



**UNIVERSITY OF NAIROBI**

**FACULTY OF SCIENCE AND TECHNOLOGY  
DEPARTMENT OF PHYSICS**

***AB INITIO* STUDY OF THE OPTICAL, STRUCTURAL,  
ELECTRONIC AND ELASTIC PROPERTIES OF  $KGeX_3$   
( $X=Br$  and  $Cl$ ) INORGANIC PEROVSKITES FOR PHOTOVOLTAIC  
APPLICATIONS**

**BY**

**NAMISI MWANAIKI MAUWA  
I56/39166/2021**

A Thesis Submitted in Partial Fulfillment of the Requirements for the Degree of  
Master of Science in Physics of the University of Nairobi.

October 2022

## DECLARATION

I declare that this thesis is my own work and has not been submitted elsewhere for examination. Where other people's work has been used, this has properly been acknowledged and referenced in compliance with the University of Nairobi's regulations.

Signature  Date...**31/10/2022**.....




NAMISI MWANAIDI MAUWA

I56/39166/2021

Department of Physics, University of

Nairobi

This thesis is submitted for research with our approval as research supervisors.

	Signature	Date
Prof. Robinson J. Musembi Department of Physics, University of Nairobi, Kenya <a href="mailto:musembirj@uonbi.ac.ke">musembirj@uonbi.ac.ke</a>		<u>01/11/2022</u>
Dr. Winfred Mueni Mulwa Department of Physics, Egerton University, Kenya <a href="mailto:winfred.mulwa@egerton.ac.ke">winfred.mulwa@egerton.ac.ke</a>		<u>01/11/2022</u>
Prof. Bernard O. Aduda ... Department of Physics, University of Nairobi, Kenya <a href="mailto:boaduda@uonbi.ac.ke">boaduda@uonbi.ac.ke</a>		01/11/2022

## ABSTRACT

Perovskite materials have proven to be good absorber materials for photovoltaic devices by virtue of their desirable optical and electrical properties, which include tunable band gap and high dielectric constant that make them interesting research materials. The perovskite materials that have shown the best photo conversion efficiency to date are those composed of hybrid inorganic-organic material and plumbum. However, the hybrid organic-inorganic perovskites exhibit intrinsic instability as the organic compounds present are sensitive to moisture, air, and oxygen. The presence of lead is also toxic to the environment. This study addressed the duo challenges by using fully inorganic elements and lead substitutes. We present a detailed first principle investigation of the structural, elastic, electronic and optical properties of  $KGeX_3$  ( $X=Cl, Br$ ) in three phases, i.e., the tetragonal, ( $P4mbm$ ) trigonal ( $R3c$ ) and cubic ( $Pm3m$ ) structures. All *ab initio* calculations in this work were performed within the Density Functional Theory (DFT) formalism as implemented in the Quantum ESPRESSO (Q.E) computational code. The self-consistent calculations were performed to solve the Kohn-Sham equations using a generalized gradient approximation (GGA) for the exchange correlation (XC) potential. The approximation of the one-body Green's function,  $G$  and the screened coulomb interaction,  $W$  (GW approximation) was used alongside the Generalized Gradient Approximation - Perdew-Burke-Ernzerhof (GGA-PBE) approximations to calculate the electronic band gaps. The optical and mechanical properties were calculated using THERMO\_PW within Quantum ESPRESSO (Q.E). The materials had reliable structural stability with the tetragonal structures having the highest bulk moduli showing incompressibility. The distorted perovskites had the lowest energies proving energetic stability. From the electronic properties, all materials had direct band gaps with the bandgap increasing from cubic-tetragonal-trigonal showing that structural distortion widens band gap values. The elastic properties showed that the trigonal structures are hard, mechanically unstable and hard hence unsuitable for photovoltaics. The theoretical efficiencies calculated from the Shockley-Queisser limit showed that the tetragonal structures had the highest power conversion efficiency (PCE) suitable for photovoltaics. Generally, we concluded that apart from the ideal cubic perovskite structure, the tetragonal structures can also be considered for photovoltaics because they were consistent in proving their excellent candidacy.

## **ACKNOWLEDGEMENTS**

First and foremost, I express my gratitude to the Almighty for his immense love and guidance throughout this journey.

I am grateful to my supervisors for holding my hand throughout this project. Prof. Robinson Musembi, for introducing me to this interesting field of computational physics, and his guidance and training throughout the research period. Thanks to Dr. Winfred Mulwa for her tireless exposures and guidance. Thank you for the great induction to Egerton University, from where I got to learn of various techniques. This work would have been impossible to complete without your help. Special thanks to Prof. Bernard Aduda for his immense support, guidance, advice and vigilance, without which this work would not have come to completion. Thank you for the constant encouragements which ensured mental and psychological wellness through my studies.

Many thanks to the research members in Egerton University; Vincent Otieno, Moses Kahura and Gabriel Chirchir for their encouragement and tireless help. I am also grateful to my colleagues in the University of Nairobi, Lynette Allan and Mwendu Mbilo for their advice, lessons and valuable assistance. To my two best friends with whom I am taking this educational journey, Sauline and Gloria, thank you and may the Lord see us through, I am glad I took this journey with you guys.

I will be forever indebted to the International Science Program (ISP) for their generosity in supporting my MSc studies to completion. This was possible through (KEN02) ([Grant 500-661-127], with Prof. Aduda Bernard as the principal investigator (PI). Immense gratitude to the Centre of High-Performance Computing (CHPC) in Cape Town, South Africa for providing the computational resources used in this work, through the project MATS1321. I appreciate the timely and efficient computational work that was carried out through your clusters.

I express my gratitude to all of you and may the Almighty reward you.



## **DEDICATION**

This work is dedicated to my amazing parents: Ramadhan Namisi Kasika and Redempta Bosibori Ondieki, my brother and small sister. Thank you for your support, prayers and belief in me.

## TABLE OF CONTENTS

DECLARATION .....	i
ABSTRACT .....	ii
ACKNOWLEDGEMENTS .....	iii
DEDICATION .....	iv
TABLE OF CONTENTS .....	v
LIST OF FIGURES .....	viii
LIST OF TABLES .....	xii
LIST OF ABBREVIATIONS .....	xiv
LIST OF SYMBOLS .....	xvi
CHAPTER ONE: INTRODUCTION .....	1
1.1: Introduction.....	1
1.2: Background of the Study.....	1
1.2.1 : DFT ab initio simulation packages.....	2
1.3: Problem Statement .....	3
1.4: Objectives .....	3
1.4.1 : General objective .....	3
1.4.2 : Specific objectives .....	4
1.5: Justification and Significance of the Study .....	4
CHAPTER TWO: LITERATURE REVIEW .....	5
2.1: Introduction.....	5
2.2: Perovskite Materials.....	5
2.2.1 : Inorganic perovskites .....	7
2.2.2 : Inorganic- organic perovskites .....	7
2.2.3 : Towards lead-free perovskite materials.....	8
2.2.4 : Replacing Pb with Ge .....	9
2.2.5: Distorted perovskite structures.....	10
2.3: Solar Cell Efficiency .....	12
2.4: The Shockley-Queisser Limit .....	13
2.5: Solar Cells Generations.....	15
CHAPTER THREE: THEORETICAL BACKGROUND .....	17
3.1: Introduction.....	17

3.2: The Schrödinger Equation (S.E) .....	17
3.3: Born-Oppenheimer Approximation .....	18
3.4: The Hohenberg- Kohn (H-K) Theorems.....	19
3.5: The Kohn- Sham Equations .....	19
3.6: The Local Density Approximation (LDA).....	21
3.7: The Generalized Gradient Approximation (GGA) .....	22
3.8: Pseudopotentials.....	22
3.9: k-point Sampling.....	23
3.10: Structural Properties.....	24
3.10.1: Tetragonal structures.....	25
3.10.2: Trigonal structures .....	25
3.10.3: Cubic structures .....	26
3.10.4: Murnaghan equation of states .....	28
3.11: Elastic Properties .....	29
3.11.1: Bulk modulus and its pressure derivative .....	33
3.12: Electronic Properties .....	33
3.13: Optical Properties.....	36
<b>CHAPTER FOUR: MATERIALS AND METHODS .....</b>	<b>39</b>
4.1: Introduction.....	39
4.2: Computational Methods.....	39
4.3: The Quantum ESPRESSO Input File.....	40
<b>CHAPTER FIVE: RESULTS AND DISCUSSIONS .....</b>	<b>42</b>
5.1: Introduction.....	42
5.2: Structural Properties.....	42
5.2.1: k-points convergence .....	42
5.2.2: Energy cutoff (ecut) convergence .....	44
5.2.3: Lattice constant convergence .....	46
5.2.4: Murnaghan equation of States.....	49
5.3: Elastic Properties .....	50
5.4: Electronic Properties .....	54
5.5: Optical Characteristics .....	59
5.6: Theoretical Efficiency.....	66

CHAPTER SIX: CONCLUSIONS AND RECOMMENDATIONS .....	67
6.1: Introduction .....	67
6.2: Conclusions .....	67
6.3: Recommendations .....	68
REFERENCES.....	70
APPENDICES .....	81
APPENDIX A: Pseudopotential files.....	81
A1: Potassium pseudopotential file- K.pbe-spn-rrjkus_psl.1.0.0.UPF .....	81
A2: Germanium pseudopotential file- Ge.pbe-n-rrjkus_psl.1.0.0.UPF .....	82
A3: Chlorine pseudopotential file- Cl.pbe-n-rrjkus_psl.1.0.0.UPF .....	82
A4: Bromine pseudopotential file- Br.pbe-n-rrjkus_psl.1.0.0.UPF .....	83
APPENDIX B: Sample input file.....	84
B1: Sample input file for cubic structure (KGeCl <sub>3</sub> ) .....	84
APPENDIX C: Murnaghan Equation of states .....	86
APPENDIX D: Publications from this Work.....	89
APPENDIX E: Relevant Conferences and Workshops Attended.....	89

## LIST OF FIGURES

- Figure 2.1 Structure of the cubic  $ABX_3$  perovskite with A and B as monovalent cations and X a halogen (Cheng *et al.*, 2018)
- Figure 2.2 Periodic table with possible  $ABX_3$  perovskites (De, 2020)
- Figure 2.3 The  $Pm3m$  cubic perovskite structure with  $BX_6$  octahedra (Howard and Stokes, 2005)
- Figure 2.4 Top and middle cross- sections of a perovskite (Burger *et al.*, 2018)
- Figure 2.5 Octahedra tilting in distorted perovskite (Howard and Stokes, 2005)
- Figure 2.6 The efficiencies of different solar panels through the years where a-Si, OPV, DSSC and PSC represents the amorphous silicon solar cell, organic photovoltaic cell, dye-sensitized solar cell and perovskite solar cells, respectively (Sundaram *et al.*, 2018)
- Figure 2.7 Graphical representation of the Shockley- Queisser limit  $E_g$  represents the band gap values in eV and AM gives the air mass coefficient (Rühle, 2016)
- Figure 2. 8 Various solar cell technologies available (Sharma *et al.*, 2015)
- Figure 3.1 the Kohn-Sham equation flowchart (Ciucivara, 2007)
- Figure 3.2 Illustration of the full and pseudo potentials with  $r_C$  as the cutoff radius of the system (Råsander, 2010)
- Figure 3.3 Schematic representations of the tetragonal  $KGeCl_3$ .perovskites using the VESTA package Momma and Izumi, (2011).

- Figure 3.4 Schematic representations of the trigonal  $\text{KGeCl}_3$  perovskites using the VESTA package Momma and Izumi, (2011).
- Figure 3.5 Schematic representations of the cubic  $\text{KGeCl}_3$  perovskites using the VESTA package Momma and Izumi, (2011).
- Figure 3.6 The octahedra tilting that can occur in perovskites and their respective space groups. C, T, O, Tr and M denotes the cubic, tetragonal, orthorhombic, trigonal and monoclinic phases, respectively Tilley, (2016) (Tilley, 2016)
- Figure 3.7 First Brillouin zones of the cubic lattice. The k-path followed is  $\Gamma - X - M - \Gamma - R - X | M - R$  (Setyawan and Curtarolo, 2010)
- Figure 3.8 First Brillouin zones of the tetragonal lattice. The k-path followed is  $\Gamma - X - M - \Gamma - Z - R - A - Z | X - R | M - A$  (Setyawan and Curtarolo, 2010)
- Figure 3.9 First Brillouin zones trigonal lattice. The k-path followed is  $\Gamma - L - B_1 B - Z - \Gamma - X | Q - F - P_1 - Z | L - P$  (Setyawan and Curtarolo, 2010)
- Figure 3.10 The spherical surface in k-space for electrons in 3D.  $k_x$ ,  $k_y$  and  $k_z$  give the coordinates in the x, y and z directions, respectively.
- Figure 4.1 A Quantum ESPRESSO input file (Hung *et al.*, 2020.)
- Figure 5.1a  $k$ -points convergence for the (i)  $\text{KGeCl}_3$  and (ii)  $\text{KGeBr}_3$  cubic perovskites
- Figure 5.1b  $k$ -points convergence for the (i)  $\text{KGeCl}_3$  and (ii)  $\text{KGeBr}_3$  tetragonal perovskites
- Figure 5.1c  $k$ -points convergence for the (i)  $\text{KGeCl}_3$  and (ii)  $\text{KGeBr}_3$  trigonal



perovskites

- Figure 5.2a Ecut convergence for the (i)  $\text{KGeCl}_3$  and (ii)  $\text{KGeBr}_3$  cubic perovskites
- Figure 5.2b Ecut convergence for the (i)  $\text{KGeCl}_3$  and (ii)  $\text{KGeBr}_3$  tetragonal perovskites
- Figure 5.2c Ecut convergence for the (i)  $\text{KGeCl}_3$  and (ii)  $\text{KGeBr}_3$  trigonal perovskites
- Figure 5.3a Lattice constant convergence for the (i)  $\text{KGeCl}_3$  and (ii)  $\text{KGeBr}_3$  cubic perovskites
- Figure 5.3b Lattice constant convergence for the (i)  $\text{KGeBr}_3$  and (ii)  $\text{KGeCl}_3$  tetragonal perovskites
- Figure 5.3c Lattice constant convergence for the (i)  $\text{KGeBr}_3$  and (ii)  $\text{KGeCl}_3$  trigonal perovskites
- Figure 5.4 Band structures and density of states of  $\text{KGeX}_3$  perovskites using DFT-(GGA-PBE) approximation. The Fermi energy level is shown by the horizontal red dashed line. VB maximum and CB minimum are shown by the red and blue circles, respectively and the discontinuities are in the regions with the blue line.
- Figure 5.5 A graph of the real part of the dielectric function against the energy in eV for the (i)  $\text{KGeBr}_3$  and (ii)  $\text{KGeCl}_3$  cubic, tetragonal and trigonal perovskite materials.
- Figure 5.6 A graph of the imaginary part of the dielectric function against the energy in eV for the (i)  $\text{KGeBr}_3$  and (ii)  $\text{KGeCl}_3$  cubic, tetragonal and trigonal perovskite materials.
- Figure 5.7 A graph of the energy loss,  $L(\omega)$ , against the energy in eV for the (i)  $\text{KGeBr}_3$  and (ii)  $\text{KGeCl}_3$  cubic, tetragonal and trigonal perovskite materials.

- Figure 5.8 A graph of the absorption coefficient,  $\alpha(\omega)$ , against the energy in eV for the (i)  $\text{KGeBr}_3$  and (ii)  $\text{KGeCl}_3$  cubic, tetragonal and trigonal perovskite materials.
- Figure 5.9 A graph of the reflectivity,  $R(\omega)$ , against the energy in eV for the (i)  $\text{KGeBr}_3$  and (ii)  $\text{KGeCl}_3$  cubic, tetragonal and trigonal  $\text{KGeX}_3$  perovskite materials.
- Figure 5.10 A graph of the refractive index,  $n(\omega)$ , against the energy in eV for the (i)  $\text{KGeBr}_3$  and (ii)  $\text{KGeCl}_3$  cubic, tetragonal and trigonal perovskite materials.
- Figure 6.1 The Murnaghan equation of states for the for the cubic, tetragonal and trigonal  $\text{KGeX}_3$  perovskite materials.

## LIST OF TABLES

- Table 5.1 The obtained values for the lattice constant convergence tests for the  $\text{KGeX}_3$  materials calculated using GGA-PBE approximation.
- Table 5.2 The calculated DFT- (GGE-PBE) lattice constants of the  $\text{KGeCl}_3$  materials in Å compared to previous work by (Hamideddine *et al.*, (2022); Houari *et al.*, (2020); Saikia *et al.*, (2020). and the respective tolerance factors.
- Table 5.3 The calculated DFT- (GGE-PBE) equilibrium volumes in Å<sup>3</sup>, minimum energies in Ry, bulk modulus in GPa and its pressure derivative from Murnaghan EoS.
- Table 5.4 The calculated elastic constants ( $C_{ij}$ ) of the  $\text{KGeX}_3$  materials in GPa using GGA-PBE approximations.
- Table 5.5 The bulk ( $B_V, B_R, B_H$ ) and shear ( $G_V, G_R, G_H$ ) moduli of the  $\text{KGeX}_3$  materials in GPa under the Voigt, Reuss and Hill averaging schemes calculated using the GGA-PBE approximations.
- Table 5.6 The Poisson's ratio ( $\nu$ ), Young's modulus  $E$  in GPa, Cauchy pressure and the  $\frac{B}{G}$  of the  $\text{KGeX}_3$  materials calculated using the GGA-PBE approximations.
- Table 5.7 The anisotropy factors, machinability and hardness of the perovskite materials calculated using the GGA-PBE approximations.
- Table 5.8 The calculated band gaps in eV of the  $\text{KGeX}_3$  materials using GGA-PBE and GW approximations compared to previous DFT reported work by (Hamideddine *et al.*, (2022); Houari *et al.*, (2020); Saikia *et al.*, (2020)

Table 5.9                      The calculated DFT- (GGE-PBE) refractive indices of the  $\text{KGeX}_3$  materials

Table 5.10                    The maximum theoretical power-conversion efficiencies of the  $\text{KGeX}_3$  materials calculated from the Shockley-Queisser limit alongside their respective band gaps.

## LIST OF ABBREVIATIONS

AM	Air mass coefficient
a-Si	Amorphous silicon solar cell
C	Cubic
CB	Conduction band
CHPC	Cluster for High Performance Computing
CIF	Crystallography Information File
CP	Car-Parrinello
DFT	Density Functional Theory
DOS	Density of states
DSSC	Dye sensitized solar cell
EoS	Equation of states
E(V)	Energy as a function of volume
FMPD	First Principle Molecular Dynamics
GGA	Generalized Gradient Approximation
GGA-PBE	Generalized Gradient Approximation - Perdew-Burke-Ernzerhof
GTF	Goldschmidt tolerance factor
GW	Approximation for one-body Green's function G and the screened Coulomb interaction W
H	Hamiltonian
H-K	Hohenberg and Kohn
HPC	High Performance Computer
K- S	Kohn-Sham
K.E	Kinetic Energy
LDA	Local Density Approximation
LED	Light emitting diode
M	Monoclinic
n	Nucleus
O	Orthorhombic
OPV	Organic photovoltaic cell
PBE	Perdew-Burke-Ernzerhof

PCE	Power Conversion Efficiency
PDOS	Partial density of states
PSC	Perovskite Solar Cell
PV	Photovoltaic
PW91	Perdew-Wang functional
PWscf	Plane Wave self-consistent field
Q.E	Quantum Espresso
S.E	Schrödinger Equation
scf	Self- consistent field
SIESTA	Spanish Initiative for Electronic Simulations with Thousands of Atoms
T	Tetragonal
T.I.S.E	Time Independent Schrödinger Equation
TDDFT	Time Dependent Density Functional Theory
Tr	Trigonal
UV	Ultraviolet
UV-Vis	Ultraviolet-visible
VASP	Vienna <i>ab initio</i> Simulation Package
VB	Valence band
vc	Variable cell
XC	Exchange correlation



## LIST OF SYMBOLS

$\alpha(\omega)$	Absorption coefficient
$A_i(i = 1,2,3)$	Shear anisotropic factors
$A_Z$	Zener's anisotropic factor
$B$	Bulk modulus
$B^I$	Pressure derivative of the bulk modulus
Bi	Bismuth
Br	Bromine
$\frac{B}{G}$	Pugh's ratio
$c$	Speed of light
$C_{IJ}$	Elastic constants
CO <sub>2</sub>	Carbon dioxide
CsGeI <sub>3</sub>	Cesium Germanium Iodide
$d$	Position
$E$	Energy of the system
$e$	Photon energy
$E_f$	Fermi energy
$E_H$	Young's modulus
$E_g$	Band gap
$E_{xc}[n(r)]$	Exchange correlation energy
$eV$	Electron volts
$\epsilon_1(0)$	Electronic part of the static dielectric function
$\epsilon_1(\omega)$	Real part of the dielectric constant
$\epsilon_2(\omega)$	Imaginary part of the dielectric constant
FA	Formamidinium
FAGeI <sub>3</sub>	Formamidinium Germanium Iodide
Fl	Flerovium
Ge	Germanium
$g(E)$	Density of states
$h$	Planck's constant

$\hat{H}$	Hamiltonian
$\hat{H}_N$	Nucleic Hamiltonian
$\hat{H}_e$	Electronic Hamiltonian
$H_V$	Vickers hardness
I	Iodine
K	Kalium (Potassium)
$k_B$	Boltzmann's constant
KGeBr <sub>3</sub>	Potassium-germanium bromide
KGeCl <sub>3</sub>	Potassium-germanium chloride
$K(\omega)$	Exciton index
$L(\omega)$	Energy loss
MA	Methylammonium
MAPbI <sub>3</sub> / CH <sub>3</sub> NH <sub>3</sub> PbI <sub>3</sub>	Methylammonium lead iodide
Mg	Magnesium
$\mu_M$	Machinability index
$N$	Number of electrons
Ni	Nickel
$N(\omega)$	Complex function of the dielectric constant
$\eta$	Maximum theoretical efficiency
$n_B$	Band index
$n(r)$	Electron density
$n(0)$	Static refractive index
$n(\omega)$	Refractive index
$P$	Pressure
$P_{max}$	Maximum power output
$P_s$	Incident power
Pb	Lead
PEA	Phenethylamine
$Q_s$	Number of absorbed photons
$R$	Coordinates of the system
$R_i$	Nuclear coordinates

$R(\omega)$	Reflectivity
$r_A$	Radius of A site atom
$r_B$	Radius of B site atom
$r_C$	Cutoff radius
$r_X$	Radius of X site atom
$r_i$	Electron coordinates
Rb	Rubidium
Ry	Rydberg
Sn	Tin
$T$	Kinetic energy
$T_e$	Kinetic energy of the electron
$T_n$	Kinetic energy of the neutron
$T_S$	Kinetic energy of non-interacting electrons
$T_{sun}$	Temperature of the sun
$t$	Goldschmidt tolerance factor
$U$	Potential energy
$U(r_i)$	Potential energy of the electron-nucleus interaction
$U(r_i, r_j)$	Electron-electron interaction
$V$	Volume
$V_{eff}$	Effective potential
$V_{BZ}$	Volume of the Brillouin zone
$V_O$	Equilibrium volume
$\nu$	Poisson's ratio
$V_H$	Hartree potential
$V_{XC}$	Exchange and correlation potential
$V_{e-e}$	Electron-electron interaction
$V_{e-n}$	Electron-neutron interaction
$V_{ext}$	External potential
$V_{n-n}$	Neutron-neutron interaction
$\lambda$	Wavelength

$\rho$	Electronic Density
$\rho_0$	Ground state density
$\Omega^1$	Volume of the unit cell in the reciprocal space
$\psi$	Wavefunction

## CHAPTER ONE: INTRODUCTION

### 1.1 : Introduction

The research background overview, goals, problem statement and the research gap addressed by this study is provided in this chapter.

### 1.2 : Background of the Study

Materials with the perovskite structure have garnered interest in the past few decades for their excellent applications as dielectrics, superconductors, and photovoltaic devices. Perovskite solar cells (PSC) are emerging as potentially life-changing devices due to their high and rapidly improving power conversion efficiency, over a very short period, more than any other solar cell type since the introduction of the first working solar cell concept by Chapin *et al.*, (1954). Perovskite-based solar cells' conversion efficiency has grown from 3.8%, since their first application in 2009, where MAPbI<sub>3</sub> served as a photosensitizer in dye sensitized solar cells (DSSC) by Kojima *et al.*, (2009), to 22.1% [ Giustino and Snaith, 2016; Yang *et al.*, 2017], to 25.2% in 2019 and to 26% recently in 2020. This is remarkable comparing to other photovoltaic cells. Silicon, for example, required 60 years to accomplish comparable PCE achievements, that is, from 4%-29%, perovskite photovoltaics taking just over a decade. As perovskite materials are mostly prepared by cheap solution methods [Giustino and Snaith, 2016], studies on the perovskite materials in PSCs could help in the potential replacement of the currently dominant silicon solar cells [Nishat *et al.*, 2021]. Currently, silicon solar cells are the most commercially used type of photovoltaic cells due to their high incident photon to electron conversion efficiency (IPCE). The main disadvantage in commercialization of these PSCs is their instability and toxicity since so far, the best perovskite materials are not environmentally friendly due to the presence of lead content, while the presence of organic compounds such as methylammonium (MA) and Formamidinium (FA) usually contributes to the instability problem due to their sensitivity to heat, moisture, and oxygen. One technique to circumvent the bottlenecks caused by instability and toxicity is to develop and optimize lead-free inorganic perovskites as this would lead to greener and more efficient devices that could be game changers in photovoltaics and other industries. This can only happen if the best perovskite material compositions are selected through studies and ensuring that the resulting materials would be suitable even after replacing lead. This study attempts to contribute to this quest by proposing an inorganic KGeX<sub>3</sub> perovskite and varying the anion of

element X between chlorine and bromine. The perovskite materials find a broad range of application such as in making optoelectronic devices, energy storage and in memory devices [Glazer, 1975]. The perovskite materials have been studied by experimental methods as well as by computational techniques. This study was done by performing first principle calculations done using the density functional theory (DFT). Enkovaara *et al.*, (2017) described DFT as a technique that has become one of the most widely used methods for simulating and predicting electronic structure properties of periodic systems. The relevance of DFT and application in research has been growing rapidly over the years.

The density functional theory (DFT) as an approximation method is used when it becomes obviously difficult to solve the many-body Schrödinger equation (S.E) while keeping in mind the degrees of freedom, and the external potentials. In DFT, we are shifting from the wave function Schrödinger equation problem, to the electron density, and this in turn reduces the already complicated 3 N-dimensional problem to one with only 3 dimensions. This is one of the reasons DFT has come to be easily accepted in research areas. Among the simulation codes used by physicists in carrying out DFT calculations are the Quantum ESPRESSO [Giannozzi *et al.*, 2020; Romero *et al.*, 2018; Scandolo *et al.*, 2005], VASP, SIESTA, and Octopus [Wan *et al.*, 2021]. This work utilizes the Quantum ESPRESSO code because it is an open-source code, not overly demanding in terms of computational resources, and friendly to users because of the already large user community.

### **1.2.1: DFT *ab initio* simulation packages**

Most of the scientific research work is conducted through experimental work, which involves laboratory, or field work, and computational means which utilize computer softwares to make simulations and predictions while making comparisons with the experimental results. Computer simulations involving DFT make use of the electron-electron interactions and the electron-nucleus interactions, which aids in the better understanding of materials in the nano scale [Kresse and Hafner, 1993]. These simulations only apply approximations to solve S.E and need no other empirical information about the system, hence the name “first principles” or “*ab initio*”. In the study of material properties, the use of computer simulations is widely employed [Romero *et al.*, 2018], and the study of electronic structure of materials centering on DFT have been made



possible. These simulation methods are flexible and can be carried out from various computing systems, depending on the properties investigated. In principle, DFT calculations are geared towards getting the exact density of the system by use of the exchange correlation (XC) potentials. These calculations aid in finding the thermo- mechanical [Malakkal *et al.*, (2016)], structural, electrical, optical and mechanical properties of materials [Roknuzzaman *et al.*, 2017]. Quantum ESPRESSO (QE) has a wide range of software used in calculating properties for example, the phonon lattice vibrations, cell dimensions, unit cell to Bravais lattice, Birch-Murnaghan equation of state, etc. QE makes use of auxiliary software like Xmgrace, Xcrysden, VESTA, GNUplot, and many more for visualization and post processing of the data obtained from calculations. The availability of numerous open-source software and being less resource demanding are part of the reasons as to why QE is utilized in this research work.

### **1.3: Problem Statement**

Perovskite materials are a game changer in photovoltaics and other applications. Despite their attractive properties, they are still not yet commercialized and marketable because of their instability and the toxicity of lead halide perovskites. Without addressing these challenges, these materials will remain to be a theoretical compound. These challenges can be counteracted by using inorganic elements and by replacement of lead by less toxic materials. The quest for potential perovskite materials has been limited to studying the structurally ideal cubic perovskite. Since perovskites are prone to phase distortions, it is crucial to give distorted perovskites equal attention in the search for dependable and sustainable photovoltaic materials. This study investigates three phases of the  $\text{KGeX}_3$  perovskite materials where X is interchanged between chlorine and bromine. The three phases are cubic, tetragonal and trigonal. In this way, this study attempts to investigate whether the overall material properties can be improved when the symmetry is lowered from the ideal cubic perovskite structure. This study also examines the effect of changing the X-site on the structural, elastic, electronic, and optical properties of  $\text{KGeX}_3$  perovskites. The use of lead-free and purely inorganic compounds would make the proposed  $\text{KGeX}_3$  (X=Cl/Br) perovskite material less toxic and more stable.

### **1.4: Objectives**

#### **1.4.1: General objective**

This study focuses on the investigation of the structural, elastic, electronic, and optical properties

of  $\text{KGeX}_3$  perovskite materials using density functional theory for photovoltaic applications.

### **1.4.2: Specific objectives**

The specific objectives of this study are to:

1. Examine the structural and elastic properties of cubic, tetragonal, and trigonal  $\text{KGeX}_3$  perovskite material.
2. Study the electronic attributes of cubic, tetragonal, and trigonal  $\text{KGeX}_3$  perovskite material.
3. Determine the optical characteristics of cubic, tetragonal, and trigonal  $\text{KGeX}_3$  perovskite material.

### **1.5: Justification and Significance of the Study**

Perovskite materials are inexpensive, solution processable, and can be synthesized in a number of ways by altering the stoichiometry or altering the occupancy of the A, B, and X sites. The power conversion efficiency of solar cells based on perovskite materials has grown at the fastest rate in photovoltaic history, with the only obstacle to commercialization being stability and toxicity. Inorganic materials are known to be more stable than their organic counterparts, and for this reason, this study seeks to provide insight for developing a multi-phase inorganic perovskite material that is stable and less toxic for photovoltaic applications. A stable inorganic perovskite with high power conversion efficiency will be a welcome alternative to the expensive silicon material that has dominated the photovoltaic industry. By examining some of the different perovskite phases, this study aims to investigate the structural, electronic, stable, and optical properties as a result of the reduction in perovskite symmetry. This will help in understanding and selection of the best perovskite phases for photovoltaic applications, which in turn will support their commercialization and the gradual shift of the environment towards clean and sufficient energy.

## CHAPTER TWO: LITERATURE REVIEW

### 2.1 : Introduction

This chapter explores the previous work on perovskite materials, perovskite solar cells (PSCs) and the silicon solar cell, the latter being the most used in the market.

### 2.2 : Perovskite Materials

Perovskite materials are named after Lev Perovski, the Russian mineralogist who proposed its structure and classification [Giustino and Snaith, 2016; Yang *et al.*, 2017]. A perovskite is any material that has  $ABX_3$  structure hence though properties of various perovskites might be different, their structures are not. The most common natural occurring type of mineral perovskite is the calcium titanate oxide ( $CaTiO_3$ ) and all perovskites take its form. The A site can be occupied by materials such as Formamidinium (FA), Methylammonium (MA), Cesium (Cs), and Rubidium (Rb), the B site with Tin (Sn), Bismuth (Bi) or Lead (Pb) and the X site with Chlorine (Cl), Bromine (Br), Nitrogen (N) or Iodine (I). Here, B is a divalent metal cation, A is a monovalent organic cation and X is a monovalent halide anion Wang *et al.*, (2019). Perovskites can either be inorganic or hybrid inorganic-organic. The structure of perovskite materials is dependent on the Goldschmidt tolerance value,  $t$ , which is given as equation (2.1);

$$t = \frac{r_A + r_X}{\sqrt{2}(r_B + r_X)} \quad (2.1)$$

Where  $r_A$ ,  $r_B$  and  $r_X$  are the radii of A, B and X atoms, respectively. Figure 2.1 shows how the  $ABX_3$  cubic structure looks like.

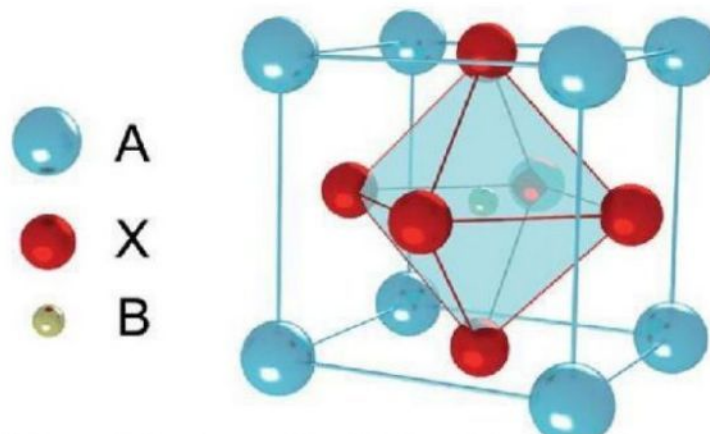


**Figure 2.1:** Structure of the cubic  $ABX_3$  perovskite with A and B as monovalent cations and X a halogen: Cheng *et al.*, (2018)

As stated earlier, different perovskite materials can be generated following the  $ABX_3$  structure. Figure 2.2 shows the periodic elements that can occupy these three sites.

**Figure 2. 2** Periodic table with possible  $ABX_3$  perovskites; De, (2020)

In terms of the properties, perovskites are yellow, brown or black minerals that have tunable bandgaps, high light absorption, broad absorption spectrum and good superconductivity Idrissi, *et al.*, (2021). Though they can occur in different structures depending on the temperature, their basic form is the cubic structure. The first ever reported perovskite material was  $MAPbI_3$  which proved to be excellent in optoelectronics (Kojima *et al.*, 2009; Tang *et al.*, 2017). In the quest to improve stability, reduce toxicity and increase the PCE of perovskite materials, several compositions have been studied and optimized such as the introduction of mixed (Cheng *et al.*, 2018; Ju *et al.*, 2017; Ma *et al.*, 2017) and double halide perovskites (Anderson *et al.*, 1993; Igbari *et al.*, 2019; Liu *et al.*, 2021; Singh *et al.*, 2021). Mixed perovskites have mixed cations in the A and B sites and the structure given as  $ABB'X_3$  for a double halide perovskite and can have up to triple cations such as the MA/FA/Cs combination. Double perovskites, in the other hand, have the  $A'A''B'B''O_6$  formula (Anderson *et al.*, 1993) or  $A_2M^{1+}M^{3+}X_6$  and have been applied in solar cells (Singh *et al.*, 2021). Perovskite materials are applied in energy storage (Zhang *et al.*, 2020), pollutant degradation (Wei *et al.*, 2021) and optoelectronic devices such as solar cells (Liu *et al.*, 2016; Roknuzzaman *et al.*,



2018; Yuan and Tang, 2020) because of their efficiency in transporting charges. Due to their stable structures and suitable band gaps, perovskite oxides are used in the production of gas sensors, spintronic devices and thermal barrier coatings (Assirey, 2019). They are also applied in catalytic activity in reactions like oxygen and hydrogen evolutions and reduction reactions (Risch, 2017). These vast applications of perovskite oxides are attributed to their low toxicity and abundance in the elements (Wu and Gao, 2018).

### **2.2.1: Inorganic perovskites**

These perovskite types consist of inorganic elements in the  $ABX_3$  structure. They are emerging as a new study area in photovoltaic applications though their counterpart, the organic-inorganic hybrid materials have been preferred because they are comparable to silicon solar cells in terms of PCE (Liu *et al.*, 2016). Inorganic perovskites are more stable in air, have suitable band gaps and simulation of these materials is easy because the structure of inorganic materials is already known. This is why these materials seem promising in obtaining stable PSCs for solar cells applications. The importance of finding the best  $ABX_3$  combination has led to researchers like Körbel *et al.*, (2016) to perform a complete sweep of the Periodic Table. In their study, high throughput calculations were used to narrow down from 32000 compounds to 20 possible materials. The study showed that Pb, Sn and Ge halide perovskites are potential prospects for photovoltaic applications because they are stable and have suitable band gaps. The improved thermal stability and conversion efficiency in solar cells was concluded just recently by Idrissi *et al.*, (2021) who investigated the electrical, structural, optical and electronic properties of the all-inorganic  $CsPbI_3$  using DFT and the Time Dependent Density Functional Theory (TDDFT) methods of calculation and employing the Quantum ESPRESSO code. On the same perovskite structure, the  $CsPbI_3$ , which is chemically stable, was found to be unstable under ambient atmosphere as recorded by Ouedraogo *et al.*, (2020) who on further investigation trying to solve this instability problem found that doping, solvent additives engineering, and 2D nanocrystal engineering are suitable ways to do so. Of all the studied inorganic perovskites, cesium-based perovskites,  $CsPbX_3$  have proven to be most stable (Faheem *et al.*, 2020).

### **2.2.2: Inorganic- organic perovskites**

These perovskite materials have both inorganic and organic compositions. The two organic compounds commonly used are the Methylammonium (MA,  $CH_3NH_3$ ) and Formamidinium (FA,

$\text{NH}_2\text{CHNH}_2$ ). Perovskite materials of this kind are versatile because they can be processed by various technologies (Saliba *et al.*, 2016). These types of perovskites are favorable because they have long charge carrier diffusion lengths, low exciton binding energies and high light absorption coefficient (Wang *et al.*, 2019). The most studied inorganic-organic perovskite is the  $\text{MAPbI}_3$  owing to its solution processability and broad absorption spectrum though its counterpart, the  $\text{FAPbI}_3$  has a broader spectrum. Hybrid perovskites are mostly studied for photovoltaic application with their PCE being greater than 23% (Park and Seok, 2019). Despite their wonderful photocatalytic properties, these perovskite types have low intrinsic stability because of the presence of organic compounds. Apart from solar cells, hybrid perovskites are also applied in X-ray detectors, thin film transistors, memory devices and Light Emitting Diodes (LEDs).

### **2.2.3: Towards lead-free perovskite materials**

The presence of lead which is soluble in water as in the Methylammonium Lead Iodide ( $\text{CH}_3\text{NH}_3\text{PbI}_3$ ) perovskite material produces  $\text{PbI}_2$  by-products which on decomposing introduce toxicity into the environment. Lead-free perovskites can be obtained by replacing Pb with any of the group 14 elements such as carbon (C), tin (Sn), germanium (Ge), silicon (Si) and Flevorium (Fl). Though getting rid of lead is crucial, it is important to ensure that its replacement does not alter the proven excellence of lead halide perovskites (Giustino and Snaith, 2016) and this tasks researchers into carefully examining and finding the best combinations whose properties can match or even exceed lead halide perovskites. Studies like that of (Filip and Giustino, 2016) who selected 25 compounds from a possible 248 found that Mg and Ni have suitably lower band gaps. According to (Liu *et al.*, 2016) bandgap and environmental toxicity reduction have been made possible by replacing Pb with Sn. In the study of Liu *et al.*, the A site was taken to be Cs, B site interchanged between Sn and Ge and the X as I, Br and Cl. The material properties were then studied and it was concluded that the stability was increased because of the resulting reduction in the crystallization rate. The overall efficiency and performance of the material solar cells also improved. In another study by (Roknuzzaman *et al.*, 2007), inorganic lead-free perovskites  $\text{CsBX}_3$  (B= Ge, Sn; X= Br, Cl, I) were simulated using first principles DFT and the resulting properties studied with comparison to lead containing materials. They concluded that the materials simulated had high optical conductivity, low reflectivity and a high absorption coefficient making them suitable for applications in optoelectronic and solar cell devices. The material  $\text{CsGeI}_3$  was found to be ideal in device applications and that Sn perovskites had lower optical absorption than Ge containing



perovskites. The study also showed that  $\text{CsSnI}_3$  was not an ideal perovskite material owing to its brittle nature. Apart from solar applications, lead-free perovskites are also applied in ceramics and can be used to replace the piezoelectric ceramics, (Takenaka *et al.*, 2007) in applications such as filters, transducer and resonator devices.

#### **2.2.4: Replacing Pb with Ge**

Other than tin (Sn), germanium has also been explored as a potential substitute for Pb since the band gaps of these materials are suitable for light harvesting. As recorded by (Krishnamoorthy *et al.*, 2015) who were the first to venture into germanium perovskite solar cells, Ge-based perovskites have excellent potential to replace Pb and in the application of the same material in device application. In their study, they synthesized germanium iodide perovskite materials,  $\text{AGeI}_3$ , (A=Cs, MA, FA) which produced both inorganic Cesium Germanium Iodide ( $\text{CsGeI}_3$ ) and organic-inorganic perovskite materials of Methylammonium lead iodide ( $\text{MAGeI}_3$ ) and Formamidinium lead iodide ( $\text{FAGeI}_3$ ). This study found that  $\text{CsGeI}_3$  showed a higher stability. For PV applications, however, these perovskites had a low PCE with 0.11% for  $\text{CsGeI}_3$  and 0.2% for  $\text{MAGeI}_3$ . To try and improve this, (Kopacic *et al.*, 2018) modified the chemical composition of these perovskites by addition of bromide ions into the hybrid  $\text{MAGeI}_3$ . This resulted in a considerable rise in the PCE of the solar cells and showed that with further studies and modifications, the germanium-based perovskites can be improved for solar cell and other applications. Other than using solely germanium, other lead-free studies such as that done by Cheng *et al.*, (2018) have incorporated germanium and tin to synthesize mixed perovskites. In this case, the organic component Phenethylamine (PEA) was used to synthesize materials with the formula  $(\text{PEA})_2\text{Ge}_{1-d}\text{Sn}_d\text{I}_4$  and was found that increasing the Sn levels decreased the bandgap. At  $d= 0.5$ , the material was found to have better stability and a bandgap of 1.95eV. All-inorganic germanium perovskites have also been studied, e.g., the study by Houari *et al.* (2019) who applied first principle calculations to find the properties of  $\text{AGeI}_3$  where the A cations were interchanged between kalium, plumbum and cesium. In that study, the germanium iodide perovskites were found to be good light harvesters in photovoltaics due to their broad absorption spectrum and high reflectance. Apart from photovoltaics, germanium halide perovskites have also been used in LEDs (Yang *et al.*, 2021) where mixed halide Pb- Ge perovskites were synthesized and showed potential of being environmentally cleaner than their counterparts, lead halide perovskites.

### 2.2.5: Distorted perovskite structures

The ideal perovskite structure is in the cubic phase with  $Pm\bar{3}m$  as the space group (Howard and Stokes, 2005; Lufaso and Woodward, 2001; Tilley, 2016). The corner-sharing octahedra of the ideal cubic structure looks like as shown in Figure 2.3.

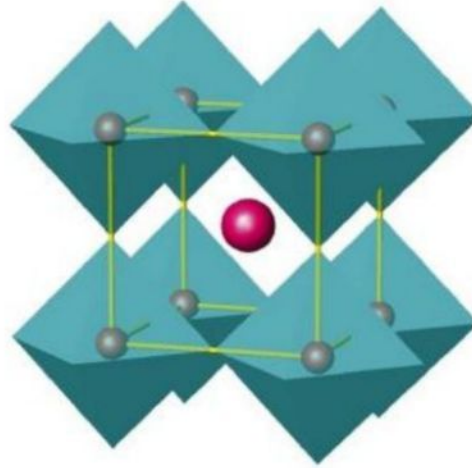


*Figure 2.3 The  $Pm\bar{3}m$  cubic perovskite structure with  $BX_6$  octahedra; Howard and Stokes, (2005)*

From Figure 2.3, the  $BX_6$  octahedra is located at the corners with the B cations sitting at the center and the A cations located in the spaces between the octahedra (Howard and Stokes, 2005; Lufaso and Woodward, 2001). The most common cause of distortion in perovskites is octahedron tilting. Here, the octahedra are tilted lowering the symmetry of the perovskite to other Bravais lattices like the trigonal, tetragonal, monoclinic and orthorhombic structures. The tilting occurs mainly if the sizes of the atoms vary. Another form of distortion is the cation displacement (Tilley, 2016). Distorted perovskites can be best described by the Goldschmidt tolerance factor in equation (2.1) which can measure if a perovskite is octahedrally tilted using the size of cation A with respect to the corner-sharing  $BX_6$  octahedra (Lufaso and Woodward, 2001). Figure 2.4 shows the top and middle cross sections of a cubic perovskite. This geometry is used to calculate the dimensions of lattice constant  $a$ . Using Figure 2.4 and considering the top cross-section, the value of lattice constant  $a$  is given by equation (2.2)

$$a = 2(r_B + r_A) \quad (2.2)$$

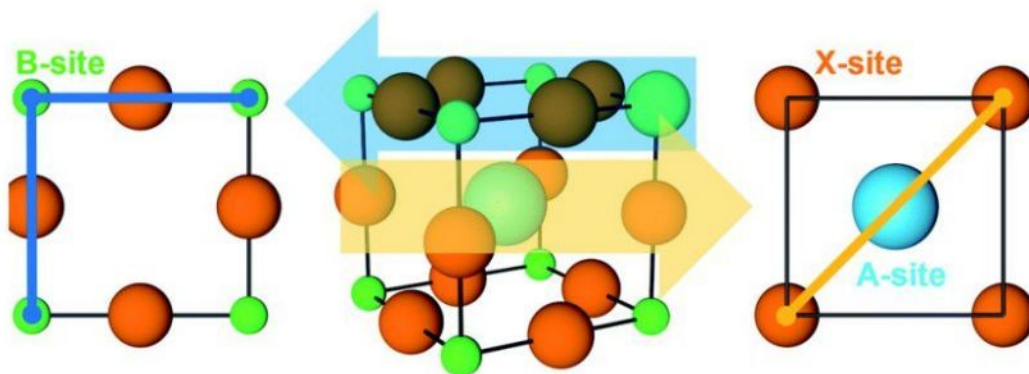


*Figure 2. 4 Top and middle cross- sections of a perovskite; Burger et al. (2018)*

Considering the middle cross- section, the value of lattice constant  $a$  is given by equation (2.3)

$$a = \sqrt{2}(r_A + r_X) \quad (2.3)$$

Then equation (2.1) gives the tolerance factor, that is, equation (2.3) divided by equation (2.2). The Goldschmidt tolerance factor (GTF) is equal to unity for the structurally ideal perovskites and the perovskite is distorted otherwise. If the cation A is too big, the Goldschmidt tolerance factor (GTF) is more than unity and the  $BX_6$  corner-sharing link is broken making the octahedra to bulge outwards. If the cation A is too small, then equation (2.1) dictates that the tolerance factor becomes less than unity. This makes the octahedra to tilt inwards since the A cations are not able to touch its neighbors. Figure 2.5 shows a distorted perovskite with a smaller A cation.

The structure changes have adverse effects on the macroscopic and microscopic material

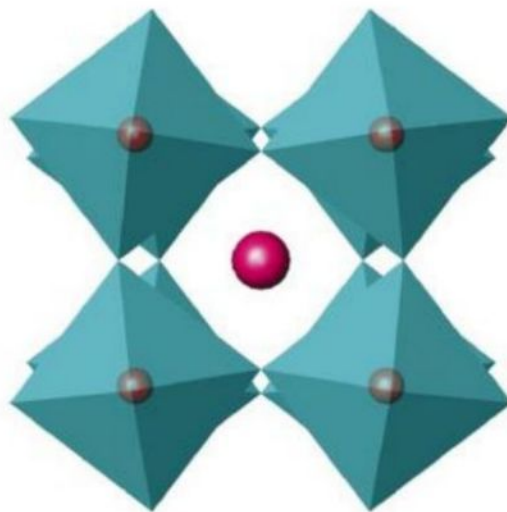


*Figure 2. 5 Octahedra tilting in distorted perovskite; Howard and Stokes, (2005)*

properties and these can also affect applications such as photovoltaics (Krishnamoorthy *et al.*, 2015) and optoelectronics (Luo *et al.*, 2021). To study these property changes caused by distortion, studies like that of (Mao *et al.*, 2018), who carried out first principle screening of all inorganic perovskites, found out that indeed, electronic properties can be altered through distortion. They studied 260 inorganic perovskites with A= Li, K, Rb, Na, Cs, B= Sn, Pb and Ge and X= I, F, Cl, Br in the cubic, orthorhombic and tetragonal phases and found that as the symmetry was being lowered to the other phases, the bandgap increased. The increase was also noted when the X element changed from I-Br-Cl-F. This, however, is not always the case as in the work by Ghaithan *et al.*, (2020) who looked into the optical, structural and electronic properties of CsPbBr<sub>3</sub> in the cubic, tetragonal and orthorhombic phases using different exchange correlation functionals and concluded that the optical properties of the materials remained unchanged. The question on which perovskite crystal structure is stable is a controversial one and is still being probed. Luo *et al.*, (2021), who studied CsGeI<sub>3</sub> existing in three distorted structures namely, trigonal *R3m*, orthorhombic *Pmmm* and the tetragonal *P4mbm* found that the most stable structure was found in the trigonal phase followed by the orthorhombic phase. For most perovskite structures, structural changes occur in a series as conditions such as pressure and temperature are changed. In most cases, the cubic structures form in cases of high temperatures and pressure (Tilley, 2016).

### **2.3 : Solar Cell Efficiency**

The percentage of energy that is transformed into electricity is referred to as the solar cell efficiency. This parameter is crucial in the desirability of solar cells. Some of the elements influencing the solar cells efficiency are the cell temperature, solar cell shading and the solar cell inclination as well as orientation. Figure 2.6 shows a comparison of efficiency of silicon solar cells, organic photovoltaics, dye sensitized solar cells (DSSC) and PSC through the years.



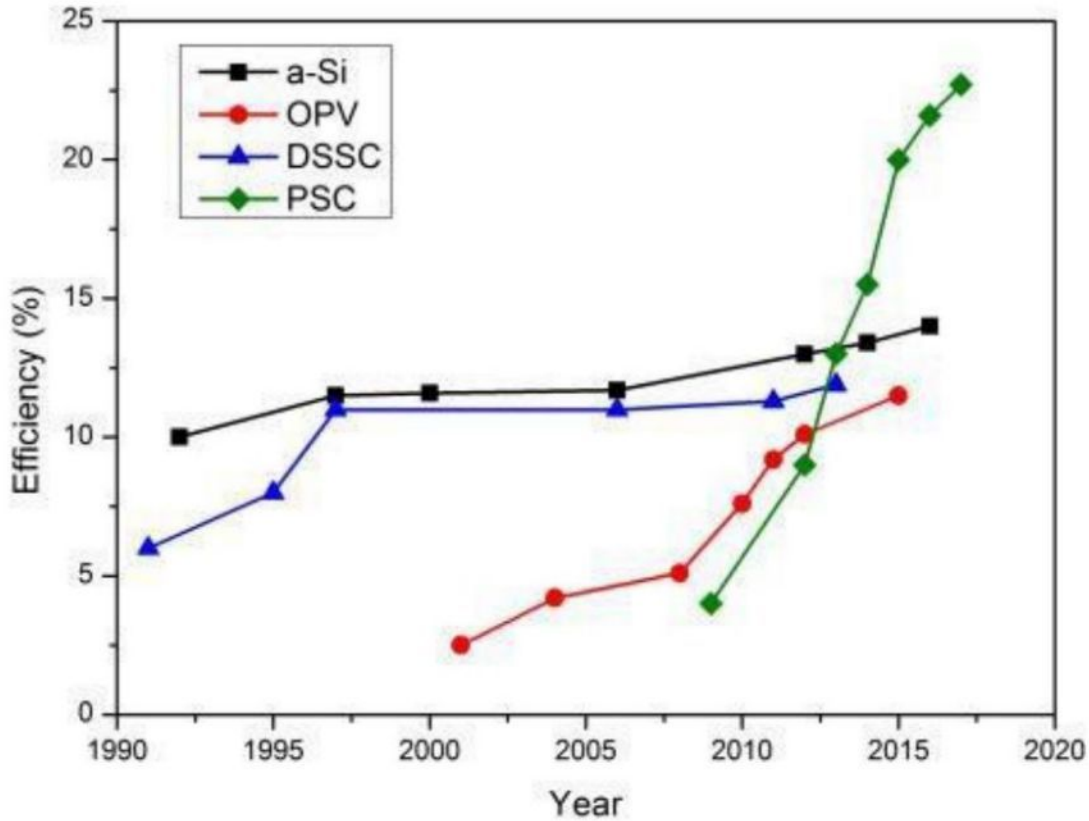


*Figure 2. 6 The efficiencies of different solar panels through the years where a-Si, OPV, DSSC and PSC represents the amorphous silicon solar cell, organic photovoltaic cell, dye-sensitized solar cell and perovskite solar cell, respectively Sundaram et al. (2018)*

In the figure 2.6, the efficiency of PSCs has remarkably increased over a short span of years and this is attributed to the research and improvement of the perovskite materials and the other layers of the solar cell.

#### **2.4: The Shockley-Queisser Limit**

Also called the detailed balance limit, the Shockley-Queisser limit is a theoretical limit in solar cells that gives the maximum theoretical efficiency a solar cell made from a single p-n junction can have (Shockley and Queisser, 1961). The maximum theoretical efficiency,  $\eta$ , is the ratio of the generated photon energy to the input power and is given by equation (2.4). (Shockley and Queisser, 1961)

$$\eta = \frac{P_{max}}{P_s} = \frac{E_g Q_s}{P_s} \quad (2.4)$$

where  $P_{max}$  is the maximum power output,  $P_s$  is the incident power,  $E_g$  is the materials' band gap and  $Q_s$  gives the number of absorbed photons (Shockley and Queisser, 1961)

From equation (2.4), the number of absorbed photons is given by equation (2.5) which is obtained from integration of the Planck's law (Marr and Wilkin, 2012);

$$Q_s = \frac{2\pi(k_B T_{sun})^3}{h^3 c^2} \int_{x_g}^{\infty} \frac{x^2 dx}{e^x - 1} \quad (2.5)$$

Where  $T_{sun}$ ,  $h$ ,  $k_B$ , and  $c$  are the sun's temperature, Planck's constant, Boltzmann's constant, and the speed of light, respectively.

$$x_g k_B T_{sun} = h\nu_g; \quad x_g = \frac{E_g}{k_B T_{sun}} \quad (2.6)$$

Finally,  $P_s$  is given by equation (2.7)

$$P_s = \frac{2\pi(k_B T_{sun})^4}{h^3 c^2} \int_0^{\infty} \frac{x^3 dx}{e^x - 1} \quad (2.7)$$

Using equation (2.8);

$$\int_0^{\infty} \frac{x^3 dx}{e^x - 1} = \frac{\pi^4}{15} \quad (2.8)$$

Equation (2.7) becomes equation (2.9), that is;

$$P_s = \frac{2\pi^5 (k_B T_{sun})^4}{15 h^3 c^2} \quad (2.9)$$

Figure 2.7 shows a graphical representation of the Shockley Queisser limit.

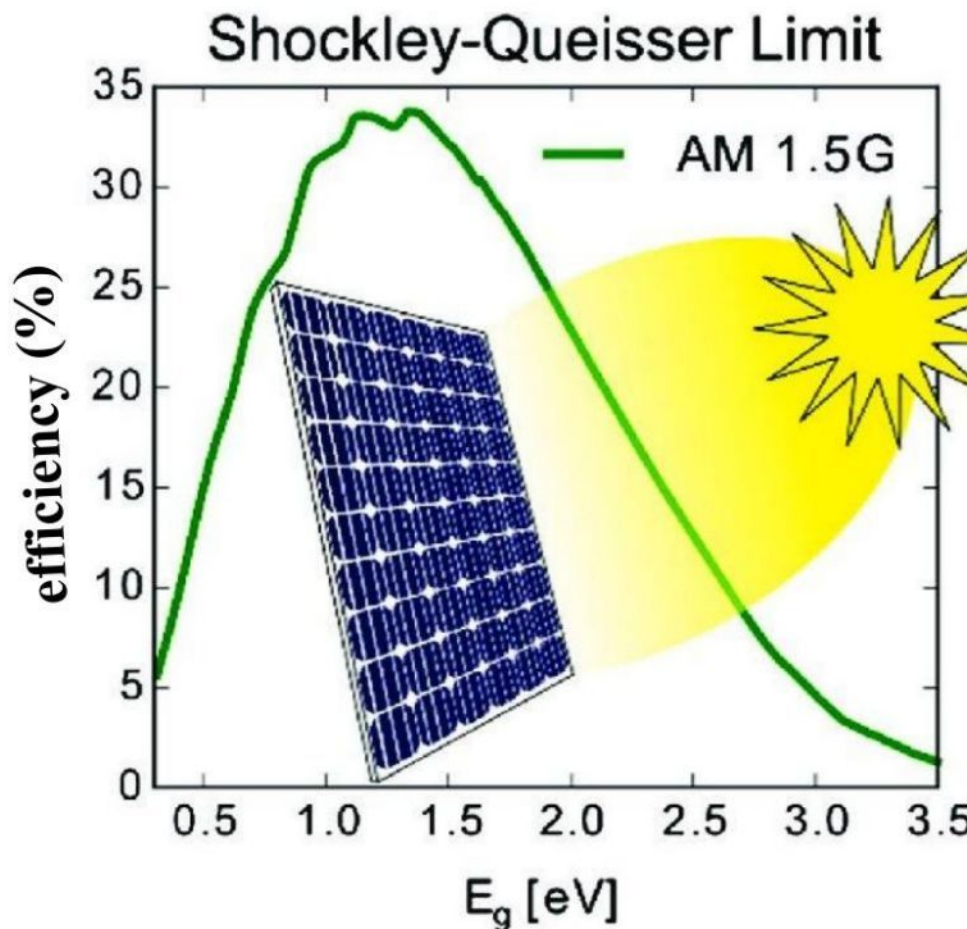
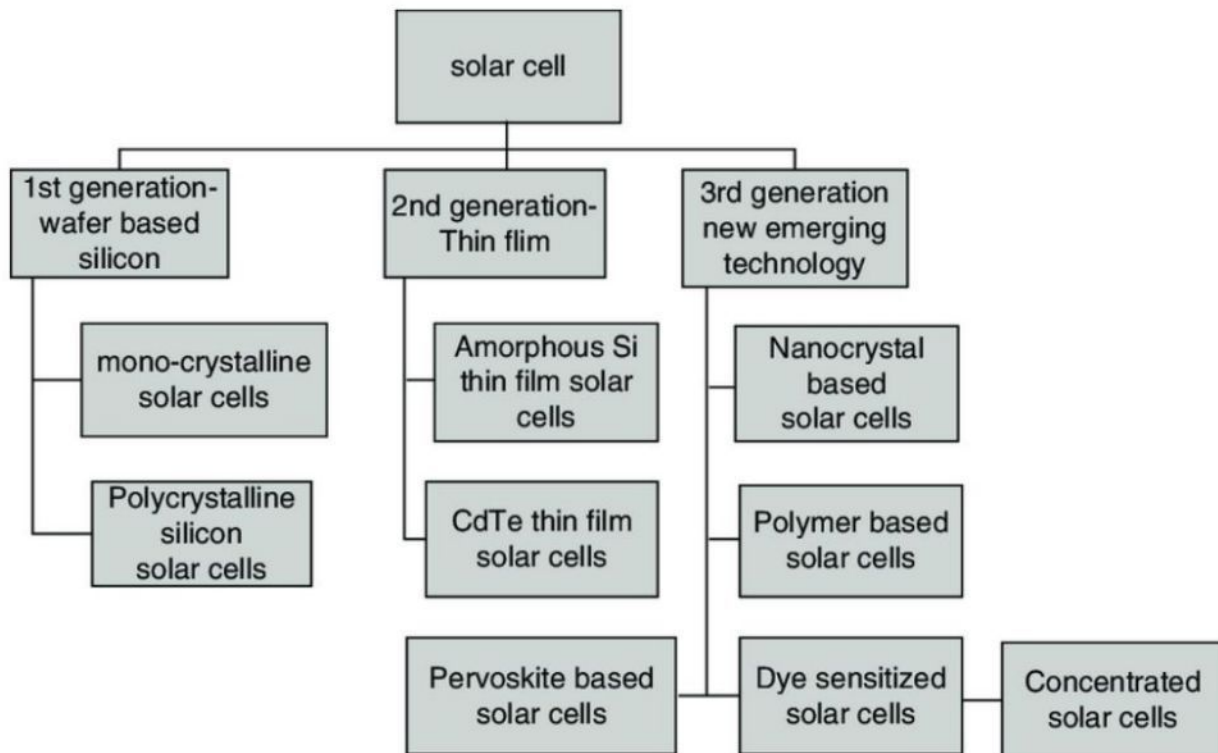


Figure 2. 7 Graphical representation of the Shockley- Queisser limit.  $E_g$  represents the band gap values in eV and AM gives the air mass coefficient. Rühle, (2016)

### 2.5 : Solar Cells Generations

Solar cells can be classified into first, second, third and fourth generation solar cells. The quest for efficient solar cell technologies has resulted to many years of research, alterations and developments (Badawy, 2015). Thus, solar cell generations are classified according to the type of material used and the periodic aspect of their developments. First generation solar cells are the oldest type of solar cells present and are mainly based on single crystals of silicon wafers (Khatibi *et al.*, 2019; Sharma *et al.*, 2015). Second generation solar cells were developed after and comprise of low-cost thin film photovoltaics including amorphous silicon and Gallium arsenide (Green, 2002; Khatibi *et al.*, 2019). Perovskite solar cells fall in the third-generation solar cells together with the dye sensitized solar cells and polymer-based solar cells (Green, 2002). Figure 2.8 gives a more detailed summary of the types of solar cells available.



**Figure 2. 8 Various solar cell technologies available (Sharma et al., 2015)**

From this chapter, perovskites have potential in revolutionizing the photovoltaic sector. Since perovskites can be synthesized in different ways using different components in the A, B and X sites, our study will study the effectiveness of potassium and germanium-based perovskites in photovoltaics by calculating their material properties. Since the B site contains germanium, which studies have shown is as equally good in photovoltaics as the toxic lead, this study's overall material will be environmentally ideal. It is also expected to be more stable and last longer since all the elements used are inorganic. Furthermore, this chapter shows that the properties of perovskites change when structural distortions happen within the perovskite materials. It is therefore crucial to compare structural, electronic, mechanical, optical and dynamical properties across the different structural phases available. This will help in choosing the best structural phases needed to produce the optimal property characteristics for different application in optoelectronics.



## CHAPTER THREE: THEORETICAL BACKGROUND

### 3.1 : Introduction

In materials physics and chemistry, understanding the structure is important and many theories have emerged to explain it. This chapter investigates the theoretical background of DFT and the theorems and approximations around it.

### 3.2 : The Schrödinger Equation (S.E)

The transition from classical mechanics to quantum mechanics is made easy by the S.E which succeeds in explaining the dynamics of quantum systems with profound precision (Sholl and Steckel, 2009).

From  $\hat{H}\psi = E\psi$ , (Schrödinger, 1926; Zerfass, 2015) the many-body S.E is given by equation (3.1):

$$\hat{H}(r_1, r_2 \dots r_N ; R_1, R_2 \dots R_M) = E\Psi(r_1, r_2 \dots r_N ; R_1, R_2 \dots R_M) \quad (3.1)$$

Where  $r_i$  and  $R_i$  represent the electron and nuclear coordinates, respectively and  $\hat{H}$  is the Hamiltonian and is the sum of all potential and kinetic energies of the system, that is, equation (3.2);

$$\hat{H} = T_e + T_n + V_{e-e} + V_{e-n} + V_{n-n} \quad (3.2)$$

Where  $T_e$  and  $T_n$  are the kinetic energy of the electron and neutron, respectively  $V_{e-e}$  is the electron-electron interaction,  $V_{e-n}$  is the electron-neutron interaction and  $V_{n-n}$  is the neutron-neutron interaction.

Since we are dealing with spatial coordinates, solving the many-body S.E becomes impossible since we have to keep into account the three dimensions of the individual electrons and it becomes more unsolvable when considering the electron-electron interactions. For example, solving the equation for CO<sub>2</sub> results in a 66-dimensional problem (Sholl and Steckel, 2009) and getting closer home with our perovskite material, solving for KGeCl<sub>3</sub> and KGeBr<sub>3</sub> would result to 306 and 468 dimensional problems, respectively which will take ages to solve. This is because K has 19 electrons, Ge has 32 electrons, Br has 35 electrons and Cl has 17 electrons. A one-dimensional problem would then have  $(19 + 32 + (X \times 3))$  electrons with the three-dimensional problem having 306 and 468 electrons for the KGeCl<sub>3</sub> and KGeBr<sub>3</sub> perovskite, respectively. The Born-Oppenheimer approximation attempts to simplify the S.E.

### 3.3: Born-Oppenheimer Approximation

This is an approximation for the motion of molecules. Since electrons are light and small in size, they have a more rapid response to atomic changes. The nucleus, on the other hand, is heavy and much bigger in size hence slow and for this reason; they can be treated as fixed points (Zerfass, 2015). The Born- Oppenheimer approximation separates the nucleus and electrons into two distinct ground state quantum mechanical problems. Using this, the molecular Hamiltonian is given by equation (3.3):

$$\hat{H} = \hat{H}_N + \hat{H}_e \quad (3.3)$$

where  $\hat{H}$  is the total Hamiltonian,  $\hat{H}_e$  is the electronic Hamiltonian and  $\hat{H}_N$  is the nucleic Hamiltonian. The electronic Hamiltonian constitutes of the electronic kinetic and potential energies and is as in equation (3.4), (Toulouse, 2019),

$$\hat{H} = T_e + V_{e-e} + V_{e-n} \quad (3.4)$$

From equation (3.4),  $T_e$  is the kinetic energy of the electron,  $V_{e-e}$  is the electron-electron interaction and  $V_{e-n}$  is the electron-nucleus interaction. This approximation is used to simplify the S.E in the many-body case by only focusing on the electrons. By only dealing with the electrons, the Time Independent Schrödinger Equation (T.I.S.E) in equation (3.1) becomes equation (3.5) (Harrison, 2005):

$$\hat{H}(r_1, r_2 \dots r_N) = E\Psi(r_1, r_2 \dots r_N) \quad (3.5)$$

where from this, the wavefunction  $\Psi$ , is given by equation (3.6);

$$\Psi = (r_1, r_2 \dots r_N) \quad (3.6)$$

From the S.E in equation (3.5), replacing the electronic Hamiltonian gives equation (3.7)

$$(T_e + V_{e-e} + V_{e-n})(r_1, r_2 \dots r_N) = E(r_1, r_2 \dots r_N) \quad (3.7)$$

and from Sholl and Steckel, (2009), this can be expanded as in equation (3.8)

$$\left[ \frac{h^2}{2m} \sum_{i=1}^N \nabla_i^2 + \sum_{i=1}^N U(r_i) + \sum_{i=1}^N \sum_{j<1}^N U(r_i, r_j) \right] \Psi = E\Psi \quad (3.8)$$

In this case,  $h$  represents the Planck's constant,  $N$  gives the total number of electrons,  $m$  is the mass of the electron,  $U(r_i)$  is the potential energy of the electron-nucleus interaction and  $U(r_i, r_j)$

represents the electron-electron interaction. From the above equation (3.8), the electron- electron interaction still poses a problem in the solving of the equation and DFT ‘takes care’ of that.

### 3.4: The Hohenberg- Kohn (H-K) Theorems

The Hohenberg and Kohn theorems jump-started the transition into DFT by showing that the density function contains all the information we need about a system (Epstein and Rosenthal, 1976; Gaa *et al.*, 1964.) and proves to be less complicated since the density has only three coordinates hence easier to solve the many- body problems. In this case, the example given above of CO<sub>2</sub> and the perovskite atoms all reduce to a 3-dimensional problem. In DFT, the Hamiltonian involves the interaction of electrons with one another and external potential, which is in many cases the nucleus-electron interaction. Since there exists a one-to-one mapping from the potential to the ground state density as shown in equation (3.9), that is (Sholl and Steckel, 2009.; Toulouse, 2019),

$$U(r) \rightarrow n(r) \quad (3.9)$$

Hohenberg and Kohn showed that the inverse is true as in equation (3.10); that there is a mapping from the ground state density to the potential (Toulouse, 2019)

$$n(r) \rightarrow U(r) + Const \quad (3.10)$$

From this, the ground state density determines the potential (Harrison, 2005.) from which the Hamiltonian of the system is obtained thus everything about the system. The first Hohenberg-Kohn theorem, proven by the contradiction method, showed that the ground state energy is a unique functional of the electron density, hence the name DFT. The main limitation of this theorem is that it only proves that there exists an energy functional but does not specify further on what exactly the functional is (Sholl and Steckel, 2009). The second Hohenberg-Kohn theorem probes whether a given density is the lowest density possible, i.e., the ground state density  $\rho_0$ . This optimization is done following the variational principle where trial densities are used to find the minimum energies.

### 3.5: The Kohn- Sham Equations

Applying the S.E from the H-K theorems, the energy functional can be expressed by equation (3.11) (Harrison, 2005);

$$E[\rho] = T[\rho] + V_{ext}[\rho] + V_{e-e}[\rho] \quad (3.11)$$

Where  $V_{ext}$  is the external potential. From equation (3.11), the K.E and e-e interaction functionals can only be approximated since their exact values are unknown. Since the K.E makes up almost all the total energy of the system, proper approximation of its functional is crucial. This is where the K-S equations come in and they make it possible to calculate nearly all the K.E by the introduction of a system of non-interacting electrons that have the same  $\rho_0$  as the usual system with interacting electrons. These equations (Kohn and Sham, 1965) also solve the variational principle problem of looking for trial densities that will give the ground state energies. Since the  $\rho_0$  are the same, the two systems are said to have the same position and atomic numbers. We can then shift to the non-interacting system since the Hamiltonian will be calculated from the electron independence. Equation (3.11) then becomes equation (3.12);

$$E[\rho] = T_s[\rho] + V_{ext}[\rho] + V_H[\rho] + E_{XC}[\rho] \quad (3.12)$$

From the energy functional, the K-S equations are expressed by equation (3.13) (Sholl and Steckel, 2009.);

$$\left[ \frac{\hbar^2}{2m} \nabla^2 + U(r) + V_H(r) + V_{XC}(r) \right] \Psi_i(r) = E_i \Psi_i(r) \quad (3.13)$$

From the K-S equation above, notice that it differs from the S.E because we are dealing with individual electrons.  $V_H$  is the Hartree potential and  $V_{XC}$  represents the exchange and correlation potential. Solving the K-S equations proves to be a loop because the electron density,  $n(r)$ , needs to be known to solve the equation and at the same time the solution of the K-S equation is needed for the electron density to be found (Sholl and Steckel, 2009). To be able to solve it therefore, an iterative method is used by first solving using a trial density first after which the wavefunction can be obtained. From this, the density is then calculated and compared with the trial density and if they converge, then this is the ground state electron density from which the energy can be calculated. If not, then the process is repeated. This can be summarized from the flow chart in Figure 3.1. Errors arise from the fact that the K.E above is not for a real system and that an electron cannot interact with itself and this error is taken care of by the additional exchange correlation functional  $[\rho]$ . This  $[\rho]$  can then be approximated using various methods which will in turn give the Hamiltonian and the density functional. The commonly used approximation methods include

the Local Density Approximation (LDA) and the Generalized Gradient Approximation (GGA).

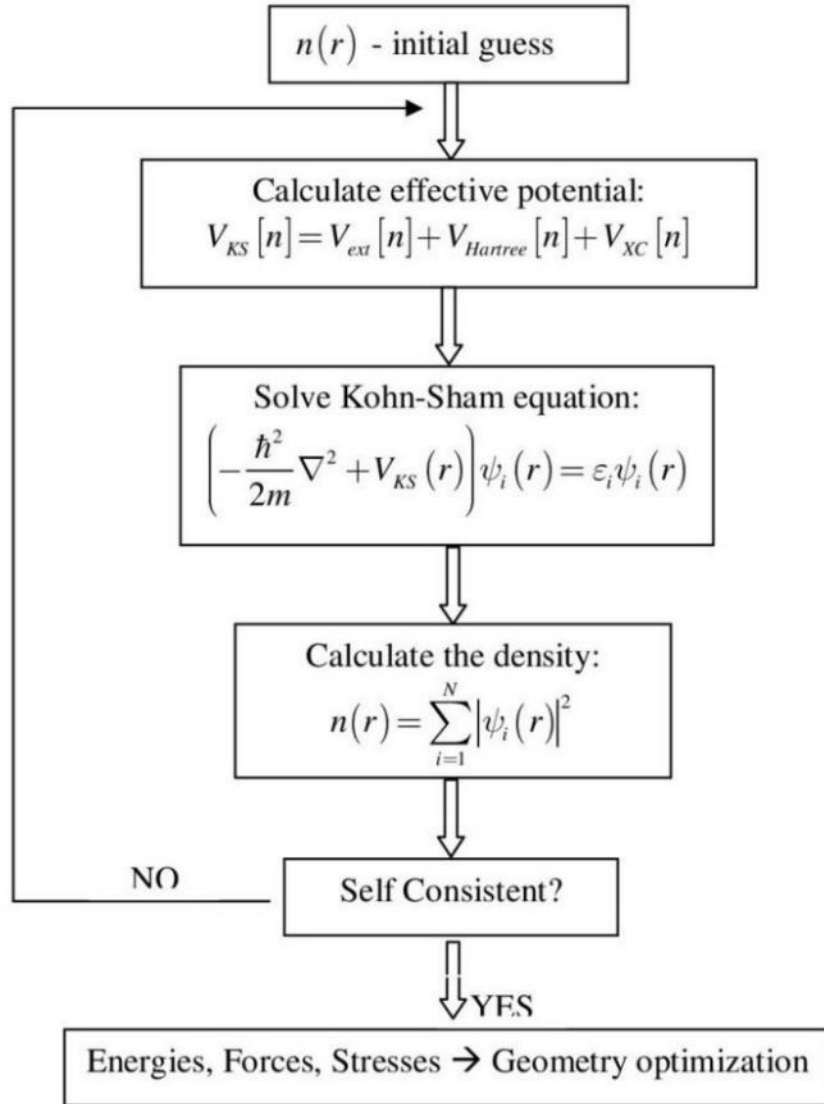


Figure 3. 1 The Kohn-Sham equation flowchart (Ciucivara, 2007)

### 3.6: The Local Density Approximation (LDA)

The LDA was proposed by Hohenberg and Kohn and is the oldest exchange-correlation functional. It makes use of the case of uniform electron gas where  $n(r)$  is taken to be constant everywhere. From the name, the LDA approximates the exchange-correlation functional using the local density only. In many systems, the LDA provides a good exchange-correlation approximation. This is because it underestimates the correlation functional but overestimates the exchange functional,

making the overall exchange-correlational functional very concise (Capelle, 2006). LDA only works in situations where the  $n(r)$  is constant hence limiting (Malakkal *et al.*, 2016; Sholl and Steckel, 2009). This is because real systems are inhomogeneous (Capelle, 2006). In LDA, the exchange-correlation energy  $E_{XC}[n(r)]$  of the system is locally approximated and is given by equation (3.14) (Zerfass, 2015),

$$E_{XC}^{LDA}[n(r)] = \int E_{XC}(n(r))n(r)dr \quad (3.14)$$

### 3.7: The Generalized Gradient Approximation (GGA)

The Generalized Gradient Approximation (GGA) was developed after LDA mainly because LDA fails in real systems (Sholl and Steckel, 2009). The GGA tends to give a more accurate approximation and is the mostly used, though it is computationally more expensive than LDA. Its accuracy stems from the fact that it contains additional physical information about the system than LDA (Sholl and Steckel, 2009). It considers the local electron density and the local gradient in the electron density hence giving better results than LDA. It should be noted, however, that GGA does not accurately predict the lattice parameters and the hydrogen bond is also not treated accurately. GGA consists of many unique functionals. Some of GGA functionals include the Perdew-Burke-Ernzerhof-Generalized Gradient Approximation (GGA-PBE), the Perdew-Burke-Ernzerhof for solids (PBEsol) and the Perdew-Wang-91 (PW91). This study used the GGA-PBE functionals for the exchange-correlation approximation.

### 3.8: Pseudopotentials

In solids, the electrons are divided into the inner core electrons and the valence electrons. The core electrons are inert and do not participate in chemical bonding hence only the valence electrons take part in chemical bonding, and ultimately determine the physical properties of materials (Råsander, 2010; Sholl and Steckel, 2009). For this reason, the core electrons can be fixed and focus is put only on the valence electrons after which the effective potential ( $V_{eff}$ ) is found. This was done by replacing the core electrons by a weaker pseudopotential which mimicked the effect of the core electrons. Doing this reduced the computational burden caused by the electrons Sholl and Steckel, (2009). Pseudopotentials were obtained from the Q.E website where they were downloaded and the right pseudopotential file chosen according to the chosen approximation functional (GGA-PBE). Alternatively, they can also be obtained from the GBRV pseudopotentials site. This site is named after the creators using the initials, that is, Kevin F. Garrity, Joseph W.



Bennett, Karin M. Rabe, and David Vanderbilt. Figure 3.2 shows the pseudo electrons and the all-electron potentials and their wavefunctions. The dashed lines show the pseudo potential and wavefunctions which are smoothed and correspond to the true potential and wavefunction, respectively.

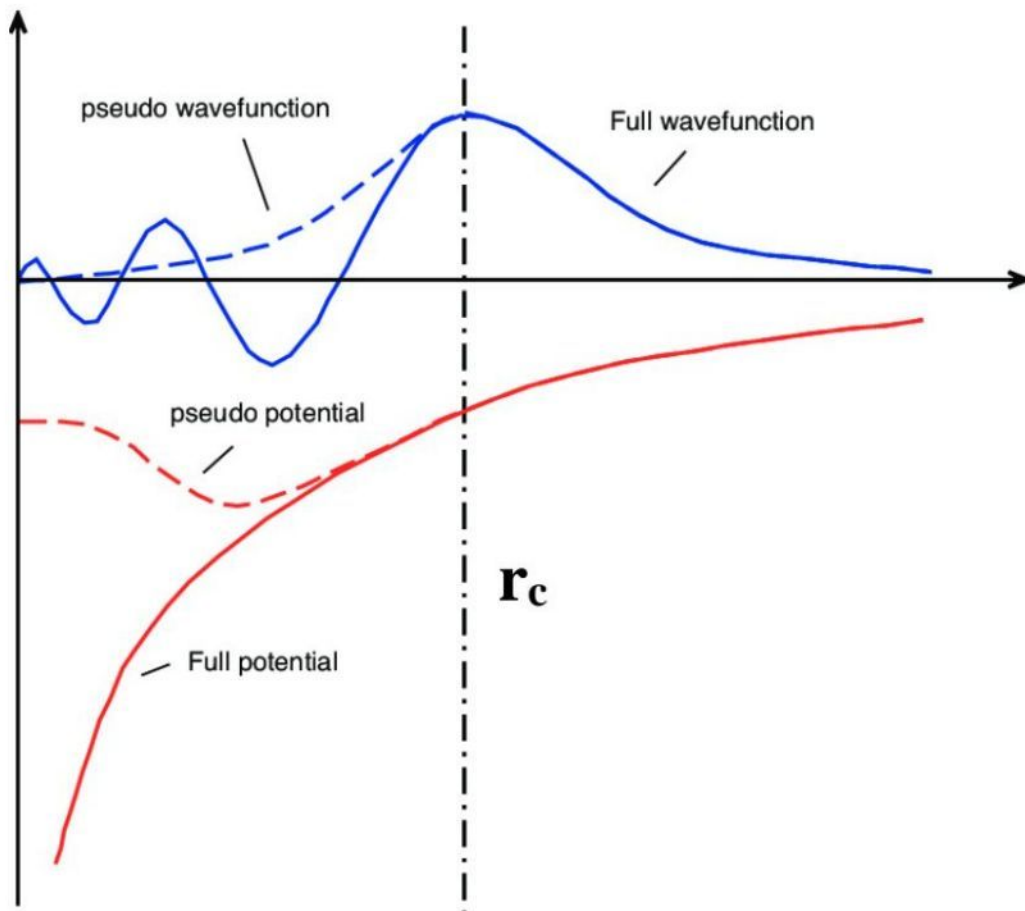


*Figure 3. 1 Illustration of the full and pseudo potentials with  $r_c$  as the cutoff radius of the system (Råsander, 2010).*

### 3.9: k-point Sampling

$k$ -points exist in reciprocal space. In crystal structure calculations, it is crucial to integrate periodic functions over the Brillouin zone. To ensure efficiency, sampling of the  $k$ -points in the reciprocal space was done to only pick and use special points of high symmetry. The commonly used method for  $k$ -point sampling is the Monkhorst-Pack method (Monkhorst and Pack, 1976) which uses equally spaced mesh in the Brillouin zone. Here, the sequence used is (nd1 nd2 nd3 d1 d2 d3)

where the last three terms specify the displacement from the origin and is set to 0 for situations where there is no offset. The first three give the  $k$ - points and differs from the dimensions used. In 3D for example, the  $k$ - points will be (  $n\ n\ n\ 1\ 1\ 1$  ) and (  $n\ n\ 1\ 1\ 1\ 1$  ) in the 2D case and so on.  $k$ - points were optimized to acquire the desired size of the Brillouin-zone for the band structure calculations. In this work, the  $k$ -points used in the band structure calculations were obtained from the Materials Cloud website (Hinuma *et al.*, 2017; Togo and Tanaka, 2018.). The  $k$ -path chosen was unique to the crystal structure obtained (Setyawan and Curtarolo, 2010). The density of states and the projected density of states (DOS and PDOS) were obtained from the electronic structure calculations and the  $k$ - points need to be dense as well (Sholl and Steckel, 2009). From the DOS, the material can be categorized as an insulator, semiconductor or metal and the band structure plot shows if the bandgap is direct or indirect and tell the type of semiconductor a material is.

### 3.10: Structural Properties

The structural properties investigated were the lattice constant  $a$ , the bond lengths and angles and the bulk modulus and its first derivative. The materials studied were in three phases, that is, the cubic, tetragonal and trigonal. The cubic phase has  $a = b = c = 5.89\text{\AA}$  and  $\alpha = \beta = \gamma = 90^\circ$ . The tetragonal phase has  $a = b = 7.97\text{\AA} \neq c = 5.81\text{\AA}$  and  $\alpha = \beta = \gamma = 90^\circ$ . The trigonal phase has  $a = b = c = 7.67\text{\AA}$  and  $\alpha = \beta = \gamma < 120^\circ, \neq 90^\circ = 60.04^\circ$ . For the lattice constant, optimization was done first to ensure the kinetic energy cut off (ecut) and k-point values were converging. Convergence ensures accuracy of calculated results compared to reported experimental findings (Sholl and Steckel, 2009). The k-point convergence was done first after which the converged value was used for the ecut convergence. The k-point sampling was done using the Monkhorst- Pack grid. The  $k$ -points convergence was done in the range of  $2 \times 2 \times 2$  to  $24 \times 24 \times 24$  at intervals of  $2 \times 2 \times 2$  with the convergence criterion at  $10^{-4}$  Ry. The ecut convergence was then carried out in the range from 10-125 Ry at intervals of 5Ry with the convergence criterion also at  $10^{-4}$  Ry. The ecut convergence was expected to obey the variational method with the total energy monotonically decreasing with increase in the cutoff energy. Finally, lattice constant convergence was carried out in which both the converged ecut and k-point were used. For trigonal structures, the lattice constant convergence was done in the range of 12-17.4 Bohr at intervals of 0.2 Bohr. For cubic structures, the lattice constant convergence was done in the range of 8.9-12.0 Bohr at intervals of 0.1 Bohr. Lastly, for the tetragonal structure, lattice constant convergence was done at 12.9-16.0 Bohr at intervals of 0.1 Bohr. After convergence, structural optimization was



done using *vc-relax* to fix the atoms in their positions and to get the optimized lattice constant.

### 3.10.1: Tetragonal structures

Information about the different structural symmetries was obtained from the Automatic FLOW for materials discovery (AFLOW) (Hicks *et al.*, 2019, 2021; Mehl *et al.*, 2017). Tetragonal structures have two types of Bravais lattices, that is, the body-centered tetragonal and the simple tetragonal. The simple tetragonal has 49 space groups including the *P4mbm*. The tetragonal perovskite studied belongs to the *P4mbm* space group. The unit cell is made up of 10 atoms, that is, 2 K atoms, 2 Ge atoms and 6 Br/Cl atoms. Ge atoms are located at the corner and the base centered positions with fractional coordinates of (0, 0, 0) and (0.5, 0.5, 0). The Cl and Br atoms occupy the face-centered positions around the germanium atoms. Figure 3.3 shows the tetragonal structure of the perovskite studied in this work. According to Tilley, (2016), the tetragonal structures with space groups *P4mbm* undergo one tilt in their corner-sharing octahedra. This tilt is symbolized by  $a^0a^0c^+$  which indicates that the tilting occurs around the z-axis.

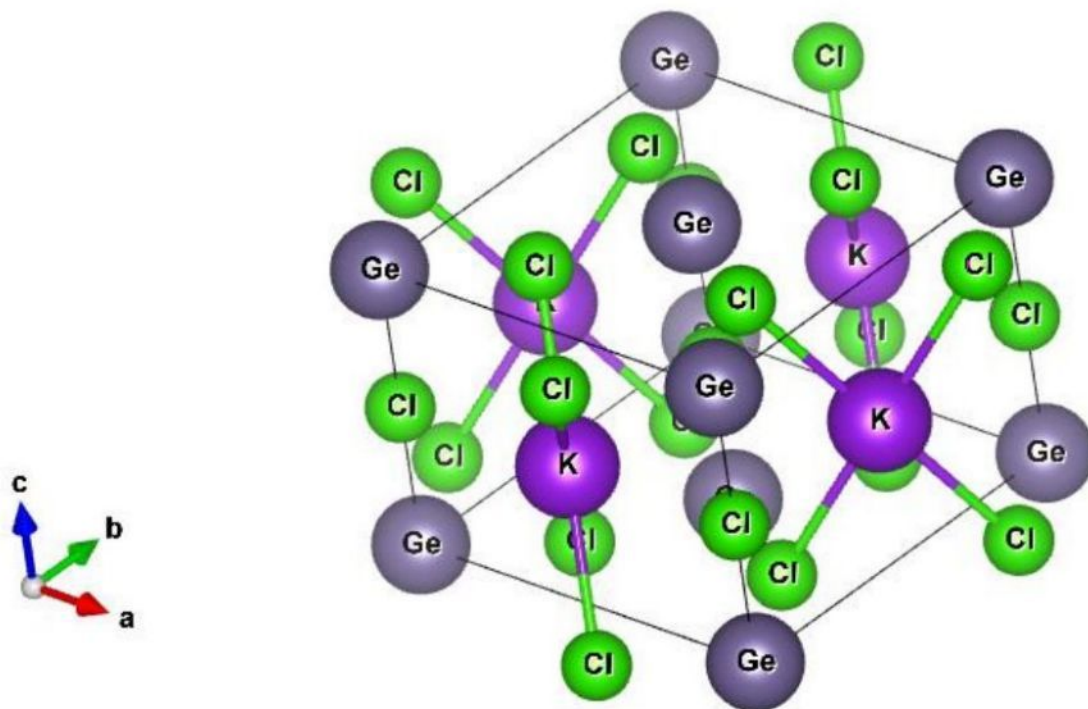
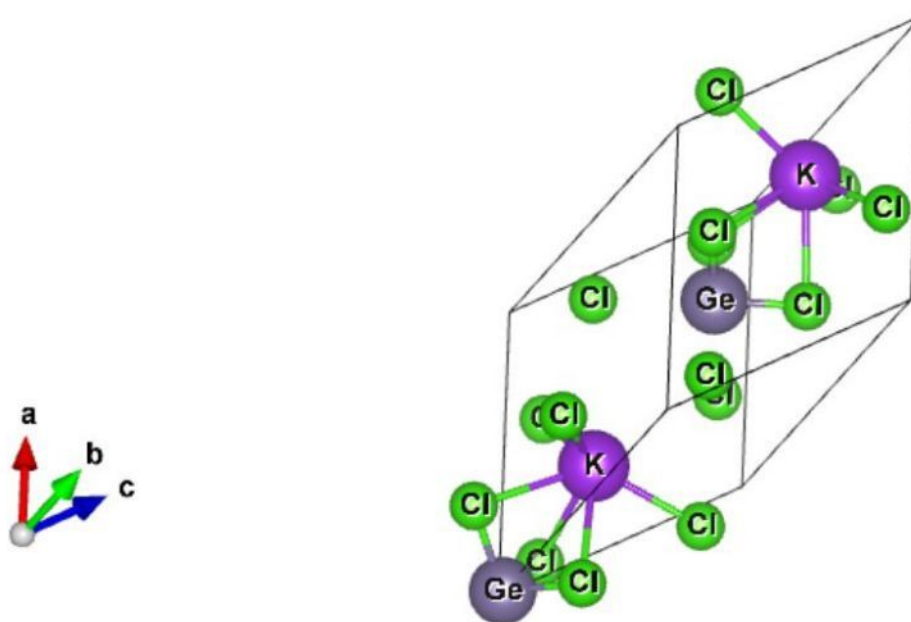


Figure 3.3: Schematic representations of the tetragonal  $KGeCl_3$  perovskites using the VESTA package Momma and Izumi, (2011).

Trigonal symmetries are formed when cubic structures are pulled along the diagonals (Hicks *et al.*, 2019). These structures have two types of Bravais lattices, that is, the hexagonal and the

rhombohedral lattice (Hicks *et al.*, 2021). The trigonal perovskite studied belongs to the  $R3c$  space group which is part of the rhombohedral lattice. The unit cell is made up of 10 atoms, that is, 2 K atoms, 2 Ge atoms and 6 Br/Cl atoms. Figure 3.4 shows the trigonal perovskite structure that was studied. The octahedra tilting in trigonal  $R3c$  is symbolized by  $a^-a^-a^-$ . This means that the structure undergoes three equal tilts which occur in the opposite directions. (Tilley, 2016)



*Figure 3.4: Schematic representations of the trigonal  $KGeCl_3$  perovskites using the VESTA package Momma and Izumi, (2011).*

### 3.10.3: Cubic structures

The ideal cubic perovskite is in space group  $Pm3m$  and is illustrated in figure 3.5. Since the structure is ideal, the tilt is symbolized by  $a^0a^0a^0$ . This shows that there are zero tilts. The unit cell is made up of 5 atoms, that is, 1 K atom, 1 Ge atom and 3 Br/Cl atoms. The K atoms are located at the corner positions with fractional co-ordinates of (0, 0, 0). Ge is located at the body-centered positions at (0.5, 0.5, 0.5) and the X atoms (Cl and Br) occupy the face centered positions at (0.5, 0.5, 0), (0, 0.5, 0) and (0.5, 0, 0.5). Figure 4.5 shows the visualized cubic structure of the perovskite studied. Since potassium-based perovskites have not been explored experimentally, this study

could not point out the temperature and pressure ranges in which the structural phase transitions happen.

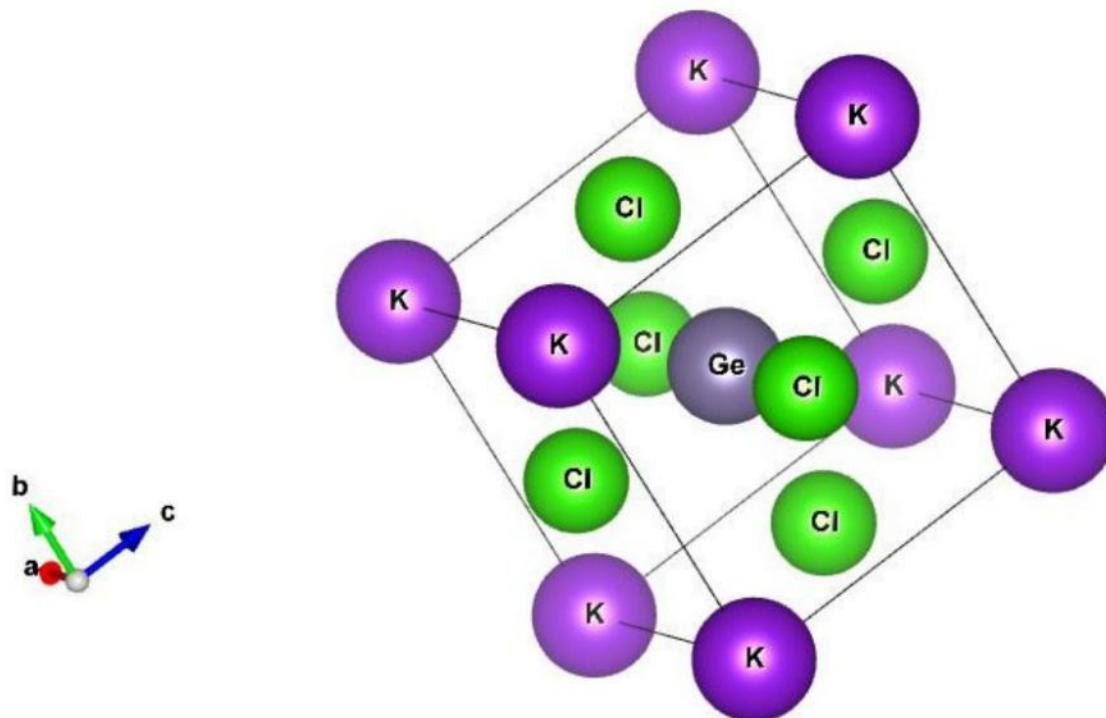


*Figure 3.5: Schematic representations of the cubic  $KGeCl_3$  perovskites using the VESTA package* Momma and Izumi, (2011).

From schematic representation of the ideal cubic structure in figure 3.5, figure 3.6 shows all the possible tilt systems in perovskites and the respective space groups. From this figure (4.6), C, T, O, Tr, M represents the cubic, tetragonal, orthorhombic, trigonal and monoclinic phases, respectively.



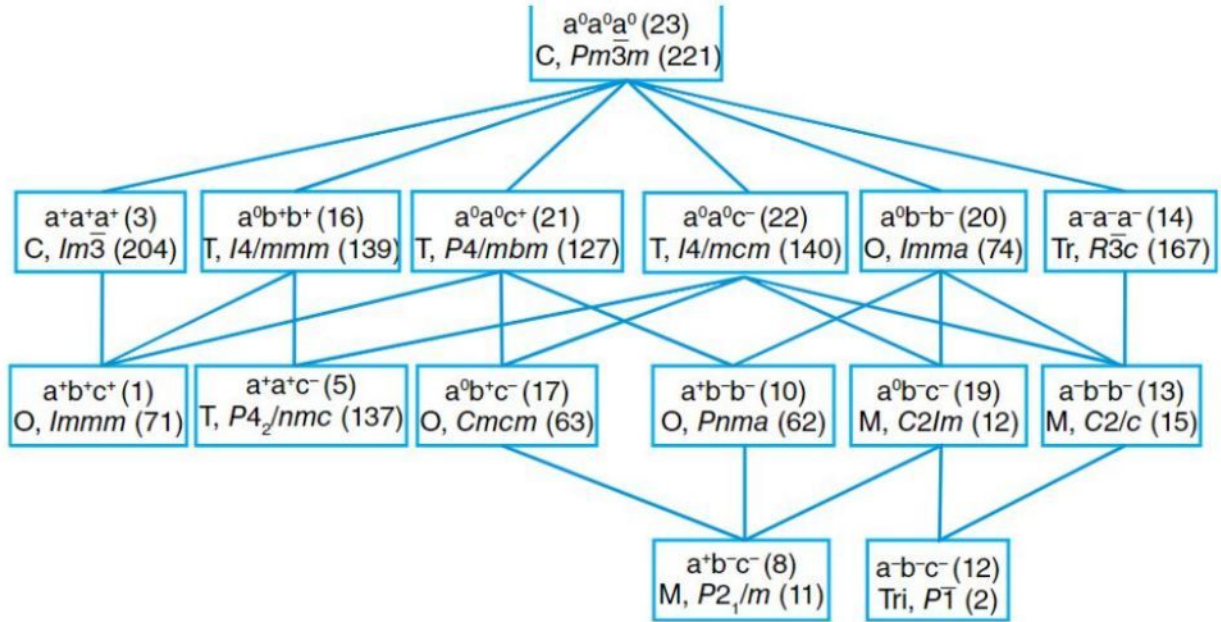


**Figure 3. 6** The octahedra tilting that can occur in perovskites and their respective space groups. *C, T, O, Tr* and *M* denotes the cubic, tetragonal, orthorhombic, trigonal and monoclinic phases, respectively. Tilley, (2016)

### 3.10.4: Murnaghan equation of states

The Murnaghan Equation of States (EoS) was used to obtain the equilibrium volume, the bulk modulus and its derivative. This was done by fitting the values of the energy versus volume data to this equation of state (Allan *et al.*, 2022). From thermodynamics definition, an EoS relates the volume, temperature and pressure of a material in a thermodynamic equilibrium (Mansour, 2020; Tyuterev and Vast, 2006). The pressure-volume relationship of a material with fixed number of particles is given by equation (3.15) (Tyuterev and Vast, 2006).

$$P(V) = \frac{B_0}{B_0^1} \left[ \left( \frac{V_0}{V} \right)^{B_0^1} - 1 \right] \quad (3.15)$$

To find the energy with respect to the volume, equation (3.15) is integrated leading to equation (3.16).

$$E(V) = \frac{B_0 V}{B_0^1} \left[ \left( \frac{V_0}{V} \right)^{B_0^1} \frac{1}{B_0^1 - 1} + 1 \right] + \text{Constant} \quad (3.16)$$

In Q.E, the energy-volume (ev.x) command was used to fit the energy and volume values into the Murnaghan equation. This fitting was done after the lattice constant convergence was carried out from which the energies of different volumes were obtained.

### 3.11: Elastic Properties

The elastic properties are crucial in determining the mechanical stability of materials. The properties studied in this work are the elastic constants, the bulk, Young's and shear moduli and the Poisson's ratio. The elastic properties were calculated using the *thermo\_pw* within Q.E. The elastic constants are denoted by  $C_{ij}$  and vary from one crystal system to the other. The elastic constants obtained from the second derivative of the crystal energy with respect to the strain are given by equation (3.17) as shown by Mouhat and Coudert, (2014); Thakur, (1982).

$$C_{ij} = \frac{1}{V_0} \left( \frac{\partial^2 E}{\partial \varepsilon_i \partial \varepsilon_j} \right) \quad (3.17)$$

Where  $V_0$  is the equilibrium volume,  $E$  is the energy of the crystal and  $\varepsilon$  is the strain. The elastic constants  $C_{ij}$  make up the elastic matrix which then describe the elastic behaviors of materials (Mouhat and Coudert, 2014). The elastic constant matrix is a 6x6 matrix. In order for a material to be stable, the principal minor determinant of the elastic constant matrix should be positive. From this condition, a set of inequalities can then be obtained for which the elastic constants  $C_{ij}$  must satisfy. From the Born stability criteria (Born, 1940; Mouhat and Coudert, 2014), these elastic constants need to meet certain conditions for the materials to be considered mechanically stable. As shown by Mouhat and Coudert, (2014) the elastic constants matrix for cubic phases is the simplest and is given by equation (3.18)

$$\begin{pmatrix} C_{11} & C_{12} & C_{12} & & & \\ C_{12} & C_{11} & C_{12} & & & \\ C_{12} & C_{12} & C_{11} & & & \\ & & & C_{44} & & \\ & & & & C_{44} & \\ & & & & & C_{44} \end{pmatrix} \quad (3.18)$$

The cubic phases have three independent elastic constants, that is,  $C_{11}$ ,  $C_{12}$  and  $C_{44}$  as shown on the matrix. Alers and Neighbours, (1957) investigated that for cubic materials, the inequalities arising from the fact that the principal minor determinants are positive are that  $C_{11} + 2C_{12}$  and  $\frac{1}{2}(C_{11} - C_{12})$  are positive. From these two relations then, equations (3.19) are obtained. These then make up the necessary stability conditions for materials in the cubic phase as reported by Hou, (2008); Li *et al.*, (2017); Mouhat and Coudert (2014);

$$\begin{aligned} C_{11} - C_{12} &> 0, \\ C_{11} + 2C_{12} &> 0, \end{aligned}$$

$$C_{44} > 0 \quad (3.19)$$

Tetragonal phases have six independent elastic constants, that is,  $C_{11}$ ,  $C_{12}$ ,  $C_{13}$ ,  $C_{33}$ ,  $C_{44}$  and  $C_{66}$ . The elastic constant matrix for the tetragonal phases is given by equation (3.20).

$$\begin{pmatrix} C_{11} & C_{12} & C_{13} & & & \\ C_{12} & C_{11} & C_{13} & & & \\ C_{13} & C_{13} & C_{33} & & & \\ & & & C_{44} & & \\ & & & & C_{44} & \\ & & & & & C_{66} \end{pmatrix} \quad (3.20)$$

From the relations that arise, a tetragonal material is regarded mechanically stable if equations (3.21) from Dong *et al.*, (2013); Mouhat and Coudert, (2014) are met;

$$\begin{aligned} C_{11} &> |C_{12}|, \\ 2C_{13}^2 &< C_{33}(C_{11} + C_{12}), \\ C_{44} &> 0, \\ C_{66} &> 0 \end{aligned} \quad (3.21)$$

Finally, for a trigonal structure, the elastic constant matrix is given by equation (3.22)

$$\begin{pmatrix} C_{11} & C_{12} & C_{13} & C_{14} & & \\ C_{12} & C_{11} & C_{13} & -C_{14} & & \\ C_{13} & C_{13} & C_{33} & & & \\ C_{14} & -C_{14} & & C_{44} & & \\ & & & & C_{44} & C_{14} \\ & & & & C_{14} & C_{66} \end{pmatrix} \quad (3.22)$$

Trigonal phases have seven independent elastic constants, that is,  $C_{11}$ ,  $C_{12}$ ,  $C_{13}$ ,  $C_{14}$ ,  $C_{33}$ ,  $C_{44}$  and  $C_{66}$ . In this case,  $C_{66} = (C_{11} - C_{12})/2$ . The stability conditions for trigonal phases are given by equation (3.23) as reported by Liu *et al.* (2016); Mouhat and Coudert, (2014)

$$\begin{aligned} C_{11} &> |C_{12}|, \\ C_{44} &> 0, \quad C_{33} > 0, \quad C_{11} > 0 \\ C_{13}^2 &< \frac{1}{2} C_{33} (C_{11} + C_{12}) \\ [(C_{11} - C_{12}) C_{44} - 2C_{14}^2] &> 0 \equiv C_{44} C_{66} \end{aligned} \quad (3.23)$$

After the calculation of the elastic constants, the moduli are calculated using the Reuss approximation in Liu *et al.* (2016) and Voigt approximation as reported by Shiferaw and Woldemariam, (2019); Liu *et al.*, (2016). The average of the Reuss and Hill approximation are then obtained from the Hill averaging scheme (Hill, 1932). From the elastic constants ( $C_{ij}$ ) and

using the Voigt theory Voigt (1910), the bulk  $B_V$  and shear  $G_V$  moduli are given by equations (3.24) and (3.25), respectively (Dong *et al.*, (2013).

$$B_V = \frac{1}{9} [(C_{11} + C_{22} + C_{33}) + 2(C_{12} + C_{23} + C_{31})] \quad (3.24)$$

$$G_V = \frac{1}{15} [(C_{11} + C_{22} + C_{33}) - (C_{12} + C_{23} + C_{31}) + 3(C_{44} + C_{55} + C_{66})] \quad (3.25)$$

From the Reuss theory Reuss, (1929), the bulk  $B_R$  and shear  $G_R$  moduli are obtained from the elastic constants using equations (3.26) and (3.27), respectively.

$$\frac{1}{B_R} = (S_{11} + S_{22} + S_{33}) + 2(S_{12} + S_{23} + S_{31}) \quad (3.26)$$

$$\frac{15}{G_R} = 4(S_{11} + S_{22} + S_{33}) - 4(S_{12} + S_{23} + S_{31}) + 3(S_{44} + S_{55} + S_{66}) \quad (3.27)$$

The  $S_{ij}$  are the elastic compliances. The elastic compliance matrix is the inverse of the elastic constant matrix, that is, as in equation (3.28)

$$S = C^{-1} \quad (3.28)$$

Where  $S$  is the elastic compliances matrix and  $C$  is the elastic constant matrix. From the Hill averaging scheme, the bulk  $B_H$  and shear  $G_H$  moduli are given by the average of the two theories, that is equation (3.29) and (3.30), respectively.

$$B_H = \frac{B_V + B_R}{2} \quad (3.29)$$

$$G_H = \frac{G_V + G_R}{2} \quad (3.30)$$

From the Pugh method (Dong *et al.* 2013; Pugh, 1954) the ductility or brittleness of a material can be obtained by checking the relation of  $\frac{B}{G}$  to the critical value of 1.75. If the ratio  $\frac{B}{G}$  is more than the value, the material is considered ductile and vice versa. After calculating the elastic constants and the moduli, the Poisson's ratio and the Youngs modulus are obtained from the shear and bulk moduli using equations (3.31) and (3.32), respectively (Dong *et al.*, 2013; Hou, 2008).

$$\nu = \frac{3B_H - 2G_H}{2(3B_H + G_H)} \quad (3.31)$$

$$E_H = \frac{9B_H G_H}{(3B_H + G_H)} \quad (3.32)$$

The degree of anisotropy of materials aids in explaining the bonding between atoms in different planes. The anisotropy indices calculated are the shear ( $A_1, A_2, A_3$ ) and the Zener's ( $A_Z$ ) anisotropic factors. Materials with indices equal to unity are isotropic and anisotropic otherwise. The deviation from unity gives the materials' degree of anisotropy. For the shear anisotropic factors,  $A_1$  gives the measure in the {100} planes between the  $\langle 101 \rangle$  and  $\langle 001 \rangle$  directions,  $A_2$  in the {010} planes between the  $\langle 101 \rangle$  and  $\langle 001 \rangle$  directions and  $A_3$  gives the measure in the {001} planes between the  $\langle 110 \rangle$  and  $\langle 010 \rangle$  directions. The anisotropic factors are given by equations 3.33-3.36.

$$A_1 = \frac{4C_{44}}{C_{11} + C_{33} - 2C_{13}} \quad (3.33)$$

$$A_2 = \frac{4C_{55}}{C_{22} + C_{33} - 2C_{23}} \quad (3.34)$$

$$A_3 = \frac{4C_{66}}{C_{11} + C_{22} - 2C_{12}} \quad (3.35)$$

$$A_Z = \frac{2C_{44}}{C_{11} - C_{12}} \quad (3.36)$$

The hardness of the materials was measured using Vickers hardness, which is given by equation 3.37.

$$H_V = \frac{(1 - 2\nu)E_H}{6(1 + \nu)} \quad (3.37)$$

The machinability index is crucial in determining the mechanical properties of materials. It is used to measure the hardness of materials and indicates how easily a material can be cut and machined during engineering processes. Materials with a high machinability index are hard and not easy to cut through, indicating that they would require more time to produce finely finished surfaces. The machinability index is given by equation 3.38

$$\mu_M = \frac{B}{C_{44}} \quad (3.38)$$

The Cauchy pressure, Poisson ratio and the Pugh's criterion are used to identify ductility or brittleness in materials with great accuracy. From the Poisson's ratio, materials with  $\nu > 0.26$  are



ductile while those with  $\nu < 0.26$  are brittle. The Cauchy pressure is calculated by  $(C_{12} - C_{44})$ . Materials with a positive value of the Cauchy pressure are ductile while those with a negative value are considered brittle.

### 3.11.1: Bulk modulus and its pressure derivative

The bulk modulus measures the resistance of a material to compression. The volume and bulk modulus of materials are inversely related as reported by (Singh and Dwivedi, 2012). The bulk modulus is given by equation (3.39)

$$B = -V \frac{\partial P}{\partial V} \quad (3.39)$$

Where  $B$  is the bulk modulus,  $V$  the volume and  $P$  is the pressure. The pressure is given by equation (3.40).

$$P = -\frac{\partial E}{\partial V} \quad (3.40)$$

Equation (3.40) then reduces equation (3.39) into equation (3.41)

$$B = V \frac{\partial^2 E}{\partial V^2} \quad (3.41)$$

The pressure derivative of the bulk modulus is given by equation (3.42).

$$B' = \frac{\partial B}{\partial P} = \frac{1}{B} \left( V \frac{\partial}{\partial V} \left( V \frac{\partial^2 E}{\partial V^2} \right) \right) \quad (3.42)$$

### 3.12: Electronic Properties

The electronic properties studied in this work were the electronic band gap and density of states. These properties are crucial in knowing how the material interacts in the electronic level and this helps in understanding the material in the larger scale (Saikia *et al.*, 2022).

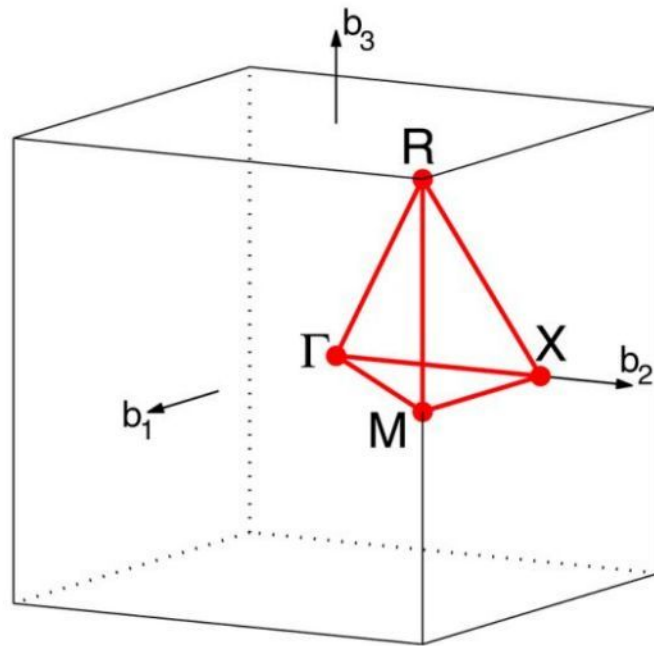


Figure 3. 7 First Brillouin zones of the cubic lattice. The  $k$ -path followed is  $\Gamma - X - M - \Gamma - R - X|M - R$ ., Setyawan and Curtarolo, (2010)

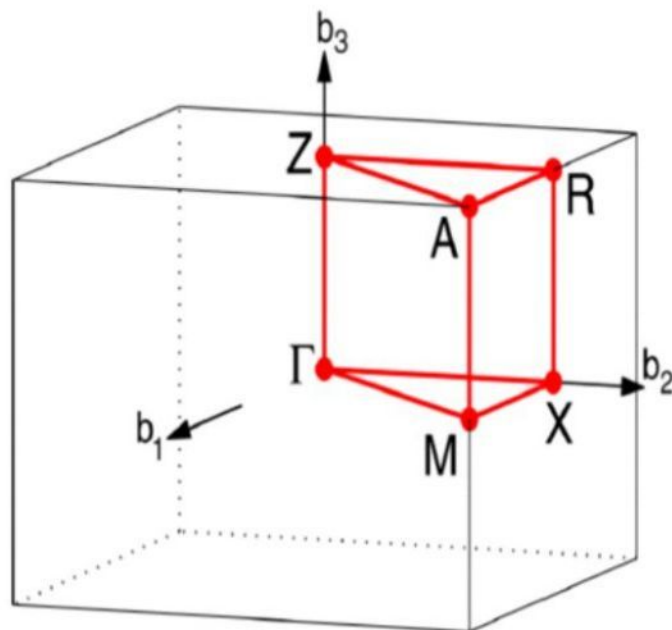
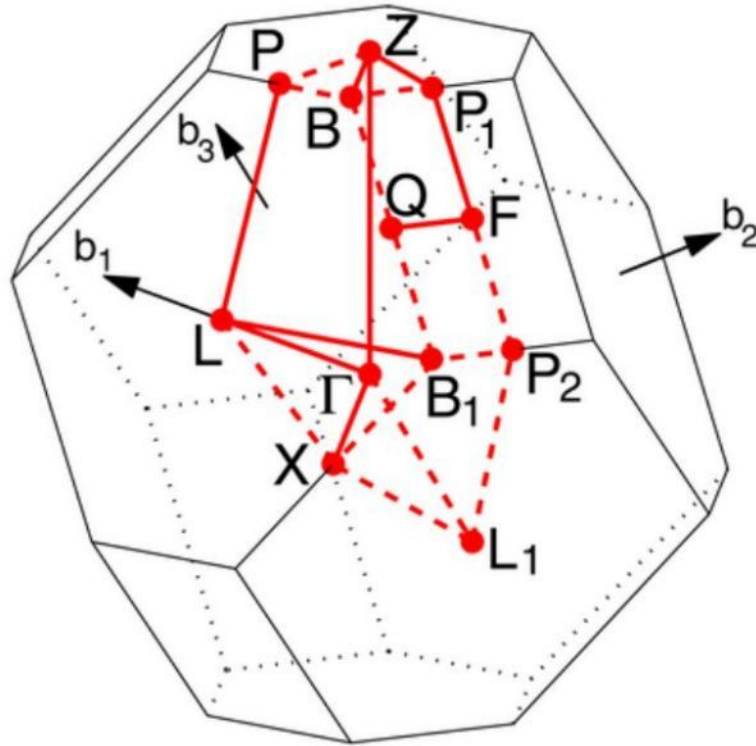


Figure 3. 8 First Brillouin zones of the tetragonal lattice. The  $k$ -path followed is  $\Gamma - X - M - \Gamma - Z - R - A - Z|X - R|M - A$ , Setyawan and Curtarolo, (2010)



**Figure 3. 9 First Brillouin zones trigonal lattice. The  $k$ -path followed is  $\Gamma - L - B_1B - Z - \Gamma - X|Q - F - P_1 - Z|L - P$  Setyawan and Curtarolo, (2010)**

The respective band gaps for the materials are calculated from the obtained band structure information. The electronic density of states is important in describing the number of states at each energy level that are available to be occupied by electrons. This characteristic is crucial in modern electronic structure theory (Mahmoud *et al.*, 2020). To obtain the number of available states in a material, that is, the density of states, we consider the electrons occupying the solid as a free electron gas. Then by representing the state of the electron as a vector in the reciprocal  $k$ -space, the energy of the electron becomes as in equation (3.43)

$$E = \frac{\hbar^2}{2m}(k_x^2 + k_y^2 + k_z^2) = \frac{\hbar^2|k|^2}{2m} \quad (3.43)$$

Where is the  $E$  energy,  $m$  the mass,  $\hbar$  the reduced Planck's constant and  $k_x$ ,  $k_y$  and  $k_z$  are the coordinates in  $k$  space. The visualization of the electrons in reciprocal space for a spherical surface is given in figure 3.10.

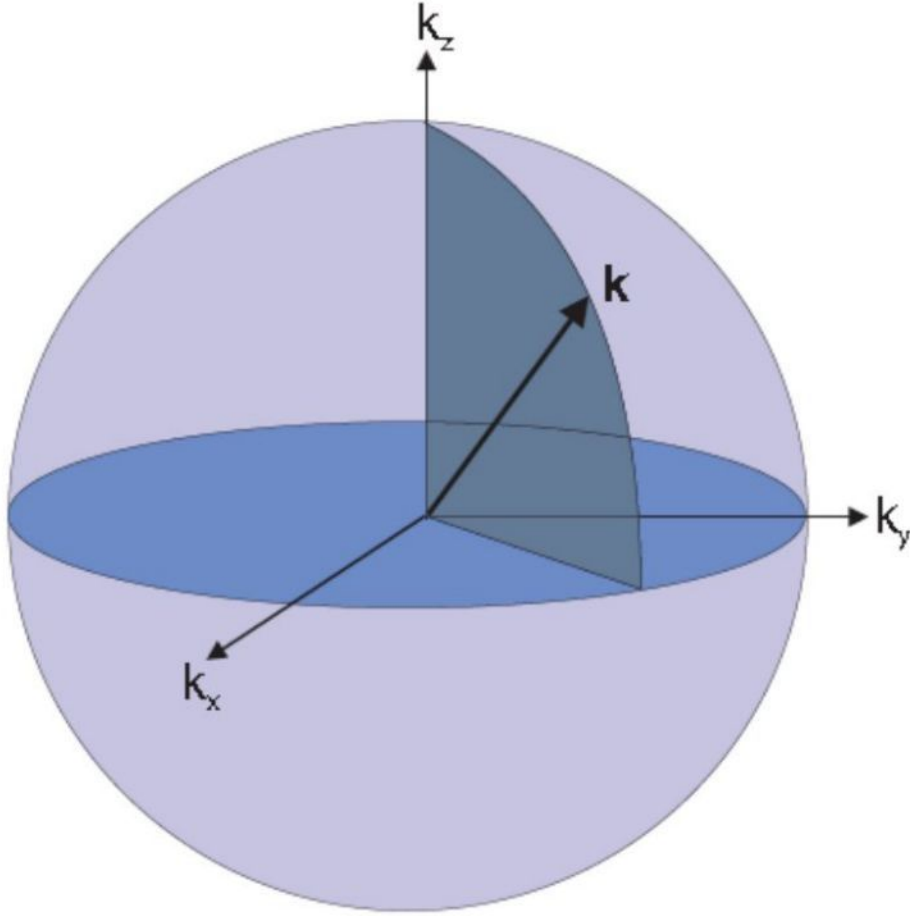


**Figure 3.10:** The spherical surface in  $k$ -space for electrons in 3D.  $k_x$ ,  $k_y$  and  $k_z$  give the coordinates in the  $x$ ,  $y$  and  $z$  directions, respectively

The total density of solids is given by equation (3.44).

$$g(E) = \frac{2}{V_{BZ}} \sum_{n_B} \int_{\Omega^1} \delta(E - E_{n_B}(\mathbf{k})) d\mathbf{k} \quad (3.44)$$

Where  $g(E)$  is the density of states,  $V_{BZ}$  is the volume of the Brillouin zone,  $n_B$  is the band index and  $\Omega^1$  is the volume of the unit cell in the reciprocal space.

### 3.13: Optical Properties

The optical properties were studied as a function of the energy in eV with the energy range from (0-20 eV). The study of the optical properties is crucial in photovoltaics since it explains how a material behaves with light (Saikia *et al.*, 2022.). To study the optical properties, the complex dielectric function is investigated (Mbilo *et al.* 2022). This function is dependent on the electronic band structure of the given material and affects its properties (Kittel, 2005). By obtaining the

dielectric function, the band behavior of solids can be extensively investigated (Amin *et al.*, 2011). From the dielectric function, the other optical properties of the material like the refractive index, reflectivity, absorption coefficient and the extinction index can be obtained. Like all complex functions, the dielectric function is made up of the real and imaginary part (Mulwa *et al.*, 2016) and is given by equation (3.45) Amin *et al.*, 2011; Hamideddine *et al.*, 2020; Tian *et al.*, 2017).

$$\mathcal{E} = \varepsilon_1(\omega) + i\varepsilon_2(\omega) \quad (3.45)$$

Where  $\varepsilon_1(\omega)$  is the real part and  $\varepsilon_2(\omega)$  is the imaginary part.  $\varepsilon_1(\omega)$  can be obtained by using the Kramers- Kronig relation as described by (Butt *et al.*, 2021; Kumar *et al.*, 2014) as in equation (3.46).

$$\varepsilon_1^\omega = 1 + \frac{2}{\pi} P \int_0^\infty \frac{\varepsilon_2(\omega^1)\omega^1}{\omega^{12} - \omega^2 + i\eta} d\omega^1 \quad (3.46)$$

The imaginary part,  $\varepsilon_2(\omega)$ , is then obtained after the real part is found. The two indices, that is, the refractive index and the extinction index, are related to the reflectivity at normal by equation (3.47) (Kittel, 2005)

$$R(\omega) = \frac{n + iK - 1}{n + iK + 1} \quad (3.47)$$

In this case,  $n(\omega)$  is the refractive index,  $K(\omega)$  the extinction index and  $R(\omega)$  is the reflectivity. In relation to the dielectric function  $\mathcal{E}(\omega)$ , the refractive and extinction indices have the relationship in equation (3.48) Kittel, (2005)

$$\sqrt{\mathcal{E}(\omega)} \equiv n(\omega) + iK(\omega) \equiv N(\omega) \quad (3.48)$$

Where  $N(\omega)$  is the complex function of  $\mathcal{E}(\omega)$ . The optical absorption coefficient  $\alpha(\omega)$  measures how light penetrates into a material at different energies Roknuzzaman *et al.*, (2017).  $\alpha(\omega)$  can be obtained from  $\varepsilon_1(\omega)$  and  $\varepsilon_2(\omega)$  using the equation (3.49),

$$\alpha(\omega) = \sqrt{2}\omega \left( \sqrt{\varepsilon_1^2(\omega) + \varepsilon_2^2(\omega)} - \varepsilon_1(\omega) \right)^{\frac{1}{2}} \quad (3.49)$$

the refractive index  $n(\omega)$ , which measures the banding of light in different media, is given by equation (3.50)

$$n(\omega) = \left( \frac{\sqrt{\varepsilon_1^2(\omega) + \varepsilon_2^2(\omega)} + \varepsilon_1(\omega)}{2} \right)^{\frac{1}{2}} \quad (3.50)$$

the reflectivity  $R(\omega)$  is given by equation (3.51)

$$R(\omega) = \frac{(n - 1)^2 + K^2}{(n + 1)^2 + K^2} \quad (3.51)$$

the exciton index  $K(\omega)$  as in equation (3.52) Saikia *et al.*, (2022).

$$K(\omega) = \left( \frac{\sqrt{\varepsilon_1^2(\omega) + \varepsilon_2^2(\omega)} - \varepsilon_1(\omega)}{2} \right)^{\frac{1}{2}} \quad (3.52)$$

The energy loss, which measures the amount of energy lost through absorption, scattering, radiation and other causes is given by equation (3.53) Saikia *et al.*, (2022.)

$$L(\omega) = \frac{\varepsilon_2(\omega)}{\varepsilon_1^2(\omega) + \varepsilon_2^2(\omega)} \quad (3.53)$$

## CHAPTER FOUR: MATERIALS AND METHODS

### 4.1 : Introduction

This chapter deals with the computational methods that were carried out on the  $KGeX_3$  ( $X=Cl, Br$ ) perovskite materials.

### 4.2 : Computational Methods

Calculations were done within the plane wave basis set implemented in Q.E code with GGA-PBE. (Perdew *et al.*, 1996) and the GW as the exchange-correlation approximations employed. The GW approximation was used to correct the band gaps obtained from the GGA-PBE approximations. GGA-PBE was the preferred exchange correlational functional because it contains more physical information hence more accurate than the LDA. The GGA-PBE was also more compatible with Q.E since methods like Hubbard\_U could not be used because the germanium atom was not compatible with the Hubbard term U. The Crystallographic Information Files (CIF) were downloaded from the Materials Project website (Jain *et al.*, 2013). After which they were used to obtain the input files from the Materials Cloud website (Talirz *et al.*, 2020). All the calculations were submitted to the Centre for High-performance Computing (CHPC) cluster in Cape Town South Africa (S.A). The Quantum ESPRESSO Code is utilized in materials modeling from the first principles and predicting the properties of materials (Giannozzi *et al.*, 2009; Malakkal *et al.*, 2015). The term ESPRESSO is coined from opEn-Source Package for Research in Electronic Structural, Simulation and Optimization. Being an open-source code, it has attracted wide usage in Physics, Chemistry and other research fields. The code has advantage over other codes in that, it comprises several softwares, for example, pw.x, ph.x, kpoint.x, cif2cell.x, etc., and other auxiliary softwares like Xmgrace, XCrySDen, Vesta, GNUplot, etc. enabling a wide scope of calculations to be done. Quantum ESPRESSO is a plane-wave based code where the PWscf is used in solving the Kohn-Sham equation to get an exact density from the exchange-correlation potential. Density is a scalar field quantity in space and can never be exact because the exchange-correlation potential is an approximation, therefore the self-consistent field calculations are computed until minimum energy is achieved. Before characterization was done, structural optimizations were carried out by performing convergence tests to the  $k$ -points, ecut and the lattice constant.  $k$ -points optimization was done by varying the  $k$ -points mesh from  $2 \times 2 \times 2$  to a denser mesh of  $24 \times 24 \times 24$  at intervals of  $2 \times 2 \times 2$ . The converged value for the  $k$ -points was used in the calculation of kinetic energy (ecut) convergence. The ecut convergence was done as a function of the total energy in Ry.



The values obtained from the  $k$ -points and *ecut* convergence were then used for the lattice constant optimization. The equilibrium bulk modulus and its pressure derivative were obtained by fitting the Murnaghan EoS to the lattice constants and their respective energy values using the *ev.x* command within QE. The band structure calculations were done by using high symmetry points instead of the normal Monkhorst and Pack mesh that was used in the convergence and lattice parameter calculations. The high symmetry points for each material were obtained from the Materials Project site (Hinuma *et al.*, (2017; Togo and Tanaka, 2018). These special points for each of the materials are shown in figure 3.7 - 3.9 (Setyawan and Curtarolo, 2010).  $\epsilon_1(\omega)$  and  $\epsilon_2(\omega)$ , the real and imaginary parts of the dielectric constant, were calculated using *thermo\_pw*, a Q.E package. Equations (3.46) – (3.53) were used to obtain the optical properties from the complex dielectric function. Mechanical stability of the materials was checked using the elastic constants, which were calculated using *thermo\_pw*. Other elastic properties such as the Cauchy pressure, Vickers hardness, machinability, anisotropy, shear and bulk moduli were derived from the elastic constants.

### 4.3: The Quantum ESPRESSO Input File

The input file varies from the calculation being done i.e., whether it is for self-consistent field (scf) or band structure calculation or variable cell (vc) relax calculation for relaxing and optimizing the structure and contains the parameters needed for the *ab initio* calculations. Periodic elements were accessed from the Materials project site by downloading the required elements after which DFT parameters such as the formation energy, volume, density and band gap were generated of the various forms of the compound under study. Selecting a particular structure then generated all the information about the structure including the lattice parameters, stability and the phonon dispersion graphs. Figure 4.1 shows a typical input file. From the Figure 4.1, the first image shows the input file and the flow chart shows how the K-S equations were calculated in Q.E. The `&control`, `&system` and `&electrons` are called name-lists and the atomic species, atomic positions and  $k$ -points are the input cards. `&Control` specifies the flux of computation, the `&system` gives the specific system, the atomic species specifies the atom and the pseudopotential file used. The atomic position shows where the atoms are located (Hung *et al.* 2018).



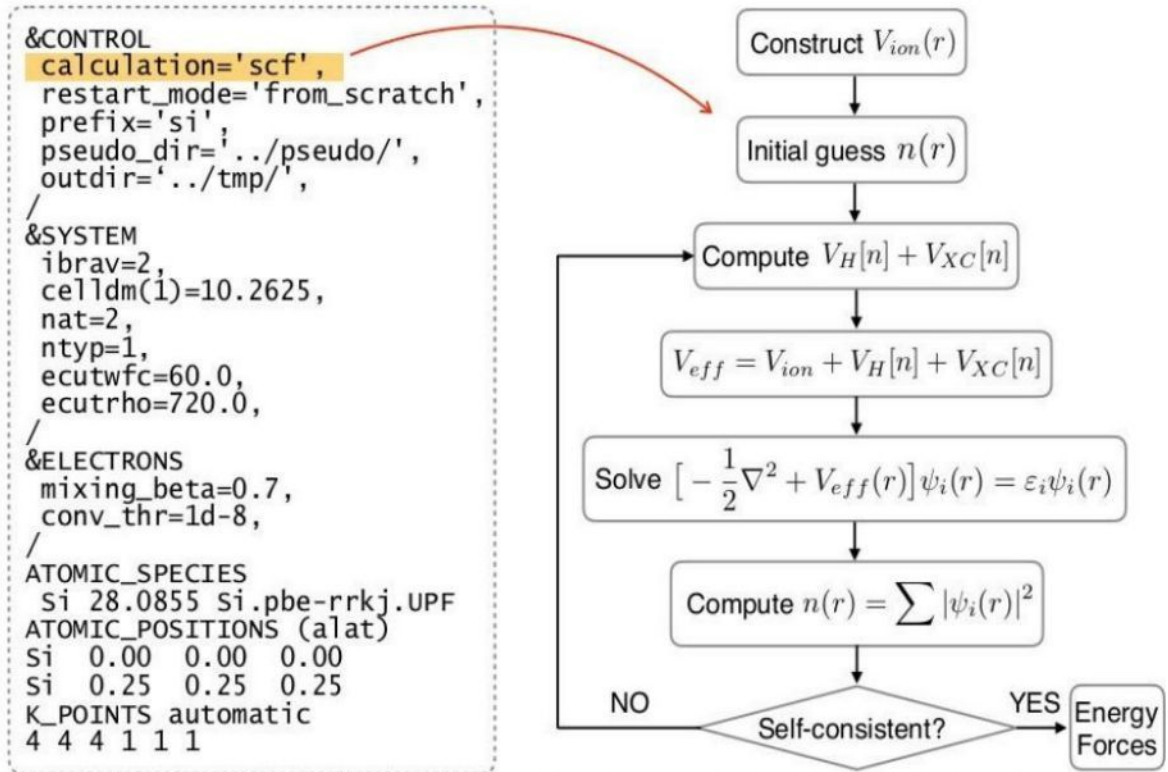


Figure 4.2 A Quantum ESPRESSO input file relating to the Kohn-Sham self-consistency scheme. Hung et al, (2018)

## CHAPTER FIVE: RESULTS AND DISCUSSIONS

### 5.1: Introduction

Results obtained from the structural, elastic, electronic and optical property calculations are discussed in this chapter. This is followed through with the analysis and discussions of the same.

### 5.2: Structural Properties

Understanding the structural properties of materials is important in their characterization and optimization for different applications. The structural properties investigated in this work are the lattice constant, equilibrium volumes, the bulk modulus and the first derivative. Convergence tests were carried out first before any other structural calculations were done.

#### 5.2.1: *k*-points convergence

The converged *k*-points for all the materials were found to be 8x8x8 and are shown in Figure 5.1(a-c). Although any value above 8x8x8 could have been used, it is important to choose a *k*-points mesh that is not too high because the higher the *k*-point grid chosen, the denser the structure becomes making the calculations computationally expensive, even though the results would be accurate. This then means that one should strike a balance between the computational cost and the accuracy. The value of *k*-points used for the calculations is shown marked with the red circles in the optimization figures 5.1(a-c).

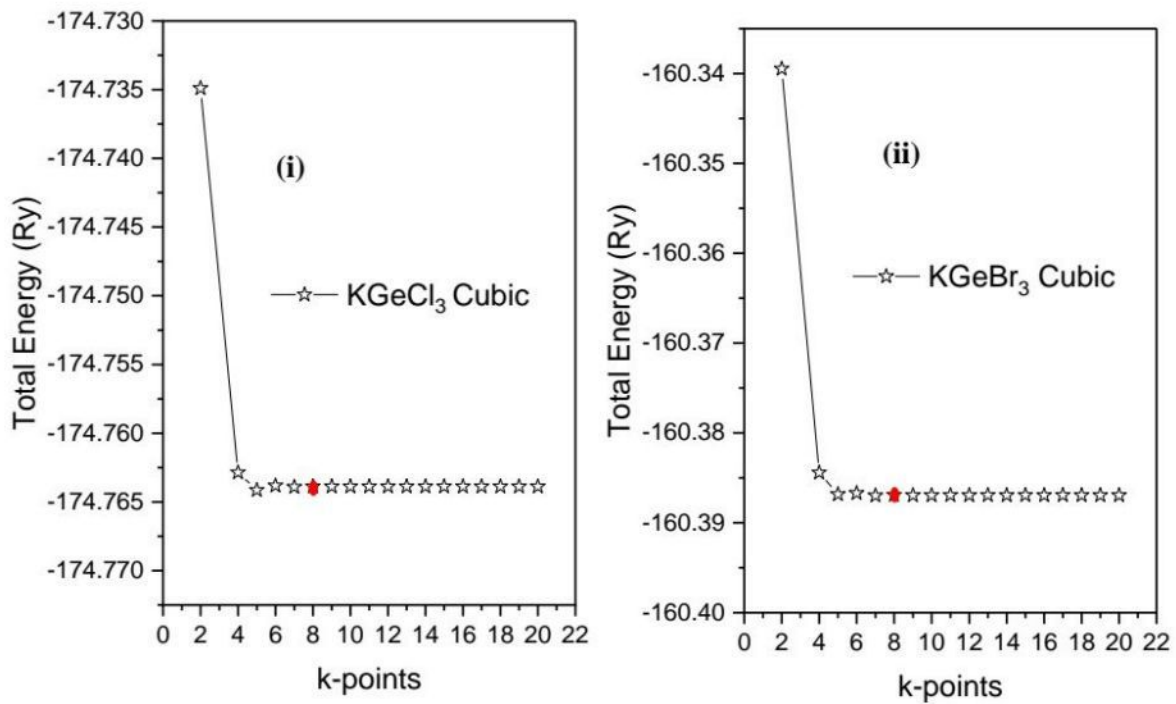


Figure 5.1 a: k-points convergence for the (i) KGeCl<sub>3</sub> and (ii) KGeBr<sub>3</sub> perovskite materials in the cubic phase

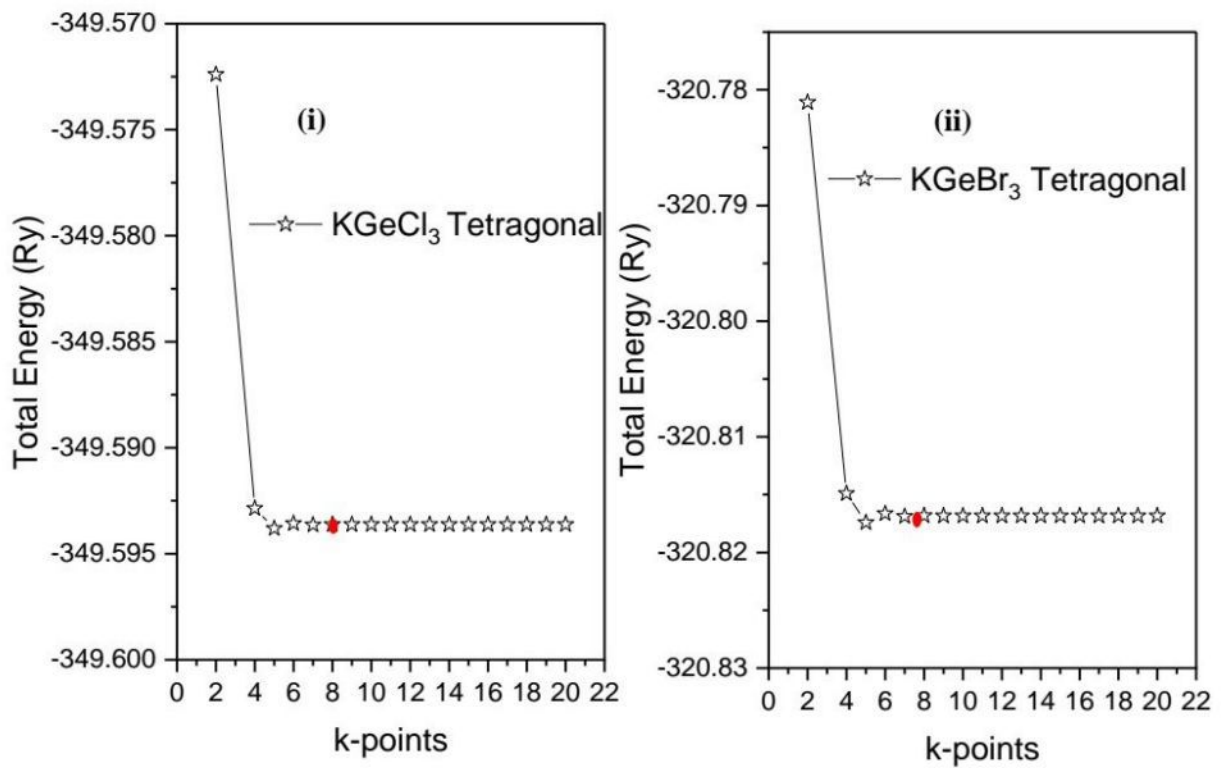


Figure 5.1 b: k-points convergence for the (i) KGeCl<sub>3</sub> and (ii) KGeBr<sub>3</sub> tetragonal perovskites

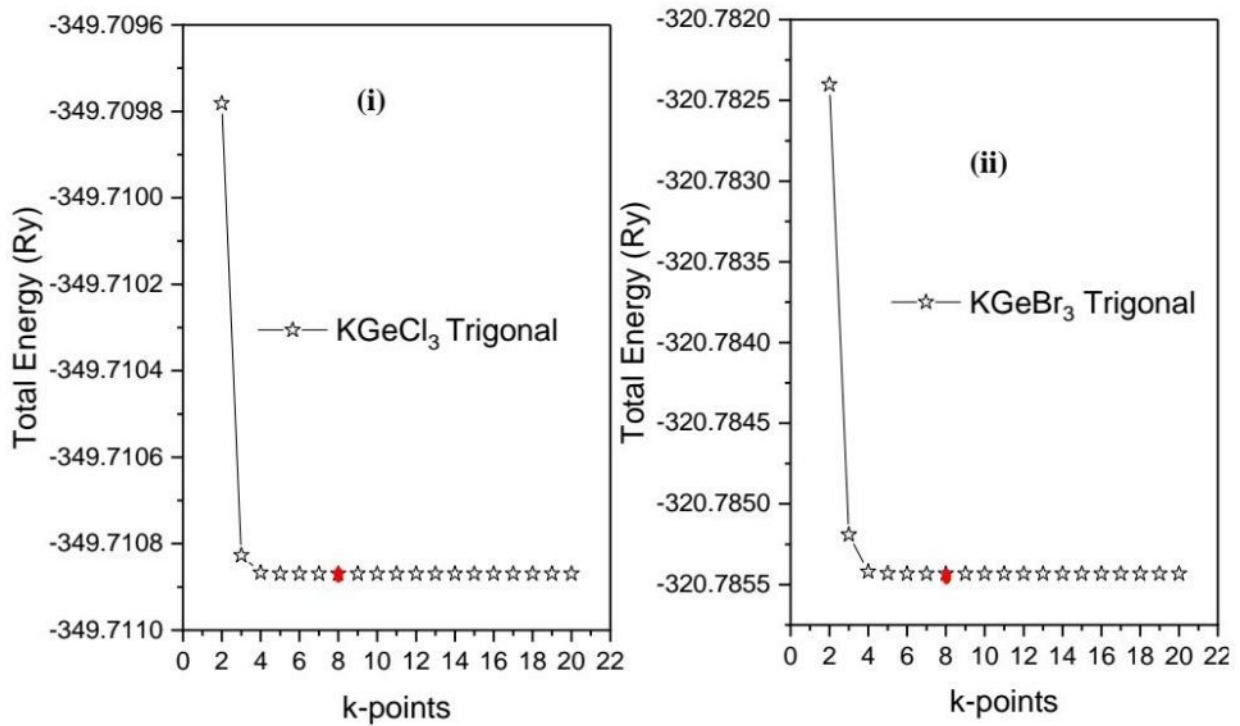


Figure 5.1 c: *k*-points convergence for the (i) KGeCl<sub>3</sub> and (ii) KGeBr<sub>3</sub> trigonal perovskites

### 5.2.2: Energy cutoff (ecut) convergence

The energy associated with the plane wave basis is important in computational research methods. Unlike in the *k*-points convergence, using higher ecut values only increases the computational time but does not guarantee increase in the accuracy. For all the materials, convergence was achieved at 100Ry since the energy remained unchanged beyond this point and is represented in Figure 5.2 (a-c), with the red circles showing the converged value of the ecut.

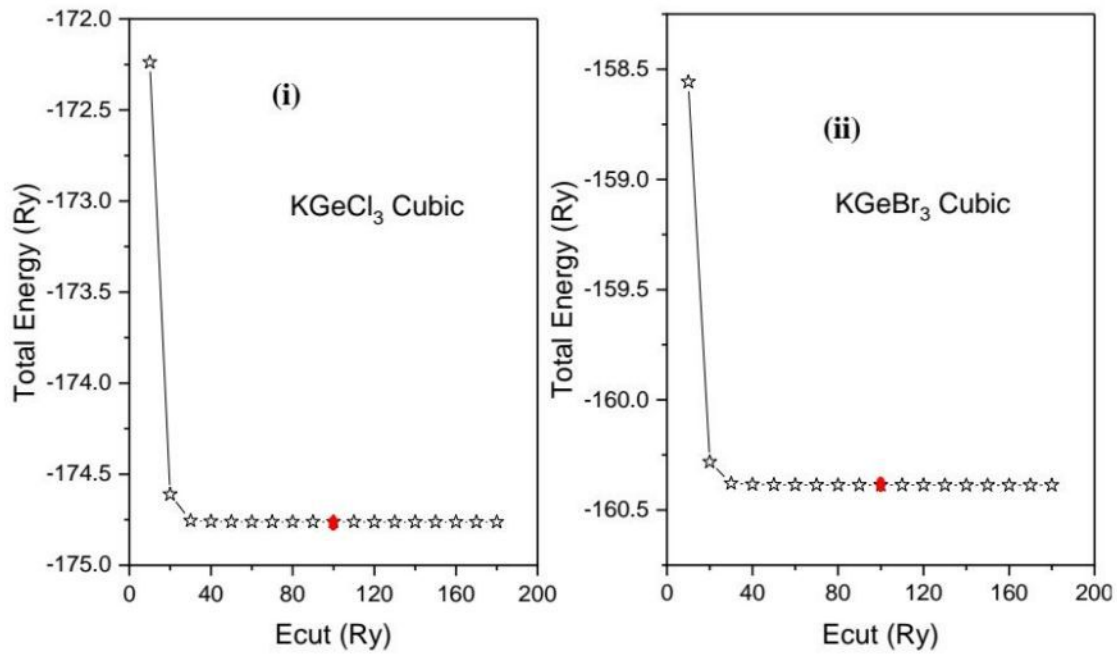


Figure 5. 2 a: Ecut convergence for the (i)  $KGeCl_3$  and (ii)  $KGeBr_3$  cubic perovskites

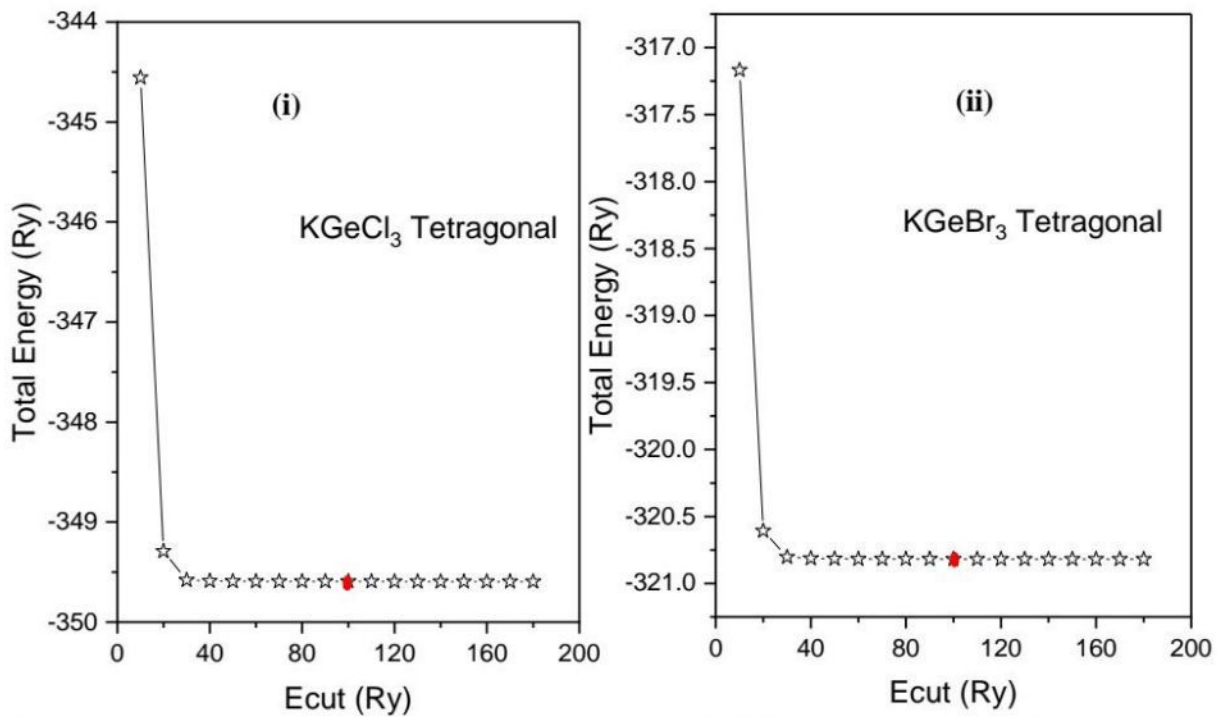


Figure 5. 2 b: Ecut convergence for the (i)  $KGeCl_3$  and (ii)  $KGeBr_3$  tetragonal perovskites

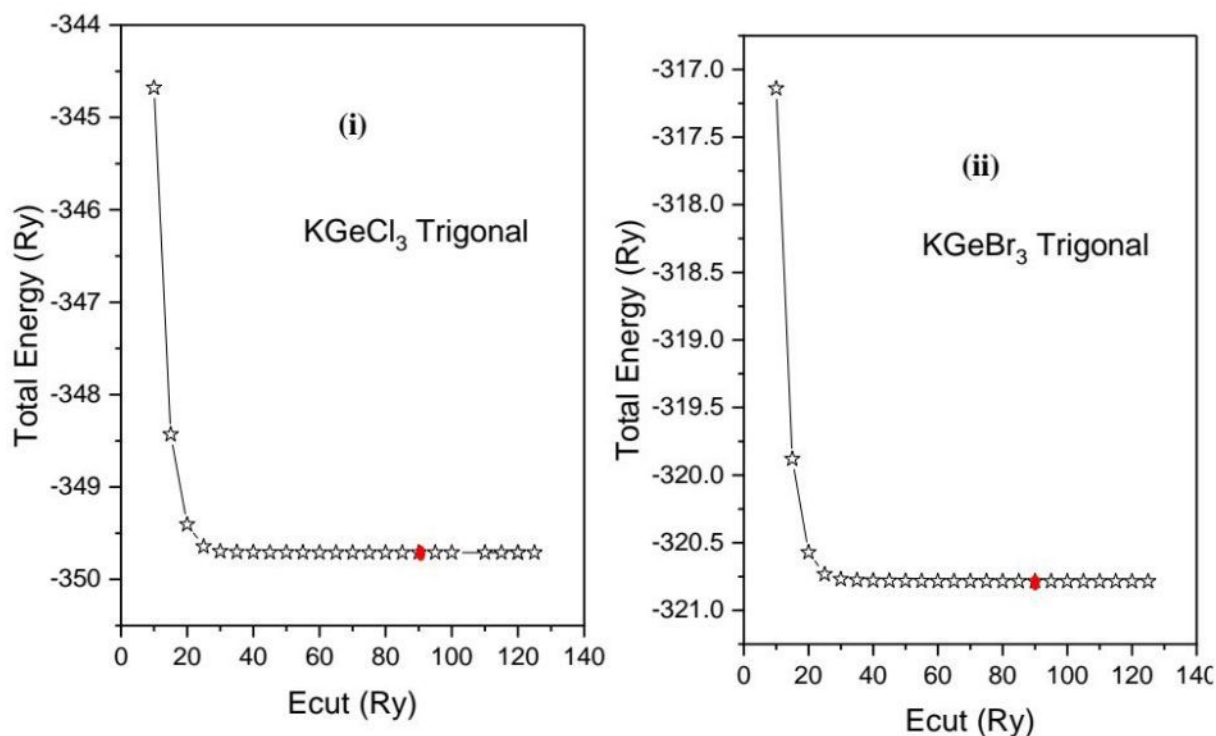


Figure 5. 2c: Ecut convergence for the (i) KGeCl<sub>3</sub> and (ii) KGeBr<sub>3</sub> trigonal perovskites

### 5.2.3: Lattice constant convergence

The length of the unit cell as a function of energy was investigated using GGA-PBE approximations and it was realized that convergence was achieved for all the materials. Table 5.1 shows the recorded values for the converged lattice constants. Optimization was achieved at the lowest energy points and this is indicated by the red circles in the graphs in figure 5.3(a-c)

**Table 5.1:** The obtained values for the lattice constant convergence tests for the KGeX<sub>3</sub> materials calculated using GGA-PBE approximation.

Material	Structure	Lattice constant (Bohr)
KGeCl <sub>3</sub>	Cubic	9.957
	Trigonal	14.426
	Tetragonal	13.799
KGeBr <sub>3</sub>	Cubic	10.467
	Trigonal	15.246
	Tetragonal	14.538



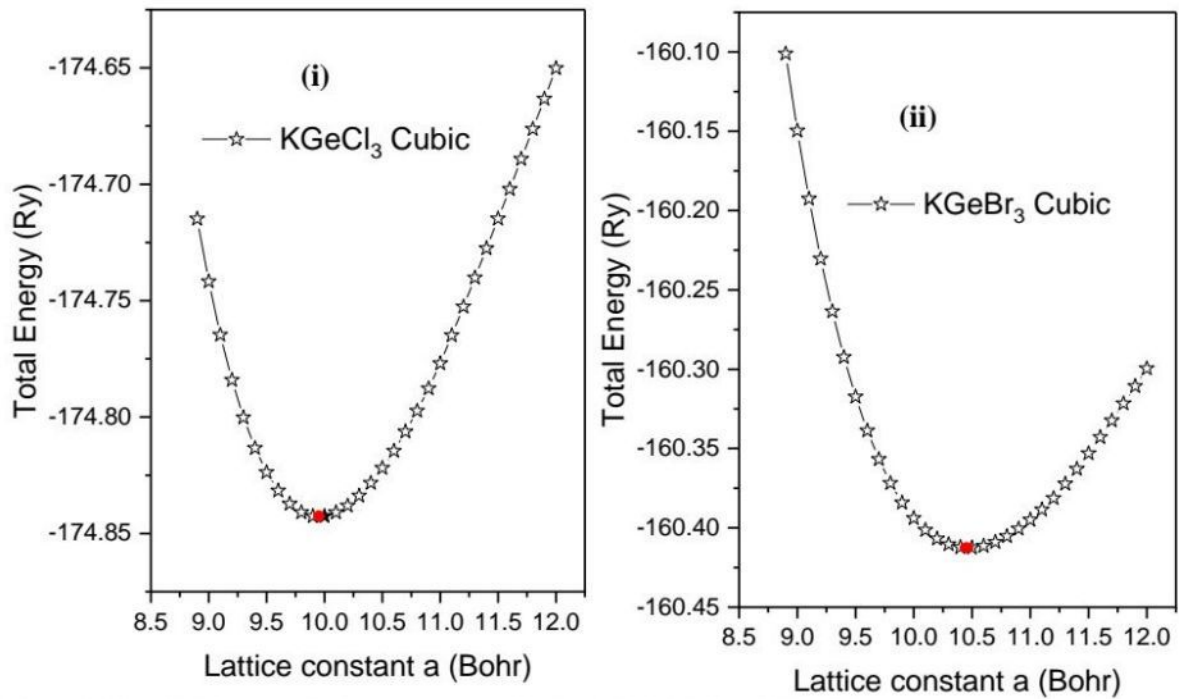


**Figure 5. 3a:** Lattice constant convergence for the (i)  $KGeCl_3$  and (ii)  $KGeBr_3$  cubic perovskites

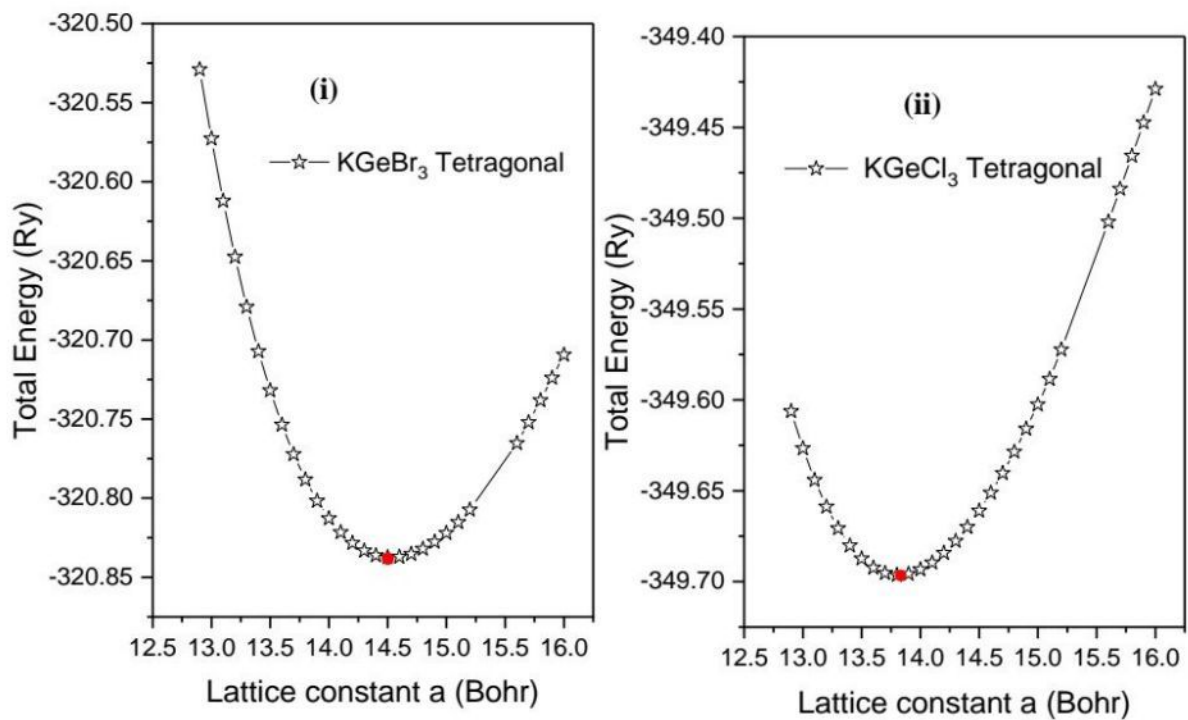


**Figure 5. 3b:** Lattice constant convergence for the (i)  $KGeBr_3$  and (ii)  $KGeCl_3$  tetragonal perovskites

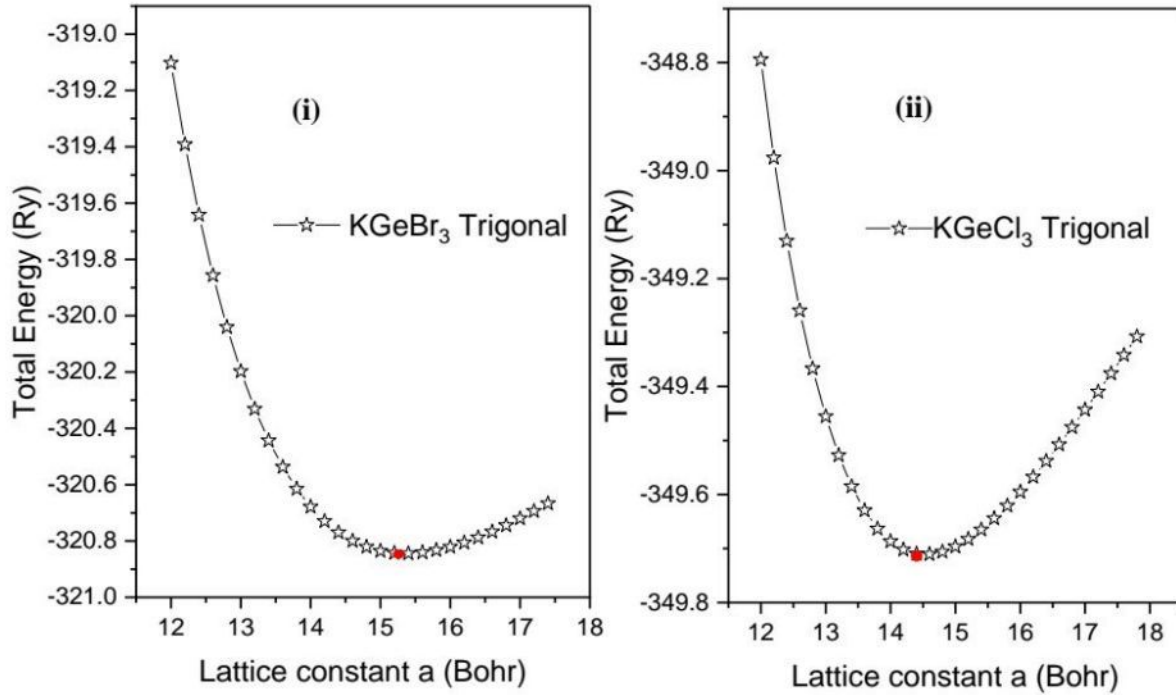


**Figure 5.3c: Lattice constant convergence for the (i)  $KGeBr_3$  and (ii)  $KGeCl_3$  trigonal perovskites**

The optimized lattice constants in Å for the perovskites in both experimental and DFT work are shown in the Table 5.2. From Table 5.2, the lattice constants are in agreement with previous work by Houari *et al.* (2020), Hamideddine *et al.* (2022) and Saikia *et al.* (2022.). The Goldschmidt Tolerance Factor (GTF) were calculated from equation (5.1).

$$t = \frac{r_A + r_X}{\sqrt{2}(r_B + r_X)} \quad (5.1)$$

The cubic structures had perfect fit of the cation K with the corner-sharing octahedra, having a GTF of unity. For the distorted perovskites, the tetragonal structures have the K cation being too small creating the octahedron tilting distortion. For the trigonal structures, because the GTF is more than unity, the K cation is too big in relation to the  $GeCl_6$  and  $GeBr_6$  octahedra making the octahedra to bulge outwards.

**Table 5. 2:** The calculated DFT- (GGE-PBE) lattice constants of the  $\text{KGeCl}_3$  materials in Å compared to previous work by (Hamideddine *et al.*, (2022); Houari *et al.*, (2020); Saikia *et al.*, (2020). and the respective tolerance factors.

Material	Cubic $Pm3m$		Tetragonal $P4mbm$		Trigonal $R3m$		GTF
	Our study	Previous work	Our study	Previous work	Our study	Previous work	
$\text{KGeCl}_3$	5.269	5.570 <sup>a</sup> 5.290 <sup>b</sup>	7.302	_____	7.634	_____	1.003 (Cubic) 0.957(Tetragonal) 1.069(Trigonal)
$\text{KGeBr}_3$	5.539	5.550 <sup>a</sup> 5.570 <sup>b</sup> 5.61 <sup>c</sup>	7.693	_____	8.068	_____	1.000 (Cubic) 0.959(Tetragonal) 1.069(Trigonal)

<sup>a</sup> (Houari *et al.*, 2020) <sup>b</sup>(Hamideddine *et al.*, 2022) <sup>c</sup>(Saikia *et al.*, 2022.)

#### 5.2.4: Murnaghan equation of States

From the Murnaghan EoS, the bulk modulus, its pressure derivative and the equilibrium volumes are shown in the Table 5.3. The minimum energies from the scf calculations and the Murnaghan equation are also included. From Table 5.3, the trigonal structures of both the  $\text{KGeCl}_3$  and  $\text{KGeBr}_3$  materials are stable because they occupy the lowest energies of -349.705 Ry and -320.846 Ry, respectively. Energetically stable materials are in their equilibrium positions hence do not decompose to any other structure. It was also noted that the trigonal  $R3c$  and tetragonal  $P4mbm$  have close energies for both the materials with the cubic structures having the highest energy of the three phases. The results show that the cubic structures had the lowest volumes, thus this led to the conclusion that the volume was increasing as the symmetry was deviating from the ideal cubic structure. Additionally, using the total energies, it was noted that for all the structures, the energy was increasing as the X anion changed from Cl to Br.

**Table 5.3:** The calculated DFT- (GGE-PBE) equilibrium volumes in  $\text{\AA}^3$ , minimum energies in Ry, bulk Modulus in GPa and its pressure derivative from Murnaghan EoS of the  $\text{KGeX}_3$  materials.

Material	Volume ( $V_0$ ) ( $\text{\AA}^3$ )	Bulk Modulus ( $B$ ) (GPa)	Pressure derivative ( $B'$ )	Minimum energy	
				Scf calc. (Ry)	Murnaghan EoS (Ry)
KGeCl <sub>3</sub> Trigonal	326.330	20.700	4.040	-349.711	-349.705
KGeCl <sub>3</sub> Cubic	145.010	25.800	4.590	-174.843	-174.842
KGeCl <sub>3</sub> Tetragonal	284.470	27.800	4.410	-349.696	-349.696
KGeBr <sub>3</sub> Trigonal	383.230	19.600	3.670	-320.843	-320.846
KGeBr <sub>3</sub> Cubic	170.880	22.100	3.900	-160.413	-160.412
KGeBr <sub>3</sub> Tetragonal	330.870	23.800	4.170	-320.837	-320.837

### 5.3: Elastic Properties

The elastic properties are necessary in determining the mechanical stability of materials. The mechanical stability is determined by checking that the elastic constants,  $C_{ij}$ , satisfy the Born stability criteria and are positive. Other elastic properties such as the bulk and shear moduli, the Young's and Poisson's ratios were calculated. Using equation (4.18), equation (4.20) and equation (4.22), the cubic, tetragonal and  $\text{KGeBr}_3$  trigonal perovskites satisfy the Born stability criterion hence are stable. For the  $\text{KGeCl}_3$  trigonal, the condition  $C_{11} > |C_{12}|$  is not met and the elastic constant  $C_{12}$  is negative, that is,  $C_{12} = -5.535$ . The Table 5.4 shows the values of the  $C_{ij}$  for the materials in GPa. There is no previous work reported in literature, to the best of our knowledge, for the materials regarding their mechanical properties.

**Table 5. 4:** The calculated elastic constants ( $C_{ij}$ ) of the  $KGeX_3$  materials in GPa using GGA-PBE approximations.

Material	$C_{11}$	$C_{12}$	$C_{13}$	$C_{22}$	$C_{23}$	$C_{33}$	$C_{44}$	$C_{55}$	$C_{66}$
KGeBr <sub>3</sub> Cubic	49.816	9.000	9.000	49.816	9.000	49.816	7.483	7.483	7.483
KGeCl <sub>3</sub> Cubic	56.165	9.118	9.118	56.165	9.118	56.165	8.339	8.339	8.339
KGeBr <sub>3</sub> Tetragonal	36.731	21.019	11.422	36.731	11.422	51.952	9.223	9.223	19.424
KGeCl <sub>3</sub> Tetragonal	43.844	25.028	14.084	43.844	14.084	60.639	10.590	10.590	22.296
KGeBr <sub>3</sub> Trigonal	12.118	5.116	3.486	12.118	3.486	6.201	7.271	7.271	3.501
KGeCl <sub>3</sub> Trigonal	2.058	-5.535	1.519	2.058	1.519	-0.890	5.990	5.990	3.797

The bulk and shear moduli in the Voigt and Reuss approximations and their averages in GPa are shown in the Table 5.5. The  $B_V$ ,  $G_V$ ,  $B_R$ ,  $G_R$ ,  $B_H$ ,  $G_H$  are obtained from equations (3.24) -(3.27), respectively. The bulk modulus results obtained from the Murnaghan EoS in Table 5.3 was found to corroborate with the moduli derived from the elastic constants in the case of tetragonal and cubic structures. From the MEoS, the calculated values of the bulk modulus were 22.100GPa and 25.800GPa for the KGeBr<sub>3</sub> and KGeCl<sub>3</sub> cubic perovskites, respectively, 23.800GPa and 27.800GPa for the KGeBr<sub>3</sub> and KGeCl<sub>3</sub> tetragonal perovskites, respectively and 19.600GPa and 20.700GPa for the KGeBr<sub>3</sub> and KGeCl<sub>3</sub> trigonal perovskites, respectively. The bulk modulus obtained from the MEoS and elastic property calculations were not the same in the case of trigonal structures.

**Table 5. 5:** The bulk ( $B_V, B_R, B_H$ ) and shear ( $G_V, G_R, G_H$ ) moduli of the  $\text{KGeX}_3$  materials in GPa under the Voigt, Reuss and Hill averaging schemes calculated using the GGA-PBE approximations.

Material	$B_V$	$B_R$	$B_H$	$G_V$	$G_R$	$G_H$
$\text{KGeBr}_3$ Cubic	22.605	22.605	22.605	12.653	10.022	11.338
$\text{KGeCl}_3$ Cubic	24.801	24.801	24.801	14.413	11.242	12.828
$\text{KGeBr}_3$ Tetragonal	23.683	23.596	23.639	13.011	11.173	12.092
$\text{KGeCl}_3$ Tetragonal	28.303	28.258	28.280	15.037	12.990	14.014
$\text{KGeBr}_3$ Trigonal	6.069	5.687	5.878	4.832	-1.261	1.785
$\text{KGeCl}_3$ Trigonal	-0.196	-1.742	-0.969	3.537	2.412	2.975

The Pugh criterion (Pugh, 1954), which is used to determine the ductile or brittle nature of materials was employed, where a material is ductile if  $n > \frac{B}{G}$  and brittle otherwise. The  $\frac{B}{G}$  ratios are 1.994, 1.933, 1.955, 2.018, 3.293 for the  $\text{KGeBr}_3$  and  $\text{KGeCl}_3$  cubic,  $\text{KGeBr}_3$  and  $\text{KGeCl}_3$  tetragonal and the  $\text{KGeBr}_3$  trigonal structures, respectively. This implies that these materials are ductile since they satisfy  $n > \frac{B}{G}$ . The  $\text{KGeCl}_3$  trigonal, whose ratio is -0.326 and way less than 1.75, is brittle. Using the critical value of the Poisson's ratio, the cubic and tetragonal structures have  $\nu > 0.26$  showing that they are ductile in nature. The bromide and chloride trigonal perovskites have  $\nu < 0.26$  indicating that they are brittle. The cubic and tetragonal structures also have positive values of the Cauchy pressure indicating ductility. From the calculations, the Pugh's criterion, Poisson ratio and the Cauchy pressure are consistent in identifying the tetragonal and cubic perovskites as ductile and the trigonal as brittle. For photovoltaic applications, this implies that the brittle trigonal structure would crack easily when used to make perovskite films for



solar cells hence unsuitable for photovoltaics. Table 5.6 shows the calculated  $\frac{B}{G}$ , Poisson's ratio, Cauchy pressure and Young's modulus of the materials.

**Table 5.6:** The Poisson's ratio ( $\nu$ ), Young's modulus  $E_H$  in GPa, Cauchy pressure and the  $\frac{B}{G}$  of the  $\text{KGeX}_3$  materials calculated using the GGA-PBE approximations.

Material	$\frac{B}{G}$	$\nu$	$E_H$	$C_{12} - C_{44}$
$\text{KGeBr}_3$ Cubic	1.994	0.283	29.093	1.517
$\text{KGeCl}_3$ Cubic	1.933	0.277	32.761	0.779
$\text{KGeBr}_3$ Tetragonal	1.955	0.281	30.970	11.796
$\text{KGeCl}_3$ Tetragonal	2.018	0.287	36.059	14.438
$\text{KGeBr}_3$ Trigonal	3.293	0.032	3.685	-2.155
$\text{KGeCl}_3$ Trigonal	-0.326	-0.049	5.657	-11.525

The anisotropy, machinability and hardness are given in table 5.7. The shear and Zener's anisotropic factors of the cubic perovskites are identical.  $A_1, A_2$  and  $A_z$  for all the materials are not equal to one, indicating that the materials are anisotropic in the respective directions. For  $A_3$ , the trigonal structures have  $A_3 = 1$  showing that the materials are isotropic in the  $\{001\}$  planes. The machinability index of the materials decreases as the material distorts to less structurally ideal phases, that is, from cubic-tetragonal-trigonal, with trigonal structures having the lowest machinability index.

**Table 5.7:** The anisotropy factors, machinability and hardness of the perovskite materials calculated using the GGA-PBE approximations.

Material	$A_1$	$A_2$	$A_3$	$A_z$	$\mu_M$	$H_V$
KGeBr <sub>3</sub> Cubic	0.367	0.367	0.367	0.367	3.021	1.640
KGeCl <sub>3</sub> Cubic	0.354	0.354	0.354	0.354	2.974	1.907
KGeBr <sub>3</sub> Tetragonal	0.560	0.560	2.473	1.174	2.563	1.768
KGeCl <sub>3</sub> Tetragonal	0.558	0.558	2.4161	1.148	2.670	1.994
KGeBr <sub>3</sub> Trigonal	2.563	2.563	1.000	2.077	0.808	0.557
KGeCl <sub>3</sub> Trigonal	-12.813	-12.813	1.000	1.578	-0.162	1.089

#### 5.4: Electronic Properties

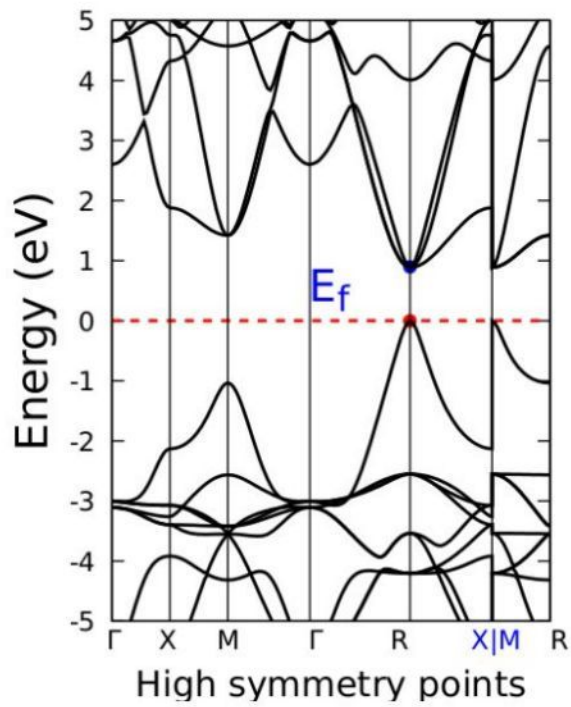
The electronic properties investigated were the partial density of states (PDOS) and band structure. Figure 5.4 (a-f) shows the results of the electronic band structures and PDOS. The band gap of a material, obtained from the band structure, is an important quantity that influences the efficiency of photovoltaic materials. It is the difference between the minimum of the conduction band and the maximum of the valence band. For easier calculation of the band gap, the top of the valence band was shifted to be the same as the Fermi energy and is shown by the dashed line in the plots in Figures 5.4(a-f). The  $k$ -paths used in the band structure calculations were unique to the structure of the material. For the cubic structures, the  $k$ -path followed was  $\Gamma - X - M - \Gamma - R - X | M - R$ . The  $k$ -path for the tetragonal structures was  $\Gamma - X - M - \Gamma - Z - R - A - Z | X - R | M - A$ . For the trigonal materials, the  $k$ -path followed was  $\Gamma - L - B_1B - Z - \Gamma - X | Q - F - P_1 - Z | L - P$ . From the band gap values, it was noted that these were increasing as the perovskite was distorting to lower symmetries, i.e., from cubic to tetragonal to trigonal. Focusing on the change in the X anion in all the structures, it was observed that as the anion changed from Cl to Br, the band gap

value decreased. This meant that as the mass of the X anion increased, the band gap was expected to decrease; the vice versa being true.

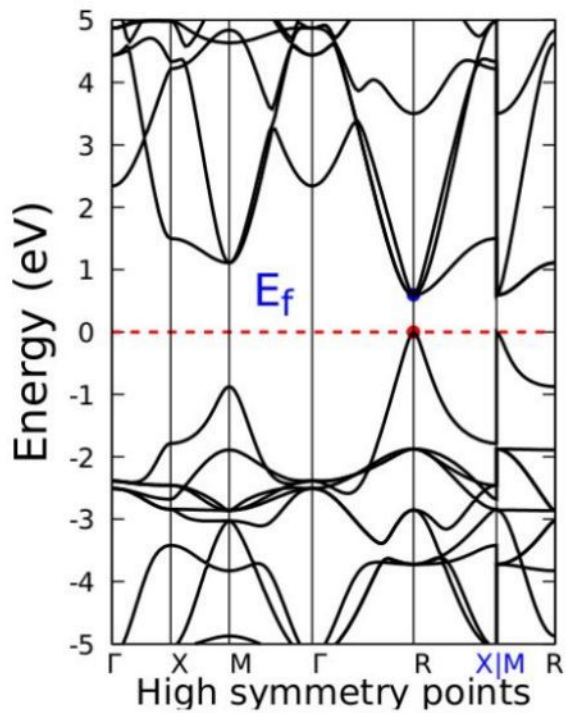
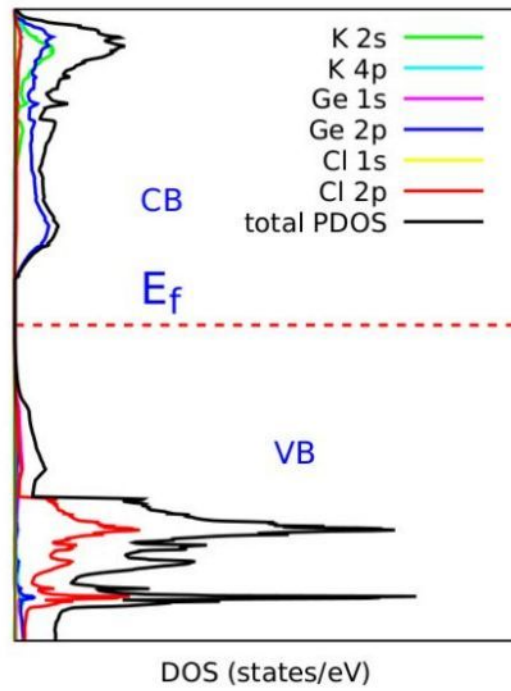
The materials showed semiconducting behaviors and have direct band gaps because the maximum of the valence band and the minimum of the conduction band are located at the same point of symmetry. The cubic perovskites have the valence band (VB) maximum and the conduction Band (CB) minimum located at the R. For the tetragonal structures, the CB and VB are located at the Z and the trigonal structures have the CB and VB located at Z and X|Q.

The band structures had discontinuities at points X|M for the cubic perovskites and points Z|X and R|M for the tetragonal perovskites. These discontinuities are indicated with blue fonts on the axes. The trigonal perovskite band structures had no visible discontinuities. The type of semiconductor can also be identified from the position of the Fermi energy in the band structure plots from Figures 5.4(a-f). For all the materials, since the Fermi energy is closer to the valence band than the conduction band, it indicates that they are *p*-type semiconductors (Alsaeedi, 2014). Although the band gap values were in agreement with previous DFT work, it should be noted that the values calculated from PBE-DFT are generally expected to underestimate the actual experimental values. Materials with band gaps in the range of 0.900-2.000 eV are the most efficient for solar energy absorption since this is the range that solar radiation reaches the earth's surface (Saikia *et al.*, 2022). These materials are therefore suitable in making photovoltaic absorber layers, tandem structures and single junction solar cells. The tetragonal and cubic structures are well in this 0.900-2.000eV range. For band gaps beyond 2.000 eV, that is, the trigonal structures, they are effective in making the window and buffer layers of the solar cells.

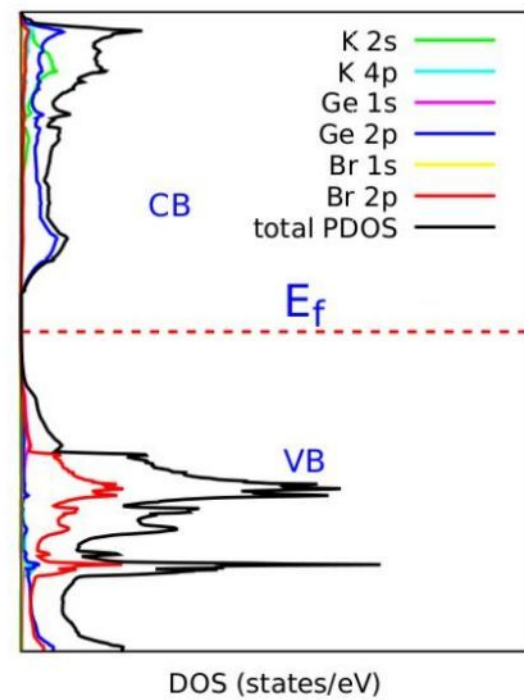
The PDOS is useful in investigating the detailed band structure of materials. It gives the properties of the electronic band structure in all the possible positions in the *k*-space. From the PDOS plots, it was noted that the conduction band was dominated by the p orbitals of germanium and the valence band mainly consists of the p orbitals of bromine and chlorine for KGeBr<sub>3</sub> and KGeCl<sub>3</sub>, respectively in the cubic structures. It can also be noted that the k orbitals do not contribute much to the total density of states.

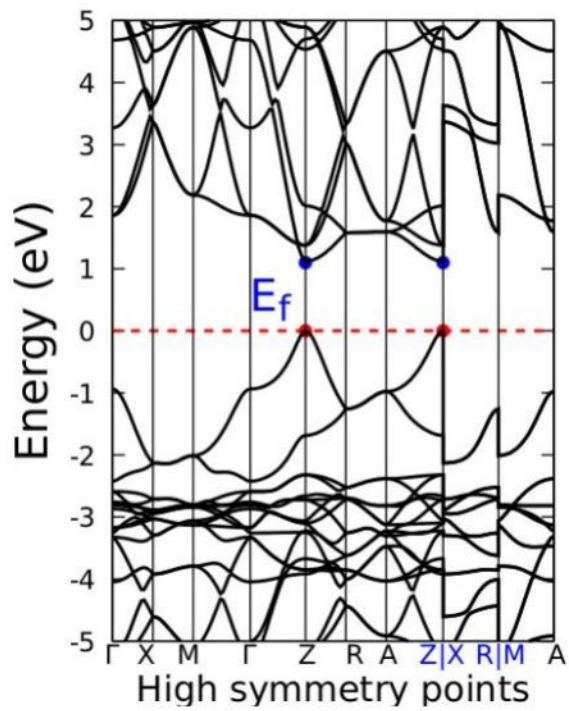


5.4 a  $KGeCl_3$  Cubic

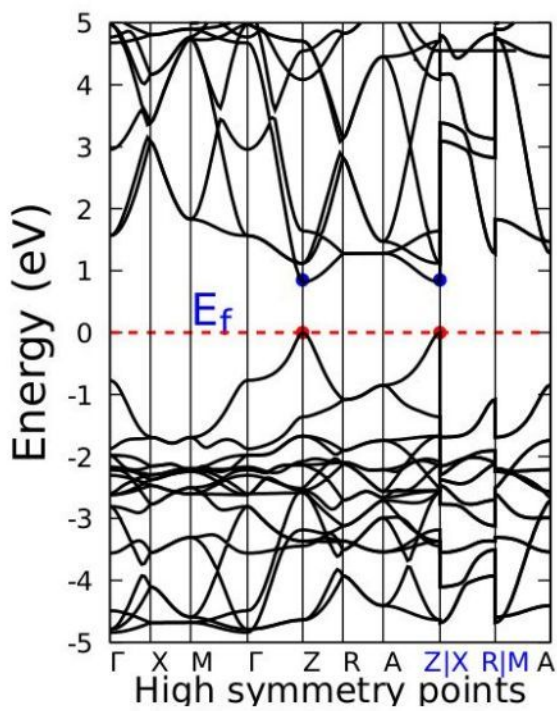
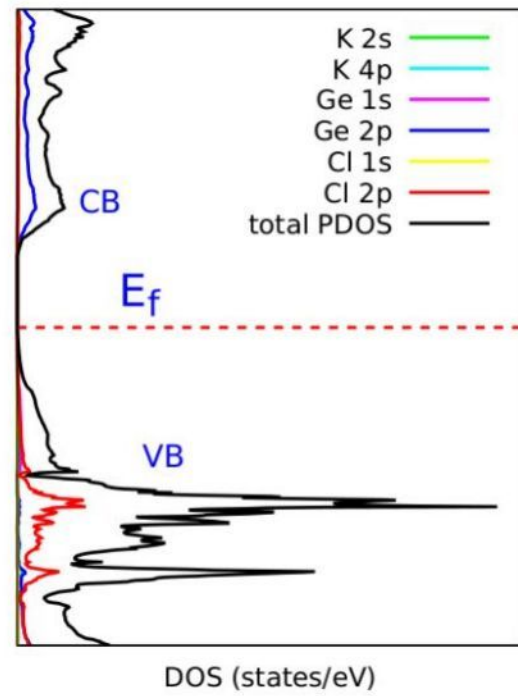


5.4 b  $KGeBr_3$  Cubic

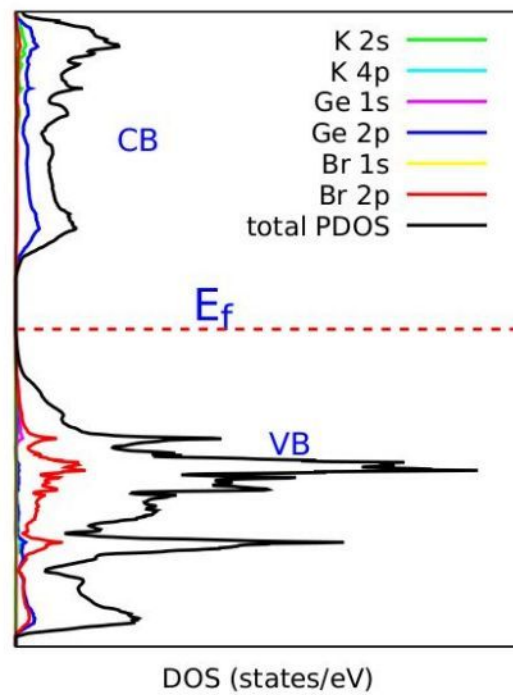




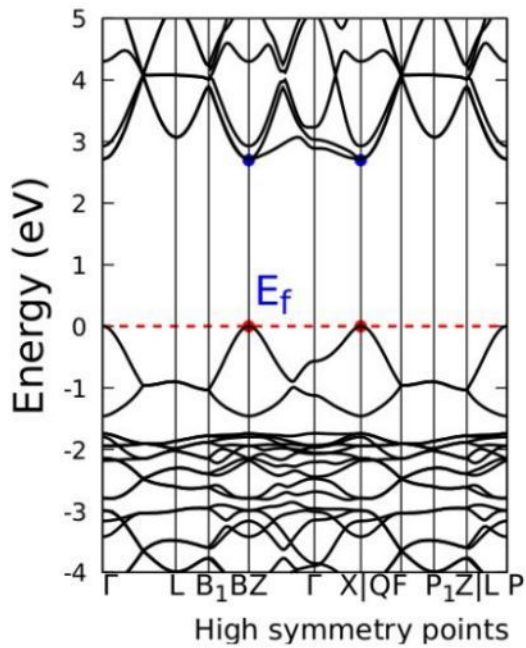
5.4 c  $KGeCl_3$  Tetragonal



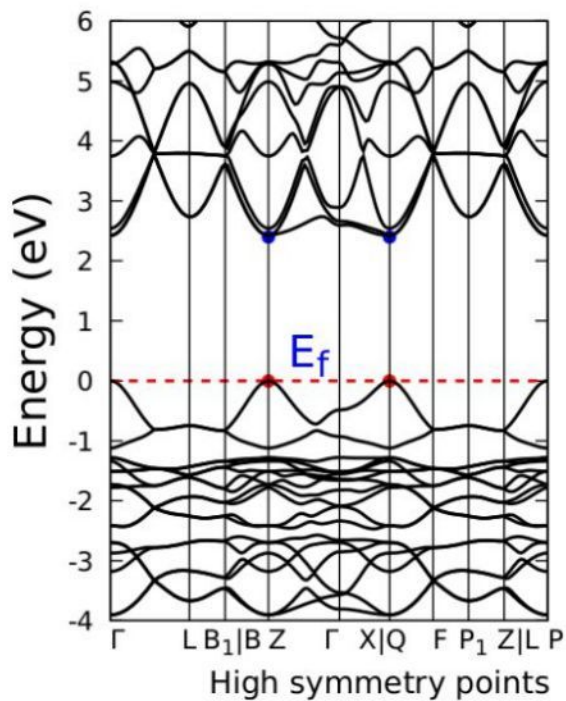
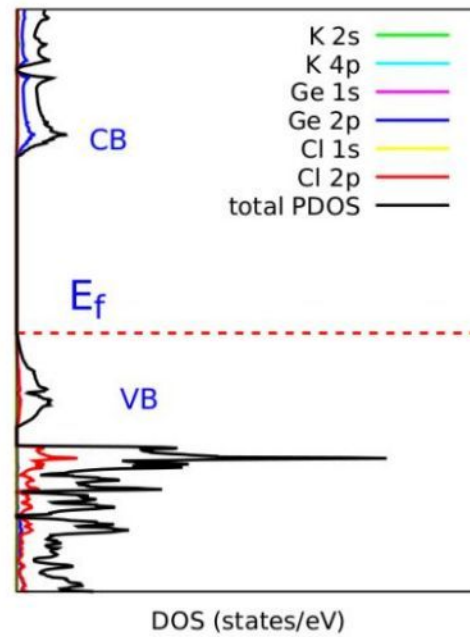
5.4 b  $KGeBr_3$  Tetragonal







5.4 c  $KGeCl_3$  Trigonal



5.4 d  $KGeBr_3$  Trigonal

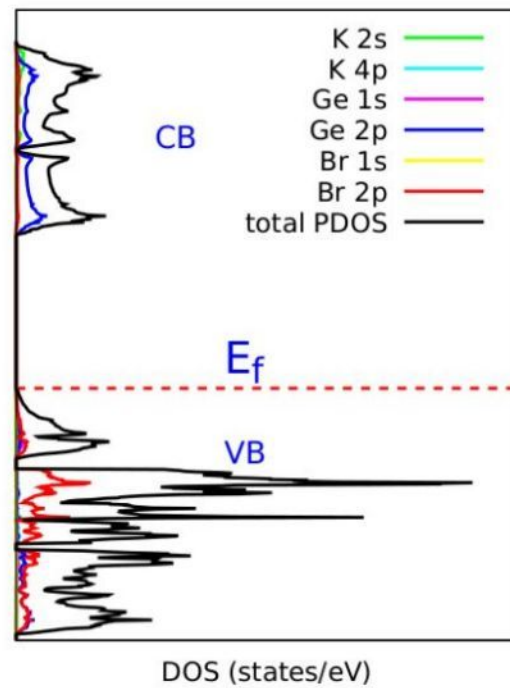


**Figure 5.4** Band structures and density of states of  $KGeX_3$  perovskites using DFT-(GGA-PBE) approximation. The Fermi energy level is shown by the horizontal red dashed line. VB maximum and CB minimum are shown by the red and blue circles, respectively and the discontinuity points are indicated on the axes with blue font.



From the band structure graphs, the band gaps were recorded and compared with literature in Table 5.8, and all were direct band gaps, and whose values are in close agreement with those reported in literature (Hamideddine *et al.*, (2022); Houari *et al.*, (2020); Saikia *et al.*, (2020). The GW approximation correction of the band gaps is also recorded in Table 5.8. The trigonal structures were found to have the largest band gaps for both materials. The cubic and tetragonal structures have band gaps of 0.800eV and 1.200eV for the KGeCl<sub>3</sub> and 0.700eV and 0.900eV for the KGeBr<sub>3</sub> materials, showing that they are in close agreement.

**Table 5.8:** The calculated band gaps in eV of the KGeX<sub>3</sub> materials using GGA-PBE and GW approximations compared to previous DFT reported work by (Hamideddine *et al.*, (2022); Houari *et al.*, (2020); Saikia *et al.*, (2020).

Material	Structure	Band gap (eV)		Band gap (eV) Previous work
		Our Work		
		GGA-PBE	GW	
KGeCl <sub>3</sub>	Cubic	0.800	1.100	0.900 <sup>a</sup> , 0.958 <sup>b</sup>
	Trigonal	2.700	2.900	---
	Tetragonal	1.200	1.900	---
KGeBr <sub>3</sub>	Cubic	0.700	1.040	0.610 <sup>a</sup> , 0.689 <sup>b</sup> , 0.910 <sup>c</sup>
	Trigonal	2.493	2.58	---
	Tetragonal	0.900	1.60	---

<sup>a</sup>(Houari *et al.*, 2020) <sup>b</sup>(Hamideddine *et al.*, 2022) <sup>c</sup>(Saikia *et al.*, 2022.)

### 5.5: Optical Characteristics

The real and imaginary parts of the dielectric constant were considered and the other optical properties such as the reflectivity, refractive index, energy loss, exciton index and absorption coefficient obtained from these. Figures (5.5) - (5.10) show these results. The minimum energy range calculated was between 0 – 20.000 eV. In terms of wavelength, this is approximately equal to 0 - 1242.000 nm. The relation between the energy and the wavelength is as in equation (5.1). The range of the visible spectrum is 400.000-700.000nm and in terms of energy approximately equals to 1.774 - 3.105eV.

$$\lambda = \frac{hc}{e} \quad (5.1)$$

In this case,  $h$  is the Planck's constant,  $c$  the speed of light and  $e$  is the energy. From Figure 5.5, of the real part of the dielectric constant against the energy in eV, the  $\epsilon_1(0)$ , called the electronic

part of the static dielectric function (Ghaithan *et al.*, 2020; Saikia *et al.*, 2022.) is 3.860, 4.380, 5.180, 6.320, 6.560 and 9.630 for  $\text{KGeCl}_3$  and  $\text{KGeBr}_3$  trigonal,  $\text{KGeCl}_3$  and  $\text{KGeBr}_3$  tetragonal and  $\text{KGeCl}_3$  and  $\text{KGeBr}_3$  cubic, respectively. From this, the electronic part of the dielectric function increases from trigonal - tetragonal - cubic, that is, as the material moves to the structurally ideal cubic perovskite. Furthermore, the  $\epsilon_1(0)$  increases with increase in the mass of the X element, that is, from chlorine to bromine. The static refractive index  $n(0)$  is the square root of the static dielectric function (Azam *et al.*, 2019) as shown by the relation in equation (5.2).

$$n(0) = \sqrt{\epsilon_1(0)} \quad (5.2)$$

From the same Figure 5.5, highest peaks were noticed at frequencies of 5.580, 6.460, 6.540, 8.400, 7.600 and 10.580 at 3.320eV, 2.890eV, 2.66eV, 2.190eV, 1.350eV and 0.480eV for  $\text{KGeCl}_3$  and  $\text{KGeBr}_3$  trigonal,  $\text{KGeBr}_3$  tetragonal and  $\text{KGeCl}_3$  and  $\text{KGeBr}_3$  cubic, respectively. The peaks are indicated with red circles.

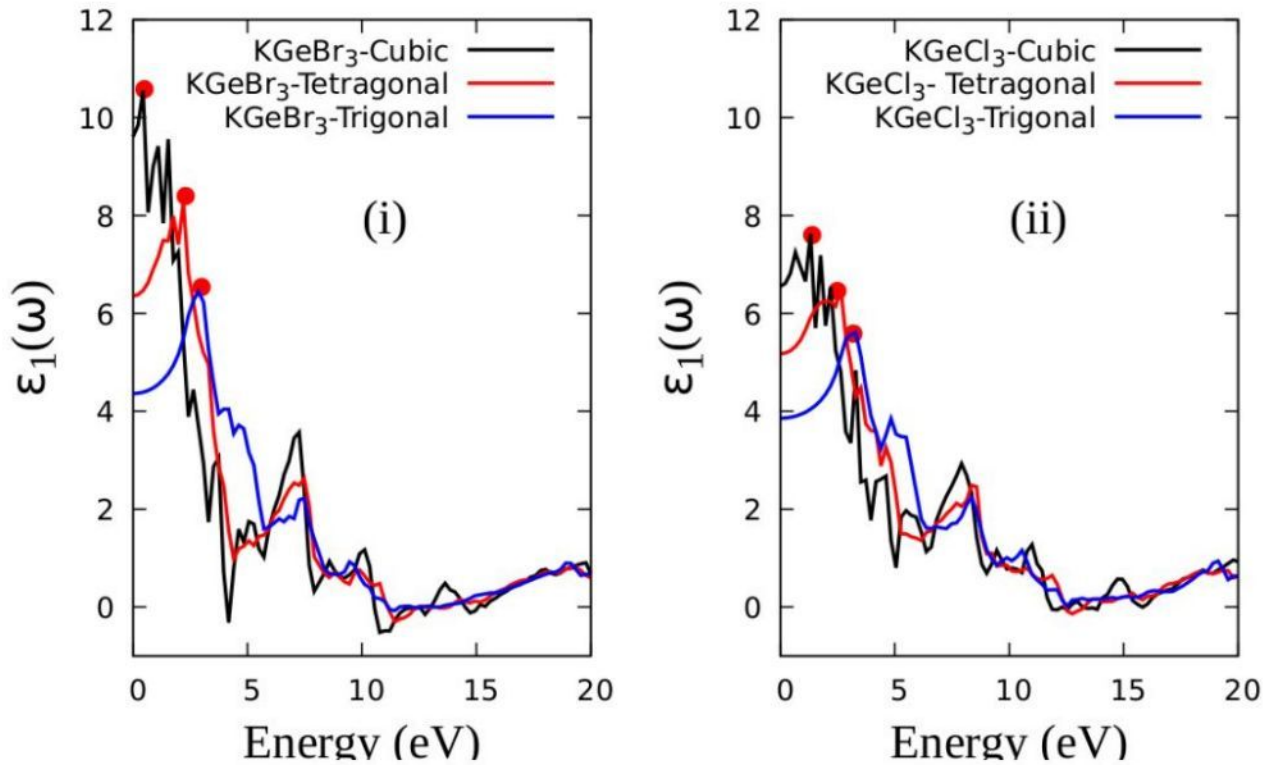


**Figure 5. 5** A graph of the real part of the dielectric function against the energy in eV for the (i)  $\text{KGeBr}_3$  and (ii)  $\text{KGeCl}_3$  cubic, tetragonal and trigonal perovskite materials.

The imaginary part spectra, from figure 5.6, is important because it relates to the band structure of materials (Benchehima *et al.*, 2018; Ghaithan *et al.*, 2020). The principal peaks of the imaginary part, which are the highest and most noticeable peaks, are located at 3.700, 4.120, 4.330, 5.870,

5.680 and 6.680 for  $\text{KGeCl}_3$  and  $\text{KGeBr}_3$  trigonal,  $\text{KGeCl}_3$  and  $\text{KGeBr}_3$  tetragonal and  $\text{KGeCl}_3$  and  $\text{KGeBr}_3$  cubic, respectively. These peaks are represented by the red circles in figure 5.6. The critical onset points are the regions in the graphs before the first peaks are observed. The critical onset points for the materials are at frequencies of 0.990, 2.748, 1.137, 0.951, 1.124 and 1.029 for  $\text{KGeCl}_3$  and  $\text{KGeBr}_3$  cubic, trigonal and tetragonal structures, respectively, represented by the green circles. These onset points are closely related to the calculated electronic band gaps of the materials recorded in table 5.8.

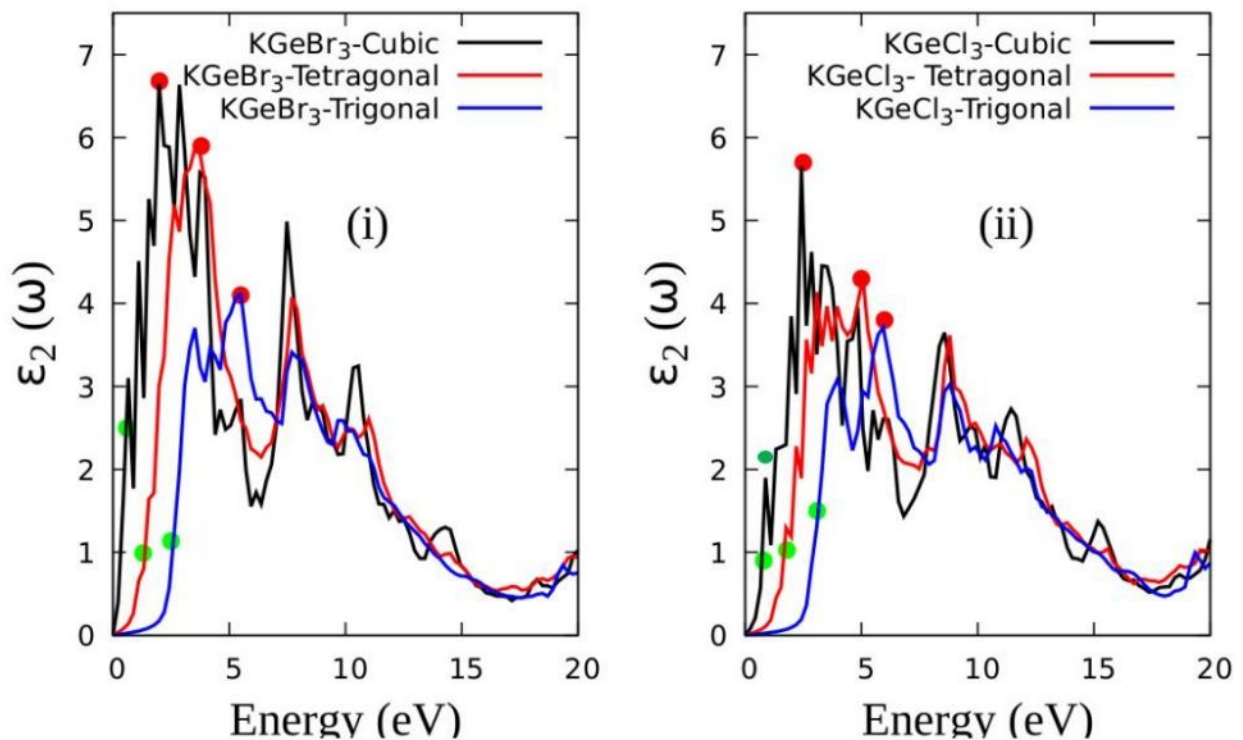


**Figure 5. 6** A graph of the imaginary part of the dielectric function against the energy in eV for the (i)  $\text{KGeBr}_3$  and (ii)  $\text{KGeCl}_3$  cubic, tetragonal and trigonal perovskite materials.

From figure 5.7 of the energy loss against the energy, it is noted that the energy is lost from the materials gradually from 0 – 5.000eV. At 15.000 – 20.000 eV, that is, in the UV spectrum the energy loss from the materials increases with the highest peaks showing in this region. In the visible region (1.774 – 3.105 eV), the energy loss is relatively low for all the materials. This is a good indication that the materials are good for photovoltaics since most of the energy will be retained and not lost to the environment.

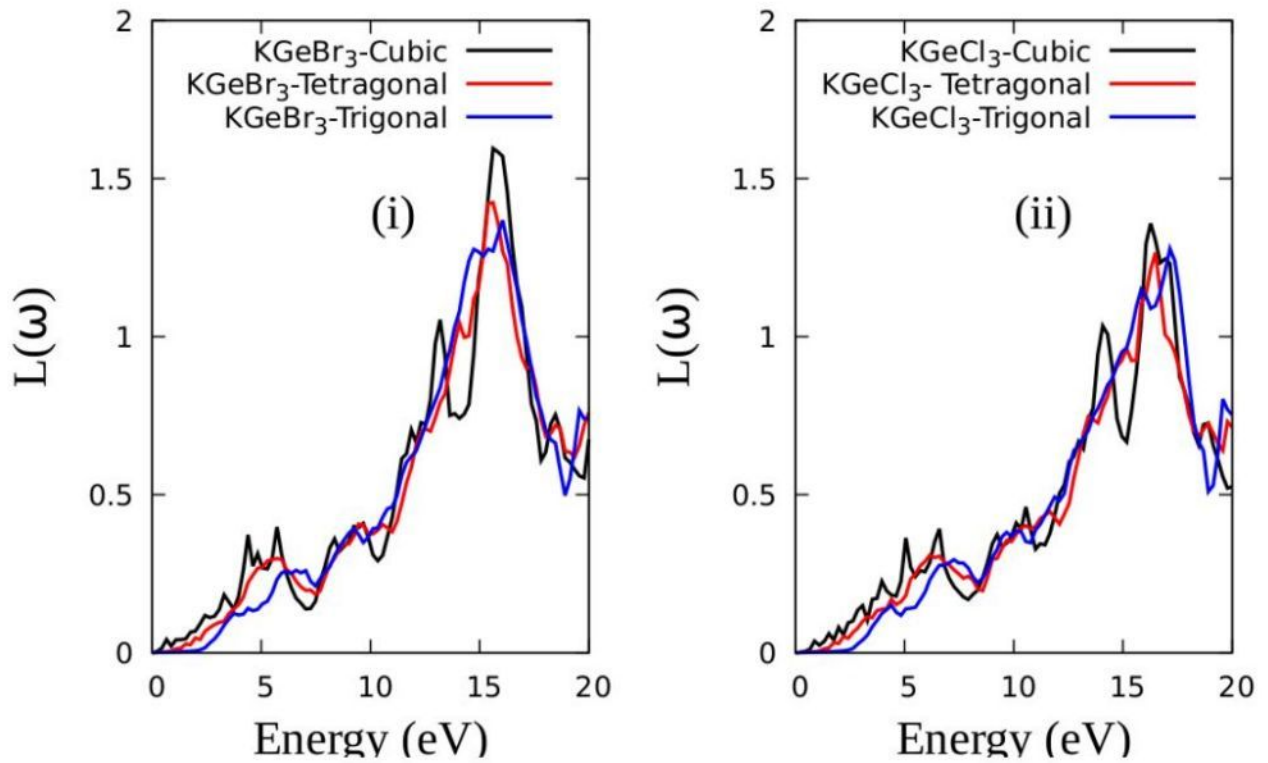


**Figure 5.7** A graph of the energy loss,  $L(\omega)$ , against the energy in eV for the (i)  $KGeBr_3$  and (ii)  $KGeCl_3$  cubic, tetragonal and trigonal perovskite materials.

In figure 5.8 of the absorption coefficients, it is observed that the highest peaks are in the range of 3.917 - 12.568 eV and the materials have broad absorption spectra in the range of 2.500eV - 16.000eV which is in the UV-Vis region of the electromagnetic spectra. This shows that  $KGeX_3$  materials in all the three phases are suitable for photovoltaics.



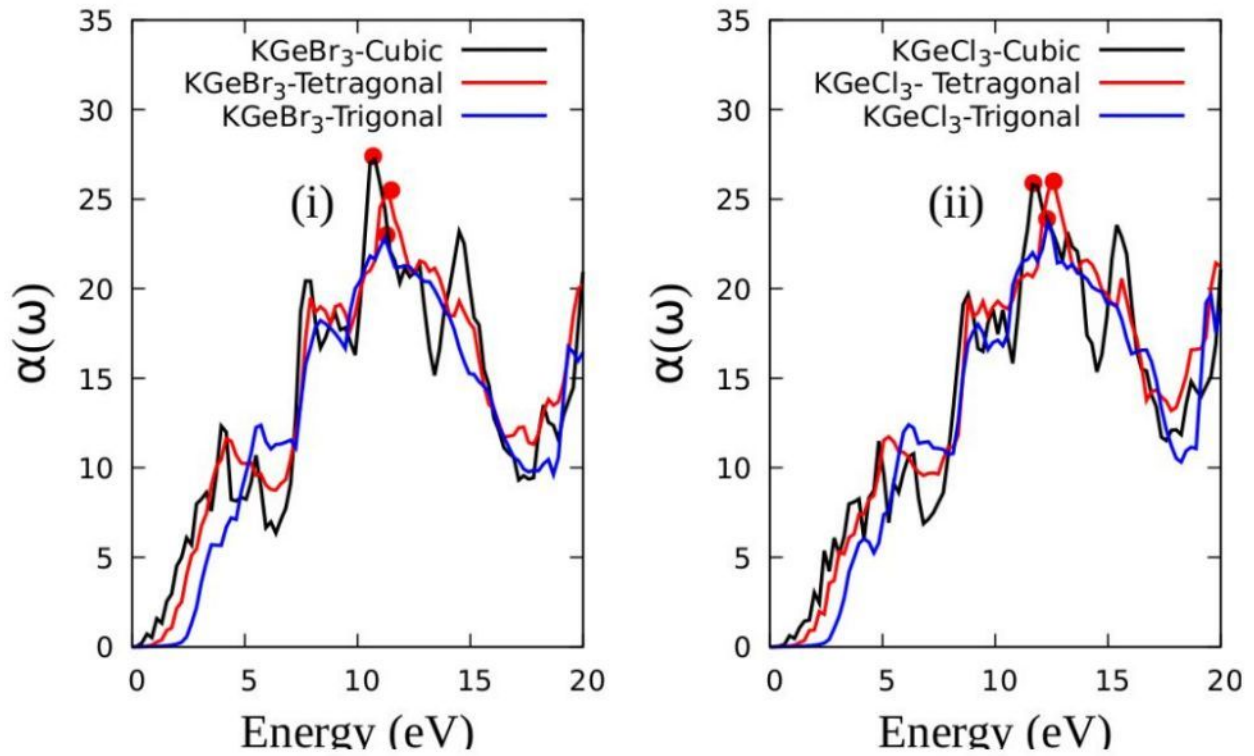


**Figure 5. 8** A graph of absorption coefficient against the energy in eV for the (i)  $KGeBr_3$  and (ii)  $KGeCl_3$  cubic, tetragonal and trigonal perovskite materials.

Figure 5.9 is a plot of the reflectivity against the energy, it shows that  $KGeBr_3$  cubic has the highest reflectivity in the visible region. For this material, reflectivity starts at the frequency of 0.262 at 0.000eV and gradually increases to the highest value of 0.298 located at 3.955eV. For the  $KGeBr_3$  tetragonal perovskite, reflectivity at 0.000eV is 0.186 after which it increases to reach the maximum reflectance value of 0.267 at 3.735eV. Its chloride counterpart,  $KGeCl_3$ , has the reflectivity value of 0.150 at 0.000eV and reaches the peak value of 0.234 at 2.669eV. For the  $KGeCl_3$  trigonal and (cubic) perovskites, reflectivity at 0.000eV is at 0.105 (0.194) and increases to the maximum value of 0.189 (0.262) located at 3.515eV (2.485eV). The maximum reflectivity of all the materials is in the visible region and is indicated on the graph by the red circles. Comparing the materials' rates of absorption in figure 5.8 with the reflectivity in figure 5.9, the reflectivity of the materials is comparatively lower indicating that the materials are good for photovoltaic applications. This is because the materials absorb more light than they reflect it.

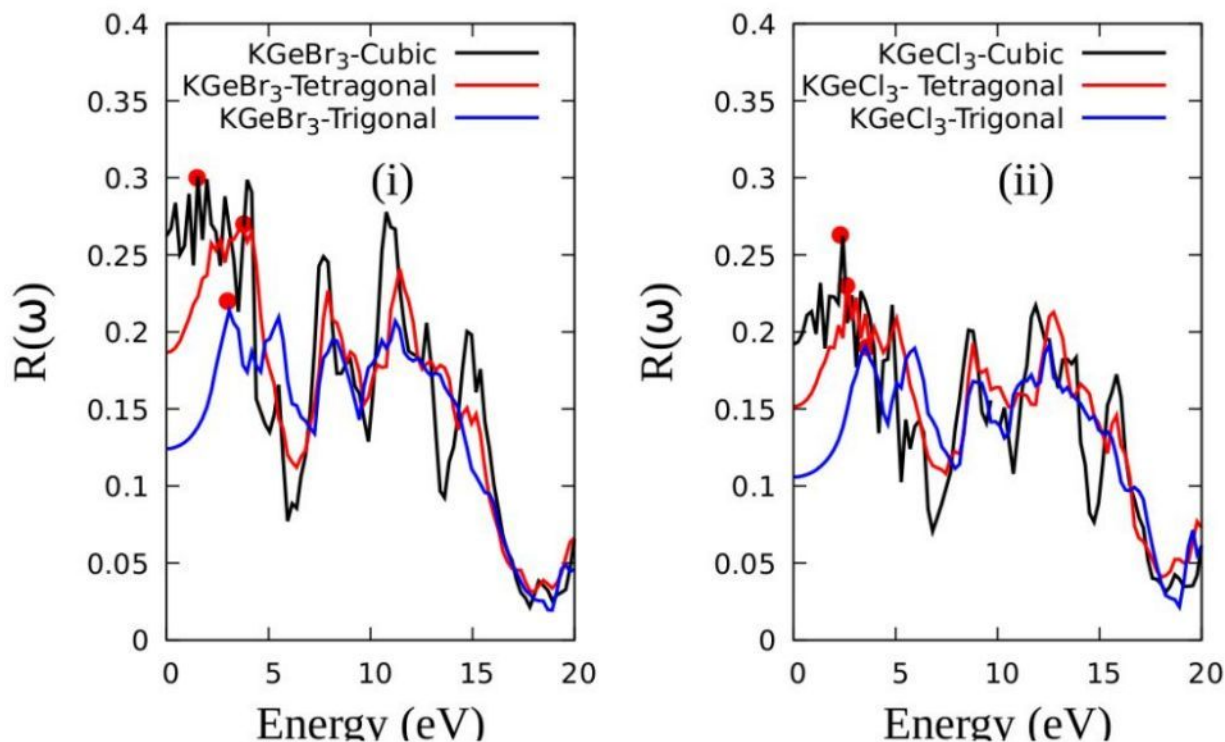


**Figure 5.9** A graph of the reflectivity,  $R(\omega)$ , against the energy in eV for the (i)  $KGeBr_3$  and (ii)  $KGeCl_3$  cubic, tetragonal and trigonal perovskite materials.

The refractive index indicates how much light is bent or refracted in a material. Figure 5.10 gives the refractive indices for the respective materials, the obtained refractive index values are given in Table 5.9. It is evident that the refractive index and the energy have an inverse relationship and that the refractive index is large in regions with small energies. For the absorption coefficient, however the case is opposite because the absorption is smaller in low energy values. The highest values of the refractive indices are located at 2.390, 2.570, 2.650, 2.910, 2.780 and 3.250 for  $KGeCl_3$  and  $KGeBr_3$  trigonal,  $KGeCl_3$  and  $KGeBr_3$  tetragonal and  $KGeCl_3$  and  $KGeBr_3$  cubic, respectively, indicated by the red filled circles. These correspond to the energy values of 3.180eV, 2.960eV, 2.670eV, 2.190eV, 1.350eV and 0.460eV for the respective materials. The tetragonal and trigonal structures have the maximum values of the refractive indices in the visible region. The cubic  $KGeCl_3$  and  $KGeBr_3$  however, have them located at the infrared and near infrared regions, respectively.  $KGeBr_3$  cubic has the highest refractive index of all the materials indicating that it is much denser and that light bends more as it moves through different media. The static refractive index,  $n(0)$ , is the refractive index at zero energy, that is, 0.000eV. For the materials, the static refractive indices are located at 1.958, 2.094, 2.266, 2.511, 2.560 and 3.113 for  $KGeCl_3$



and  $\text{KGeBr}_3$  trigonal,  $\text{KGeCl}_3$  and  $\text{KGeBr}_3$  tetragonal and  $\text{KGeCl}_3$  and  $\text{KGeBr}_3$  cubic, respectively, represented by the green circles. The static refractive index is higher for the bromide materials and relatively lower for the chloride materials. This index,  $n(0)$ , is also seen to increase from trigonal-tetragonal-cubic. The overall trend of the refractive index is similar to that of the real part of the dielectric constant from figure 5.6.

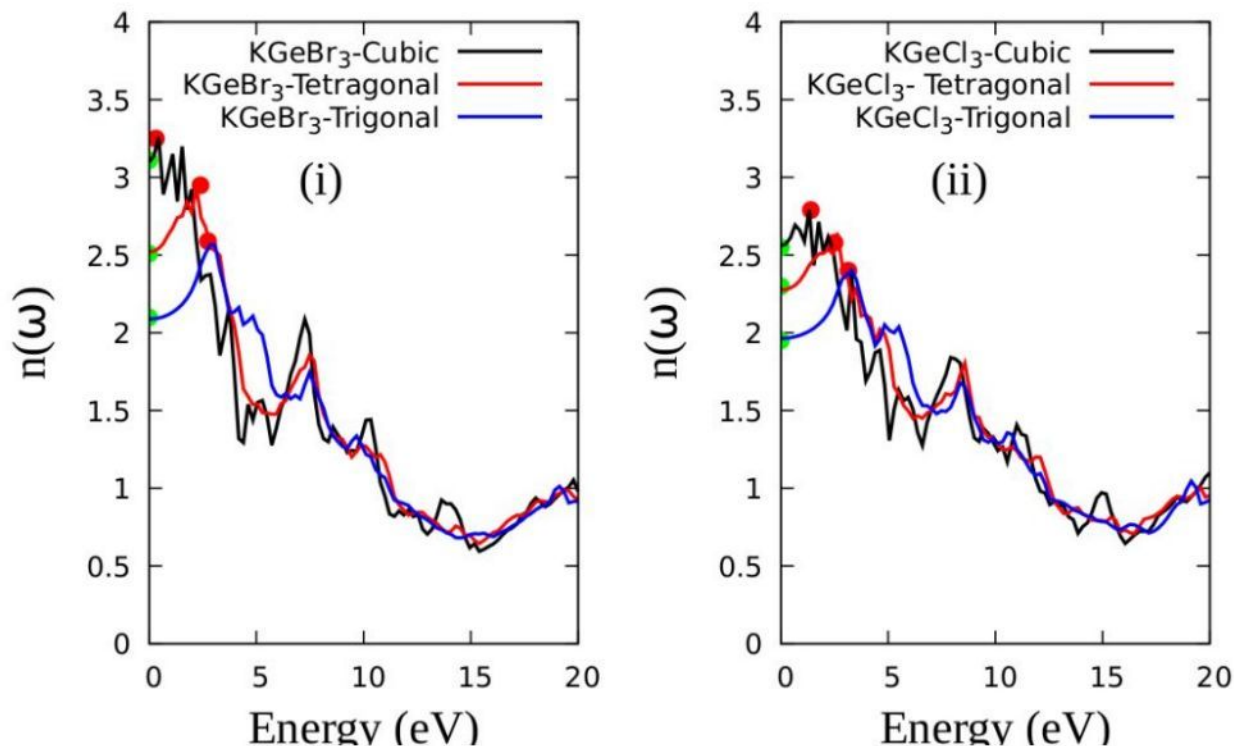


**Figure 5.10:** A graph of the refractive index,  $n(\omega)$ , against the energy in eV for the (i)  $\text{KGeBr}_3$  and (ii)  $\text{KGeCl}_3$  cubic, tetragonal and trigonal perovskite materials.

**Table 5.9:** The calculated DFT- (GGE-PBE) refractive indices of the  $\text{KGeX}_3$  materials

Material	$n(\omega)$
$\text{KGeCl}_3$ Trigonal	1.926
$\text{KGeCl}_3$ Cubic	2.585
$\text{KGeCl}_3$ Tetragonal	2.279
$\text{KGeBr}_3$ Cubic	3.092
$\text{KGeBr}_3$ Tetragonal	2.512
$\text{KGeBr}_3$ Trigonal	2.118

## 5.6: Theoretical Efficiency

The Shockley—Queisser limit gives the maximum theoretical efficiency of a solar cell. From the band gaps obtained from the electronic property calculations, Table 5.10 gives the theoretical efficiencies the perovskite  $\text{KGeX}_3$  ( $X=\text{Cl}, \text{Br}$ ) materials can have in a single p-n junction. It is observed that the tetragonal structures have the highest theoretical power conversion efficiencies followed closely by the cubic structures. As reported by Rühle, 2016; Shockley and Queisser, 1961, the maximum theoretical solar conversion efficiency that can be obtained by a solar cell is 33.7% when the band gap is at 1.400eV. The tetragonal structures are closely comparable to this maximum value and show promising results in photovoltaics.

**Table 5.10:** The maximum theoretical power-conversion efficiencies of the  $\text{KGeX}_3$  materials calculated from the Shockley-Queisser limit alongside their respective band gaps.

Material	Structure	Band gap (eV)	Theoretical efficiency (%)
$\text{KGeCl}_3$	Cubic	0.800	27.5
	Trigonal	2.700	9.3
	Tetragonal	1.200	32.5
$\text{KGeBr}_3$	Cubic	0.700	23.0
	Trigonal	2.493	12.9
	Tetragonal	0.900	30.0

## CHAPTER SIX: CONCLUSIONS AND RECOMMENDATIONS

### 6.1: Introduction

This chapter gives the conclusions drawn from the results, and recommendations for further work.

### 6.2: Conclusions

This work investigated the structural, elastic, electronic and optical properties of all-inorganic  $\text{KGeX}_3$  perovskites for use in photovoltaics. Three phases of the materials were investigated, that is, the cubic, tetragonal and trigonal phases. All the calculations were done in the Q.E code using the GGA-PBE approximations. All the calculations were well converged and for the cubic phases, the lattice constant and band gap values agreed with previous DFT work done. To the best of our knowledge, the tetragonal and trigonal  $\text{KGeX}_3$  perovskites have not been studied both experimentally and computationally hence could not be compared to previous work.

1. In the structural calculations and using the total energies of the materials, the study found out that the trigonal structures were the most energetically stable compared to the tetragonal and cubic structures because they had comparatively lower energies of -349.705 Ry and -320.846 Ry for the chloride and bromide perovskites, respectively. Noticing that the cubic structures had the highest energy, it was concluded that as the symmetry of the perovskite lowered, the energy decreased to more stable structures. The chloride perovskites for all the three phases had lower energies than their bromide counterparts showing that the energies increased as the X atoms were replaced with elements with a high mass number. The tolerance factor for the trigonal and tetragonal structures were unequal to unity showing that the two structures were truly distorted. From the tolerance factors, it was found out that for the tetragonal structures, the cause of the distortion was through an octahedra shift with the octahedra tilting inwards. However, for the trigonal structures, the K cation was too big in relation to the octahedra making the octahedra to bulge outwards causing the distortion.
2. From the elastic properties, the calculated elastic constants were employed in the Born stability criteria which classified the trigonal structures as mechanically unstable. Furthermore, the chloride trigonal structure was brittle ruling it out for photovoltaics since the perovskite films for photovoltaics would crack easily. The brittleness was checked using the Pugh's ratio, Cauchy pressure and the Poisson's ratio. All the three methods identified the trigonal structures

as brittle. The calculation of the anisotropic factors showed that all the materials were anisotropic structures save for the trigonal perovskites which are isotropic in the  $\{001\}$  planes since  $A_3 = 1$

3. In the electronic calculations, it was found that the tetragonal structures had the most suitable band gaps for use in photovoltaics, that is, 1.200 eV and 0.900 eV for the chloride and bromide perovskite, respectively. All the materials had direct band gaps with the maximum of the VB and minimum of the CB located at R and Z points of the x- axis for the cubic and tetragonal structures and the Z and X|Q of the trigonal structures, respectively.
4. From the calculation of the maximum theoretical efficiency from the detailed balance limit, also known as the Shockley -Queisser limit, the tetragonal structures have theoretical power-conversion efficiencies of 32.5% and 30% for the chloride and bromide perovskites, respectively. This phase was found to have the highest efficiencies which were closely comparable to the maximum attainable theoretical efficiency of 33.7%. The trigonal structures, because of their wide band gaps, had the lowest theoretical efficiencies. From this calculation, it was then concluded that the tetragonal structures would make the best materials for optoelectronic and photovoltaic applications.
5. For photovoltaic applications, the tetragonal structured materials appear to be more consistent according to the properties investigated in this study. The trigonal structure, though being energetically stable, had very large band gaps, that is, 2.700 eV and 2.493 eV for the chloride and bromide structures, respectively, which are not suitable for photovoltaics. Additionally, they were found to be mechanically unstable and brittle.

### **6.3: Recommendations**

Studying the electronic, elastic, optical and structural properties is important in determining if a material can be considered for photovoltaic and other applications.

1. For photovoltaics, we highly recommend the tetragonal structures because they have shown consistently good properties from the structural, electronic, mechanical and optical property calculations and the theoretical efficiencies. The trigonal structures would be

least recommended.

2. For the band gap calculation, the GGA-PBE exchange correlational functional used in this work is known to underestimate the band gap. Work still needs to be done using different approaches like the  $\Delta$ -sol and other hybrid exchange correlation approximations for more accurate band gap precisions.
3. It is also recommended for future work to employ full potential linearized augmented plane wave plus the local orbital (FP-LAPW+Lo) method.
4. For structures like the trigonal phase where the band gap was found to be way high for photovoltaics, we recommend band gap engineering studies to be done to tune the band gaps for photovoltaics.
5. In comparison with the cubic structures, the distorted tetragonal perovskites proved to be more stable and better suited for photovoltaics. Therefore, there is still the need to investigate the other lower symmetry perovskites like the monoclinic, orthorhombic and trigonal  $R3m$  in the quest for more stable and better suitable photovoltaic materials.
6. We also recommend that other stoichiometries of  $KGeX_3$  perovskite be studied with inclusion of the double, triple and mixed halide perovskites.
7. Other than photovoltaics, we recommend that these materials be studied for other applications as well.



## REFERENCES

- Akihiro, K., Kenjiro, T., Yasuo, S., and Tsutomu, M. (2009). Organometal halide perovskites as visible-light sensitizers for photovoltaic cells. *Journal of the American Chemical Society*, **131**(17), 6050–6051. <https://doi.org/https://doi.org/10.1021/ja809598r>
- Alers, G. A., and Neighbours, J. R. (1957). Crystal stability and elastic constants. *Journal of Applied Physics* **28**(12). <https://doi.org/10.1063/1.1722692>
- Allan, L., Amolo, G. O., Mwabora, J., and Mureramanzi, S. (2022). The Impact of Nitrogen Doping on Structural and Electronic Properties of Titanium Sesquioxide, Ti<sub>2</sub>O<sub>3</sub>: An ab-initio Study. <http://arxiv.org/abs/2201.00212>
- Alsaeedi, A. (2014). Synthesis of thin film solar cell based on CZT(S, Se) <https://doi.org/10.13140/RG.2.2.13501.41443>
- Amin, B., Ahmad, I., Maqbool, M., Goumri-Said, S., and Ahmad, R. (2011). *ab initio* study of the bandgap engineering of Al<sub>1-x</sub>Ga<sub>x</sub>N for optoelectronic applications. *Journal of Applied Physics*, **109**(2). <https://doi.org/10.1063/1.3531996>
- Anderson, M. T., Greenwood, K. B., Taylor, G. A., and Poepelmeiert, K. R. (1993). B-cation arrangements in double perovskites. *Progress in solid state. Chemistry* **22**, 197-233.
- Assirey, E. A. R. (2019). Perovskite synthesis, properties and their related biochemical and industrial application. *Saudi Pharmaceutical Journal*, **27**(6), 817–829. <https://doi.org/10.1016/j.jsps.2019.05.003>
- Azam, S., Irfan, M., Abbas, Z., Rani, M., Saleem, T., Younus, A., Akhtar, N., Liaqat, B., Shabbir, M., and Al-Sehemi, A. G. (2019). DFT study of the electronic and optical properties of ternary chalcogenides AlX<sub>2</sub>Te<sub>4</sub>. *Materials Research Express*, **6**(11). <https://doi.org/10.1088/2053-1591/ab4b81>
- Badawy, W. A. (2015). A review on solar cells from Si-single crystals to porous materials and Quantum dots. In *Journal of Advanced Research* **6**(2), pp. 123–132). Elsevier <https://doi.org/10.1016/j.jare.2013.10.001>
- Ben Mahmoud, C., Anelli, A., Csanyi, G., and Ceriotti, M. (2020). Learning the electronic density of states in condensed matter. *Physical Review B*, **102**(23). <https://doi.org/10.1103/PhysRevB.102.235130>
- Benchehima, M., Abid, H., Sadoun, A., and Chabane Chaouche, A. (2018). Optoelectronic properties of aluminum bismuth antimony ternary alloys for optical telecommunication applications: First principles calculation. *Computational Materials Science*, **155**, 224–234. <https://doi.org/10.1016/j.commatsci.2018.08.050>



- Burger, S., Ehrenreich, M. G., and Kieslich, G. (2018). Tolerance factors of hybrid organic-inorganic perovskites: recent improvements and current state of research. *Journal of Materials Chemistry A* **6**(44), 21785–21793. <https://doi.org/10.1039/C8TA05794J>
- Butt, M. K., Yaseen, M., Iqbal, J., Altowyan, A. S., Murtaza, A., Iqbal, M., and Laref, A. (2021). Structural, electronic, half –metallic ferromagnetic and optical properties of cubic MA<sub>1</sub>O<sub>3</sub> (M=Ce, Pr) perovskites: A DFT study. *Journal of Physics and Chemistry of Solids*, 154. <https://doi.org/10.1016/j.jpcs.2021.110084>
- Capelle, K. (2006). A bird's-eye view of density-functional theory. *Brazilian Journal of Physics*, **36**(4A), 1318–1341. <https://doi.org/10.1590/s0103-97332006000700035>
- Chapin, D. M., Fuller, C. S., and Pearson, G. L. (1954). A new silicon p-n junction photocell for converting solar radiation into electrical power [3]. *Journal of Applied Physics* **25**(5), 676–677). <https://doi.org/10.1063/1.1721711>
- Cheng, P., Wu, T., Liu, J., Deng, W. Q., and Han, K. (2018). Lead-Free, Two-Dimensional Mixed Germanium and Tin Perovskites, *Journal of Physical Chemistry Letters*, **9**(10), 2518–2522. <https://doi.org/10.1021/acs.jpcclett.8b00871>
- Ciucivara, A. (2007). Density functional studies of magnetic semiconductors and multiferroics. <https://www.researchgate.net/publication/37256837>
- De, M. (2020). Lead-Free Perovskite Nanocomposites: An Aspect for Environmental Application. *Perovskite and Piezoelectric Materials*. <https://doi.org/10.5772/INTECHOPEN.93052>
- Dong, H., Chen, C., Wang, S., Duan, W., and Li, J. (2013). Elastic properties of tetragonal BiFeO<sub>3</sub> from first-principles calculations. *Applied Physics Letters*, **102**(18). <https://doi.org/10.1063/1.4804641>
- Enkovaara, J., Rostgaard, C., and Mortensen, J. J. (2017). Advanced capabilities for materials modelling with Quantum ESPRESSO, *Journal of Physics: Condensed Matter*, **29**.
- Epstein, S. T., and Rosenthal, C. M. (1976). The Hohenberg-Kohn theorem. *Journal of Chemical Physics*, **64**(1), 247–249. <https://doi.org/10.1063/1.431969>
- Faheem, M. B., Khan, B., Feng, C., Farooq, M. U., Raziq, F., Xiao, Y., and Li, Y. (2020). All-Inorganic Perovskite Solar Cells: Energetics, Key Challenges, and Strategies toward Commercialization. *ACS Energy Letters*, **5**(1), 290–320. <https://doi.org/10.1021/acsenergylett.9b02338>
- Filip, M. R., and Giustino, F. (2016). Computational Screening of Homovalent Lead Substitution in Organic-Inorganic Halide Perovskites. *Journal of Physical Chemistry C*, **120**(1), 166–173. <https://doi.org/10.1021/acs.jpcc.5b11845>

- Gaa, I. E., Hohenberg, P., Superzewe, I., Aris, X., And, F., and Konnt, W. (1964)., Inhomogeneous electron gas, *Physical review*
- Ghaithan, H. M., Alahmed, Z. A., Qaid, S. M. H., Hezam, M., and Aldwayyan, A. S. (2020). Density Functional Study of Cubic, Tetragonal, and Orthorhombic CsPbBr<sub>3</sub> Perovskite. *ACS Omega*, *5*(13), 7468–7480. <https://doi.org/10.1021/acsomega.0c00197>
- Giannozzi, P., Baroni, S., Bonini, N., Calandra, M., Car, R., Cavazzoni, C., Ceresoli, D., Chiarotti, G. L., Cococcioni, M., Dabo, I., Dal Corso, A., de Gironcoli, S., Fabris, S., Fratesi, G., Gebauer, R., Gerstmann, U., Gougoussis, C., Kokalj, A., Lazzeri, M., Wentzcovitch, R. M. (2009). Quantum ESPRESSO: A modular and open-source software project for quantum simulations of materials. *Journal of Physics Condensed Matter*, *21*(39). <https://doi.org/10.1088/0953-8984/21/39/395502>
- Giannozzi, P., Baseggio, O., Bonfà, P., Brunato, D., Car, R., Carnimeo, I., Cavazzoni, C., de Gironcoli, S., Delugas, P., Ferrari Ruffino, F., Ferretti, A., Marzari, N., Timrov, I., Urru, A., and Baroni, S. (2020). Quantum ESPRESSO toward the exascale. *Journal of Chemical Physics*, *152*(15). <https://doi.org/10.1063/5.0005082>
- Giustino, F., and Snaith, H. J. (2016). Toward Lead-Free Perovskite Solar Cells. *ACS Energy Letters* *1*(6), 1233–1240. <https://doi.org/10.1021/acseenergylett.6b00499>
- Glazer, A. M. (1975). Simple ways of determining perovskite structures. *Acta Crystallographica Section A*, *31*(6), 756–762. <https://doi.org/10.1107/S0567739475001635>
- Green, M. A. (2002). Third generation photovoltaics: solar cells for 2020 and beyond. In *Physica E* **14**. [www.elsevier.com/locate/physce](http://www.elsevier.com/locate/physce)
- Hamideddine, I., Tahiri, N., Bounagui, O. El, and Ez-Zahraouy, H. (2022). *ab initio* study of structural and optical properties of the halide perovskite KBX<sub>3</sub> compound. *Journal of the Korean Ceramic Society*. <https://doi.org/10.1007/s43207-021-00178-6>
- Hamideddine, I., Tahiri, N., el Bounagui, O., and Ez-Zahraouy, H. (2020). Theoretical investigation of electronic and optical properties of the CuIn<sub>1-x</sub>Ga<sub>x</sub>Se<sub>2</sub>: *Ab initio* calculation. *Optik*, *207*. <https://doi.org/10.1016/j.ijleo.2019.163881>
- Harrison, N. M. (2005). *An Introduction to Density Functional Theory*.
- Hicks, D., Mehl, M. J., Esters, M., Oses, C., Levy, O., Hart, G. L. W., Toher, C., and Curtarolo, S. (2021). The AFLOW Library of Crystallographic Prototypes: Part 3. *Computational Materials Science*, *199*, 110450. <https://doi.org/10.1016/J.COMMATSCI.2021.110450>
- Hicks, D., Mehl, M. J., Gossett, E., Toher, C., Levy, O., Hanson, R. M., Hart, G., and Curtarolo, S. (2019). The AFLOW Library of Crystallographic Prototypes: Part 2. *Computational Materials Science*, *161*, S1–S1011. <https://doi.org/10.1016/J.COMMATSCI.2018.10.043>



- Hill, R. (1932), The elastic behavior of crystalline aggregate. *Proceedings of the physical society*, A **65**(349)
- Hinuma, Y., Pizzi, G., Kumagai, Y., Oba, F., and Tanaka, I. (2017). Band structure diagram paths based on crystallography. *Computational Materials Science*, **128**, 140–184. <https://doi.org/10.1016/J.COMMATSCI.2016.10.015>
- Hou, Z. F. (2008). *Ab initio* calculations of elastic modulus and electronic structures of cubic  $\text{CaZrO}_3$ . *Physica B: Condensed Matter*, **403**(17), 2624–2628. <https://doi.org/10.1016/j.physb.2008.01.025>
- Houari, M., Bouadjemi, B., Haid, S., Matougui, M., Lantri, T., Aziz, Z., Bentata, S., and Bouhafs, B. (2020). Semiconductor behavior of halide perovskites  $\text{AGeX}_3$  (A = K, Rb and Cs; X = F, Cl and Br): first-principles calculations. *Indian Journal of Physics*, **94**(4), 455–467. <https://doi.org/10.1007/s12648-019-01480-0>
- Houari, M., Bouadjemi, B., Matougui, M., Haid, S., Lantri, T., Aziz, Z., Bentata, S., and Bouhafs, B. (2019). Optoelectronic properties of germanium iodide perovskites  $\text{AGeI}_3$  (A = K, Rb and Cs): first principles investigations. *Optical and Quantum Electronics*, **51**(7). <https://doi.org/10.1007/s11082-019-1949-y>
- Howard, C. J., and Stokes, H. T. (2005). Structures and phase transitions in perovskites - A group-theoretical approach. In *Acta Crystallographica Section A: Foundations of Crystallography* **61**(1), 93–111. <https://doi.org/10.1107/S0108767304024493>
- Hung, N. T., Nugraha, A. R. T., and Saito, R. (2018). First Principles Workshop An introduction and hands-on tutorial with the Quantum ESPRESSO Quantum Espresso Hands-on Tutorial. <http://flex.phys.tohoku.ac.jp>
- Idrissi, S., Labrim, H., Bahmad, L., and Benyoussef, A. (2021). DFT and TDDFT studies of the new inorganic perovskite  $\text{CsPbI}_3$  for solar cell applications. *Chemical Physics Letters*, **766**(January), 138347. <https://doi.org/10.1016/j.cplett.2021.138347>
- Idrissi, S., Ziti, S., Labrim, H., and Bahmad, L. (2021). Band gaps of the solar perovskites photovoltaic  $\text{CsXCl}_3$  (X=Sn, Pb or Ge). *Materials Science in Semiconductor Processing*, **122**. <https://doi.org/10.1016/j.mssp.2020.105484>
- Igbari, F., Wang, Z. K., and Liao, L. S. (2019). Progress of Lead-Free Halide Double Perovskites. *Advanced Energy Materials* **9**(12). Wiley-VCH Verlag. <https://doi.org/10.1002/aenm.201803150>
- Charles, K. (2005) *Introduction to Solid State Physics*, John Wiley and Sons Inc., 11-126
- Jain, A., Ong, S. P., Hautier, G., Chen, W., Richards, W. D., Dacek, S., Cholia, S., Gunter, D., Skinner, D., Ceder, G., and Persson, K. A. (2013). Commentary: The Materials Project: A

- materials genome approach to accelerating materials innovation. *APL Materials*, **1**(1), 011002. <https://doi.org/10.1063/1.4812323>
- Ju, M. G., Dai, J., Ma, L., and Zeng, X. C. (2017). Lead-Free Mixed Tin and Germanium Perovskites for Photovoltaic Application. *Journal of the American Chemical Society*, **139**(23), 8038–8043. <https://doi.org/10.1021/jacs.7b04219>
- Khatibi, A., Razi Astaraei, F., and Ahmadi, M. H. (2019). Generation and combination of the solar cells: A current model review. In *Energy Science and Engineering* **7**(2) pp. 305–322). John Wiley and Sons Ltd. <https://doi.org/10.1002/ese3.292>
- Kohn, W., and Sham, L. J. (1965). Self-consistent equations including exchange and correlation effects. *Physical Review*, **140**(4A), A1133. <https://doi.org/10.1103/PHYSREV.140.A1133/FIGURE/1/THUMB>
- Kopacic, I., Friesenbichler, B., Hoefler, S. F., Kunert, B., Plank, H., Rath, T., and Trimmel, G. (2018). Enhanced Performance of Germanium Halide Perovskite Solar Cells through Compositional Engineering. *ACS Applied Energy Materials*, **1**(2), 343–347. <https://doi.org/10.1021/acsaem.8b00007>
- Körbel, S., Marques, M. A. L., and Botti, S. (2016). Stability and electronic properties of new inorganic perovskites from high throughput: *Ab initio* calculations. *Journal of Materials Chemistry C*, **4**(15), 3157–3167. <https://doi.org/10.1039/c5tc04172d>
- Krishnamoorthy, T., Ding, H., Yan, C., Leong, W. L., Baikie, T., Zhang, Z., Sherburne, M., Li, S., Asta, M., Mathews, N., and Mhaisalkar, S. G. (2015). Lead-free germanium iodide perovskite materials for photovoltaic applications. *Journal of Materials Chemistry A*, **3**(47), 23829–23832. <https://doi.org/10.1039/c5ta05741h>
- Kuma, S., and Woldemariam, M. M. (2019). Structural, Electronic, Lattice Dynamic, and Elastic Properties of SnTiO<sub>3</sub> and PbTiO<sub>3</sub> Using Density Functional Theory. *Advances in Condensed Matter Physics*, 2019. <https://doi.org/10.1155/2019/3176148>
- Kumar, M., Umezawa, N., and Imai, M. (2014). (SrBa)(SiGe)<sub>2</sub> for thin-film solar-cell applications: First-principles study. *Journal of Applied Physics*, **115**(20). <https://doi.org/10.1063/1.4880662>
- Li, S., Li, S., and Ju, X. (2017). Elastic properties of cubic K<sub>2</sub>B<sub>12</sub>H<sub>12</sub> from theoretical calculations. *Journal of Alloys and Compounds*, **695**, 2916–2922. <https://doi.org/10.1016/j.jallcom.2016.11.385>
- Liu, J., Xue, Y., Wang, Z., Xu, Z. Q., Zheng, C., Weber, B., Song, J., Wang, Y., Lu, Y., Zhang, Y., and Bao, Q. (2016). Two-Dimensional CH<sub>3</sub>NH<sub>3</sub>PbI<sub>3</sub> Perovskite: Synthesis and Optoelectronic Application. *ACS Nano*, **10**(3), 3536–3542. <https://doi.org/10.1021/acsnano.5b07791>



- Liu, Q. J., Qin, H., Jiao, Z., Liu, F. S., and Liu, Z. T. (2016). First-principles calculations of structural, elastic, and electronic properties of trigonal  $\text{ZnSnO}_3$  under pressure. *Materials Chemistry and Physics*, *180*, 75–81. <https://doi.org/10.1016/j.matchemphys.2016.05.041>
- Liu, X., Yang, Z., Chueh, C. C., Rajagopal, A., Williams, S. T., Sun, Y., and Jen, A. K. Y. (2016). Improved efficiency and stability of Pb-Sn binary perovskite solar cells by Cs substitution. *Journal of Materials Chemistry A*, *4*(46), 17939–17945. <https://doi.org/10.1039/c6ta07712a>
- Liu, Y., Nag, A., Manna, L., and Xia, Z. (2021). Lead-Free Double Perovskite  $\text{Cs}_2\text{AgInCl}_6$ . In *Angewandte Chemie - International Edition* **60**(21) 11592–11603. John Wiley and Sons Inc. <https://doi.org/10.1002/anie.202011833>
- Lufaso, M. W., and Woodward, P. M. (2001). Structural Science Prediction of the crystal structures of perovskites using the software program SPuDS. *Acta Cryst*, *57*, 725–738.
- Luo, T., Xia, Y., Huang, J., Huang, X., Wu, Z., Chen, Y., Xu, X., Xie, W., Liu, P., Hu, C., Lu, X., and Shi, T. (2021). Different structural evolutions of inorganic perovskite  $\text{CsGeI}_3$ . *CrystEngComm*, *23*(28), 4917–4922. <https://doi.org/10.1039/d1ce00364j>
- Ma, Q., Huang, S., Chen, S., Zhang, M., Lau, C. F. J., Lockrey, M. N., Mulmudi, H. K., Shan, Y., Yao, J., Zheng, J., Deng, X., Catchpole, K., Green, M. A., and Ho-Baillie, A. W. Y. (2017). The Effect of Stoichiometry on the Stability of Inorganic Cesium Lead Mixed-Halide Perovskites Solar Cells. *Journal of Physical Chemistry C*, *121*(36), 19642–19649. <https://doi.org/10.1021/acs.jpcc.7b06268>
- Malakkal, L., Szpunar, B., Zuniga, J. C., Siripurapu, R. K., and Szpunar, J. A. (2015). An interface to Quantum ESPRESSO. *Proceedings of the 3rd World Congress on Integrated Computational Materials Engineering, ICME 2015, Icme*, 155–162. <https://doi.org/10.1002/9781119139508.ch19>
- Malakkal, L., Szpunar, B., Zuniga, J. C., Siripurapu, R. K., and Szpunar, J. A. (2016). First principles calculation of thermo-mechanical properties of thorium using Quantum ESPRESSO. *International Journal of Computational Materials Science and Engineering*, *5*(2), 1–15. <https://doi.org/10.1142/S2047684116500081>
- Mao, X., Sun, L., Wu, T., Chu, T., Deng, W., and Han, K. (2018). First-Principles Screening of All-Inorganic Lead-Free  $\text{ABX}_3$  Perovskites. *Journal of Physical Chemistry C*, *122*(14), 7670–7675. <https://doi.org/10.1021/acs.jpcc.8b02448>
- Marr, J. M., and Wilkin, F. P. (2012). A better presentation of Planck's radiation law. *American Journal of Physics*, *80*(5), 399–405. <https://doi.org/10.1119/1.3696974>
- Mbilo, M., Manyali, G. S., and Musembi, R. J. (2022). *Ab initio* study of  $\text{K}_3\text{Cu}_3\text{P}_2$  material for photovoltaic applications. *Computational Condensed Matter*, *32*, e00726. <https://doi.org/10.1016/j.cocom.2022.e00726>

- Mehl, M. J., Hicks, D., Toher, C., Levy, O., Hanson, R. M., Hart, G., and Curtarolo, S. (2017). The AFLOW Library of Crystallographic Prototypes: Part 1. *Computational Materials Science*, 136, S1–S828. <https://doi.org/10.1016/J.COMMATSCI.2017.01.017>
- Mohamed Mansour, E. (2020). Equation of State. In *Inverse Heat Conduction and Heat Exchangers*. IntechOpen. <https://doi.org/10.5772/intechopen.89919>
- Momma, K., and Izumi, F. (2011). VESTA 3 for three-dimensional visualization of crystal, volumetric and morphology data. *Journal of Applied Crystallography*, 44(6), 1272–1276. <https://doi.org/10.1107/S0021889811038970/FULL>
- Monkhorst, H. J., and Pack, J. D. (1976). Special points for Brillouin-zone integrations. In *NUMBER 13*.
- Mouhat, F., and Coudert, F. X. (2014). Necessary and sufficient elastic stability conditions in various crystal systems. *Physical Review B - Condensed Matter and Materials Physics*, 90(22). <https://doi.org/10.1103/PhysRevB.90.224104>
- Mulwa, W. M., Ouma, C. N. M., Onani, M. O., and Dejene, F. B. (2016). Energetic, electronic and optical properties of lanthanide doped TiO<sub>2</sub>: An *ab initio* LDA+U study. *Journal of Solid State Chemistry*, 237, 129–137. <https://doi.org/10.1016/j.jssc.2016.02.003>
- Nishat, S. S., Hossain, M. J., Mullick, F. E., Kabir, A., Chowdhury, S., Islam, S., and Hossain, M. (2021). Performance Analysis of Perovskite Solar Cells Using DFT-Extracted Parameters of Metal-Doped TiO<sub>2</sub> Electron Transport Layer. *Journal of Physical Chemistry C*, 125(24), 13158–13166. <https://doi.org/10.1021/acs.jpcc.1c02302>
- Ouedraogo, N. A. N., Chen, Y., Xiao, Y. Y., Meng, Q., Han, C. B., Yan, H., and Zhang, Y. (2020). Stability of all-inorganic perovskite solar cells. *Nano Energy*, 67, 104249. <https://doi.org/10.1016/j.nanoen.2019.104249>
- Park, B. wook, and Seok, S. Il. (2019). Intrinsic Instability of Inorganic–Organic Hybrid Halide Perovskite Materials. *Advanced Materials*, 31(20), 1–17. <https://doi.org/10.1002/adma.201805337>
- Perdew, J. P., Burke, K., and Ernzerhof, M. (1996). Generalized Gradient Approximation Made Simple.
- Planck's Radiation law*. (2012).
- Pugh, S. F. (1954). Relations between the elastic moduli and the plastic properties of polycrystalline pure metals. *The London, Edinburgh, and Dublin Philosophical Magazine and Journal of Science*, 45(367), 823–843. <https://doi.org/10.1080/14786440808520496>



- Råsander, M. (2010). *A Theoretical Perspective on the Chemical Bonding and Structure of Transition Metal Carbides and Multilayers*.  
<https://www.researchgate.net/publication/241685137>
- Reuss, A. (1929). Berechnung der Fließgrenze von Mischkristallen auf Grund der Plastizitätsbedingung für Einkristalle. *ZAMM - Journal of Applied Mathematics and Mechanics / Zeitschrift Für Angewandte Mathematik Und Mechanik*, **9**(1), 49–58.  
<https://doi.org/10.1002/ZAMM.19290090104>
- Risch, M. (2017). Perovskite Electrocatalysts for the Oxygen Reduction Reaction in Alkaline Media. *Catalysts* **7**(5), 154. <https://doi.org/10.3390/CATAL7050154>
- Roknuzzaman, M., Ostrikov, K. K., Wang, H., Du, A., and Tesfamichael, T. (2017). Towards lead-free perovskite photovoltaics and optoelectronics by ab-initio simulations. *Scientific Reports*, **7**(1), 1–8. <https://doi.org/10.1038/s41598-017-13172-y>
- Roknuzzaman, M., Ostrikov, K. (Ken), Chandula Wasalathilake, K., Yan, C., Wang, H., and Tesfamichael, T. (2018). Insight into lead-free organic-inorganic hybrid perovskites for photovoltaics and optoelectronics: A first-principles study. *Organic Electronics*, **59**, 99–106. <https://doi.org/10.1016/j.orgel.2018.04.051>
- Romero, J., Phillips, E., Ruetsch, G., Fatica, M., Spiga, F., and Giannozzi, P. (2018). A performance study of quantum ESPRESSO's PWscf Code on multi-core and GPU Systems. *Lecture Notes in Computer Science (Including Subseries Lecture Notes in Artificial Intelligence and Lecture Notes in Bioinformatics)*, **10724 LNCS**, 67–87.  
[https://doi.org/10.1007/978-3-319-72971-8\\_4](https://doi.org/10.1007/978-3-319-72971-8_4)
- Rühle, S. (2016). Tabulated values of the Shockley-Queisser limit for single junction solar cells. *Solar Energy*, **130**, 139–147. <https://doi.org/10.1016/j.solener.2016.02.015>
- Saikia, D., Alam, M., Bera, J., Betal, A., Gandhi, A. N., and Sahu, S. (2020). *A First-principles study on  $ABBr_3$  ( $A = Cs, Rb, K, Na$ ;  $B = Ge, Sn$ ) halide perovskites for photovoltaic applications*.
- Saliba, M., Matsui, T., Seo, J. Y., Domanski, K., Correa-Baena, J. P., Nazeeruddin, M. K., Zakeeruddin, S. M., Tress, W., Abate, A., Hagfeldt, A., and Grätzel, M. (2016). Cesium-containing triple cation perovskite solar cells: Improved stability, reproducibility and high efficiency. *Energy and Environmental Science*, **9**(6), 1989–1997.  
<https://doi.org/10.1039/c5ee03874j>
- Scandolo, S., Giannozzi, P. I., Cavazzoni, C. I., de Gironcoli, S. I., Pasquarello, A. V., and Baroni, S. I. (2005). First-principles codes for computational crystallography in the Quantum-ESPRESSO package Ab-initio calculations / Molecular dynamics / Phonons / Elastic constants / High-pressure / Quantum-ESPRESSO Computer program / *Computational crystallography*. **220**, 574–579.

- Schrödinger, E. (1926). An undulatory theory of the mechanics of atoms and molecules. *Physical Review*, **28**(6), 1049–1070. <https://doi.org/10.1103/PhysRev.28.1049>
- Setyawan, W., and Curtarolo, S. (2010). High-throughput electronic band structure calculations: Challenges and tools. *Computational Materials Science*, **49**(2), 299–312. <https://doi.org/10.1016/j.commatsci.2010.05.010>
- Sharma, S., Jain, K. K., and Sharma, A. (2015). Solar Cells: In Research and Applications—A Review. *Materials Sciences and Applications*, **06**(12), 1145–1155. <https://doi.org/10.4236/msa.2015.612113>
- Shockley, W., and Queisser, H. J. (1961). Detailed balance limit of efficiency of p-n junction solar cells. *Journal of Applied Physics*, **32**(3), 510–519. <https://doi.org/10.1063/1.1736034>
- Sholl, D. S., and Steckel, J. A. (2009). *Density Functional Theory, A Practical Introduction*. John Wiley and Sons Inc.
- Singh, N., Agarwal, A., and Agarwal, M. (2021). Performance evaluation of lead-free double-perovskite solar cell. *Optical Materials*, **114**. <https://doi.org/10.1016/j.optmat.2021.110964>
- Singh, P. K., and Dwivedi, A. (2012). Pressure derivatives of bulk modulus for materials at extreme compression. *Indian Journal of Pure and Applied Physics* **50**.
- Sundaram, S., Shanks, K., and Upadhyaya, H. (2018). 18 - Thin Film Photovoltaics. In *A Comprehensive Guide to Solar Energy Systems*: Elsevier Inc. <https://doi.org/10.1016/B978-0-12-811479-7/00018-X>
- Takenaka, T., Nagata, H., Hiruma, Y., Yoshii, Y., and Matumoto, K. (2007). Lead-free piezoelectric ceramics based on perovskite structures. *Journal of Electroceramics*, **19**(4), 259–265. <https://doi.org/10.1007/s10832-007-9035-4>
- Talirz, L., Kumbhar, S., Passaro, E., Yakutovich, A. v., Granata, V., Gargiulo, F., Borelli, M., Uhrin, M., Huber, S. P., Zoupanos, S., Adorf, C. S., Andersen, C. W., Schütt, O., Pignedoli, C. A., Passerone, D., VandeVondele, J., Schulthess, T. C., Smit, B., Pizzi, G., and Marzari, N. (2020). Materials Cloud, a platform for open computational science. *Scientific Data*, **7**(1), 1–12. <https://doi.org/10.1038/s41597-020-00637-5>
- Tang, H., He, S., and Peng, C. (2017). A Short Progress Report on High-Efficiency Perovskite Solar Cells. *Nanoscale Research Letters*, **12**. <https://doi.org/10.1186/s11671-017-2187-5>
- Thakur, K. P. (1982). Theoretical strength of a perfect nickel crystal under simple stresses. *Journal of Applied Physics*, **53**(12), 8722–8729. <https://doi.org/10.1063/1.330471>



- Tian, J. H., Song, T., Sun, X. W., Wang, T., and Jiang, G. (2017). First-Principles Study on the Half-Metallic Ferromagnetism and Optical Properties of Fe-Doped CdSe and Co-Doped CdSe. *Journal of Superconductivity and Novel Magnetism*, **30**(2), 521–528. <https://doi.org/10.1007/s10948-016-3691-z>
- Tilley, R. J. D. (2016). *Perovskites Structure-Property Relationships*. [www.wiley.com](http://www.wiley.com).
- Togo, A., and Tanaka, I. (2018). *Spglib: a software library for crystal symmetry search*.
- Toulouse, J. (2019). *Introduction to density-functional theory*. 1–58.
- Tyuterev, V. G., and Vast, N. (2006). Murnaghan's equation of state for the electronic ground state energy. *Computational Materials Science*, **38**(2), 350–353. <https://doi.org/10.1016/j.commatsci.2005.08.012>
- Wan, X., Zhang, Z., Yu, W., and Guo, Y. (2021). A density-functional-theory-based and machine-learning-accelerated hybrid method for intricate system catalysis. *Materials Reports: Energy*, **1**(3), 100046. <https://doi.org/10.1016/j.matre.2021.100046>
- Wang, R., Mujahid, M., Duan, Y., Wang, Z. K., Xue, J., and Yang, Y. (2019). A Review of Perovskites Solar Cell Stability. *Advanced Functional Materials*, **29**(47), 1–25. <https://doi.org/10.1002/adfm.201808843>
- Wei, K., Faraj, Y., Yao, G., Xie, R., and Lai, B. (2021). Strategies for improving perovskite photocatalysts reactivity for organic pollutants degradation: A review on recent progress. *Chemical Engineering Journal* **414**. Elsevier B.V. <https://doi.org/10.1016/j.cej.2021.128783>
- Wu, T., and Gao, P. (2018). Development of perovskite-type materials for thermoelectric application. *Materials*, **11**(6), 1–32. <https://doi.org/10.3390/ma11060999>
- Yang, D., Zhang, G., Lai, R., Cheng, Y., Lian, Y., Rao, M., Huo, D., Lan, D., Zhao, B., and Di, D. (2021). Germanium-lead perovskite light-emitting diodes. *Nature Communications*, **12**(1). <https://doi.org/10.1038/s41467-021-24616-5>
- Yang, S., Fu, W., Zhang, Z., Chen, H., and Li, C. Z. (2017). Recent advances in perovskite solar cells: Efficiency, stability and lead-free perovskite. *Journal of Materials Chemistry A*, **5**(23), 11462–11482. <https://doi.org/10.1039/c7ta00366h>
- Yuan, Y., and Tang, A. (2020). Progress on the controllable synthesis of all-inorganic halide perovskite nanocrystals and their optoelectronic applications. *Journal of Semiconductors* **41**(1). IOP Publishing Ltd. <https://doi.org/10.1088/1674-4926/41/1/011201>
- Zerfass, L. (2015). The ABCs of DFT. *Flexo*, **40**(2), 22–24.
- Zhang, L., Miao, J., Li, J., and Li, Q. (2020). Halide Perovskite Materials for Energy Storage

Applications. *Advanced Functional Materials* **30**(40).  
<https://doi.org/10.1002/adfm.202003653>

## APPENDICES

### APPENDIX A: Pseudopotential files

Four pseudopotential files were used in this calculation, that is, for potassium, germanium, chlorine and bromine. They are as shown below.

#### *A1: Potassium pseudopotential file- K.pbe-spn-rrjkus\_psl.1.0.0.UPF*

<UPF version="2.0.1">

<PP\_INFO>

Generated using "atomic" code by A. Dal Corso v.6.2.2

Author: ADC

Generation date: 4May2018

Pseudopotential type: USPP

Element: K

Functional: PBE

Suggested minimum cutoff for wave functions: 41. Ry

Suggested minimum cutoff for charge density: 277. Ry

The Pseudo was generated with a Scalar-Relativistic Calculation

Local Potential by smoothing AE potential with Bessel fncs, cutoff radius: 1.5000

Pseudopotential contains additional information for GIPAW reconstruction.

Valence configuration:

nl pn l occ Rcut Rcut US E pseu

3S 1 0 2.00 1.200 1.300 -2.597645

4S 2 0 1.00 1.200 1.300 -0.170438

3P 2 1 6.00 1.400 1.600 -1.382750

4P 3 1 0.00 1.400 1.600 -0.059132

Generation configuration:

3S 1 0 2.00 1.200 1.300 -2.597649

4S 2 0 1.00 1.200 1.300 -0.170441

3P 2 1 6.00 1.400 1.600 -1.382755

4P 3 1 0.00 1.400 1.600 -0.059133

3D 3 2 0.00 1.200 1.700 0.050000

3D 3 2 0.00 1.200 1.700 1.000000

Pseudization used: troullier-martins

***A2: Germanium pseudopotential file- Ge.pbe-n-rrjkus\_psl.1.0.0.UPF***

<UPF version="2.0.1">

<PP\_INFO>

Generated using "atomic" code by A. Dal Corso v.6.3

Author: ADC

Generation date: 4Sep2018

Pseudopotential type: USPP

Element: Ge

Functional: PBE

Suggested minimum cutoff for wave functions: 20. Ry

Suggested minimum cutoff for charge density: 116. Ry

The Pseudo was generated with a Scalar-Relativistic Calculation

L component and cutoff radius for Local Potential: 2 2.2000

Pseudopotential contains additional information for GIPAW reconstruction.

Valence configuration:

nl pn l occ Rcut Rcut US E pseu

4S 1 0 2.00 1.500 1.700 -0.862224

4P 2 1 2.00 1.500 2.000 -0.286299

Generation configuration:

4S 1 0 2.00 1.500 1.700 -0.862222

4S 1 0 0.00 1.500 1.700 0.300000

4P 2 1 2.00 1.500 2.000 -0.286298

4P 2 1 0.00 1.500 2.000 0.300000

4D 3 2 -2.00 2.200 2.200 0.500000

Pseudization used: troullier-martins

***A3: Chlorine pseudopotential file- Cl.pbe-n-rrjkus\_psl.1.0.0.UPF***



<UPF version="2.0.1">

<PP\_INFO>

Generated using "atomic" code by A. Dal Corso v.6.3

Author: ADC

Generation date: 4Sep2018

Pseudopotential type: USPP

Element: Cl

Functional: PBE

Suggested minimum cutoff for wave functions: 45. Ry

Suggested minimum cutoff for charge density: 223. Ry

The Pseudo was generated with a Scalar-Relativistic Calculation

Local Potential by smoothing AE potential with Bessel fncs, cutoff radius: 1.8000

Pseudopotential contains additional information for GIPAW reconstruction.

Valence configuration:

nl pn l occ Rcut Rcut US E pseu

3S 1 0 2.00 1.200 1.600 -1.520835

3P 2 1 5.00 1.300 1.600 -0.631741

Generation configuration:

3S 1 0 2.00 1.200 1.600 -1.520832

3S 1 0 0.00 1.200 1.600 6.200000

3P 2 1 5.00 1.300 1.600 -0.631738

3P 2 1 0.00 1.300 1.600 3.200000

3D 3 2 0.00 1.300 1.600 0.100000

3D 3 2 0.00 1.300 1.600 0.300000

Pseudization used: troullier-martins

#### ***A4: Bromine pseudopotential file- Br.pbe-n-rrjkus\_psl.1.0.0.UPF***

<UPF version="2.0.1">

<PP\_INFO>

Generated using "atomic" code by A. Dal Corso v.6.3

Author: ADC

Generation date: 4Sep2018

Pseudopotential type: USPP

Element: Br

Functional: PBE

Suggested minimum cutoff for wave functions: 49. Ry

Suggested minimum cutoff for charge density: 196. Ry

The Pseudo was generated with a Scalar-Relativistic Calculation

L component and cutoff radius for Local Potential: 2 1.7000

Pseudopotential contains additional information for GIPAW reconstruction.

Valence configuration:

nl pn l occ Rcut Rcut US E pseu

4S 1 0 2.00 1.200 1.500 -1.479845

4P 2 1 5.00 1.400 1.700 -0.577675

Generation configuration:

4S 1 0 2.00 1.200 1.500 -1.479837

4S 1 0 0.00 1.200 1.500 6.300000

4P 2 1 5.00 1.400 1.700 -0.577671

4P 2 1 0.00 1.400 1.700 6.300000

4D 3 2 -2.00 1.700 1.700 0.500000

Pseudization used: troullier-martins

## **APPENDIX B: Sample input file**

The input files contain all the information needed for the first principle calculations.

### ***B1: Sample input file for cubic structure (KGeCl<sub>3</sub>)***

```
&Control  
calculation = 'scf'  
restart_mode='from_scratch',  
prefix='KGeCl3',  
pseudo_dir='/mnt/lustre/users/mnamisi/pseudo',  
outdir= './tempdir',  
tprnfor =. true.,
```

```

tstress=. true.
/
&System
ibrav= 1,
celldm (1) =9.95687,
nat= 5,
ntyp= 3
ecutwfc = 100.0,
ecutrho = 800.0,
occupations='smearing',
smearing='m-v',
degauss=0.0146997236,
/
&Electrons
mixing_mode = 'plain'
mixing_beta = 0.3
conv_thr = 1.0d-6
mixing_fixed_ns = 0
/
ATOMIC_SPECIES
Cl 35.453 Cl.pbe-n-rrkjus_psl.1.0.0.UPF
Ge 72.64 Ge.pbe-n-rrkjus_psl.1.0.0.UPF
K 39.0983 K.pbe-spn-rrkjus_psl.1.0.0.UPF
ATOMIC_POSITIONS (crystal)
K 0.000000000 0.000000000 0.000000000
Ge 0.500000000 0.500000000 0.500000000
Cl 0.500000000 0.000000000 0.500000000
Cl 0.500000000 0.500000000 0.000000000
Cl 0.000000000 0.500000000 0.500000000
K_POINTS {automatic}
8 8 8 0 0 0

```

## APPENDIX C: Murnaghan Equation of states

The Murnaghan equation of states was used to obtain the volumes, bulk moduli and its first derivative. Figures 6.1 (a-f) show the results obtained.

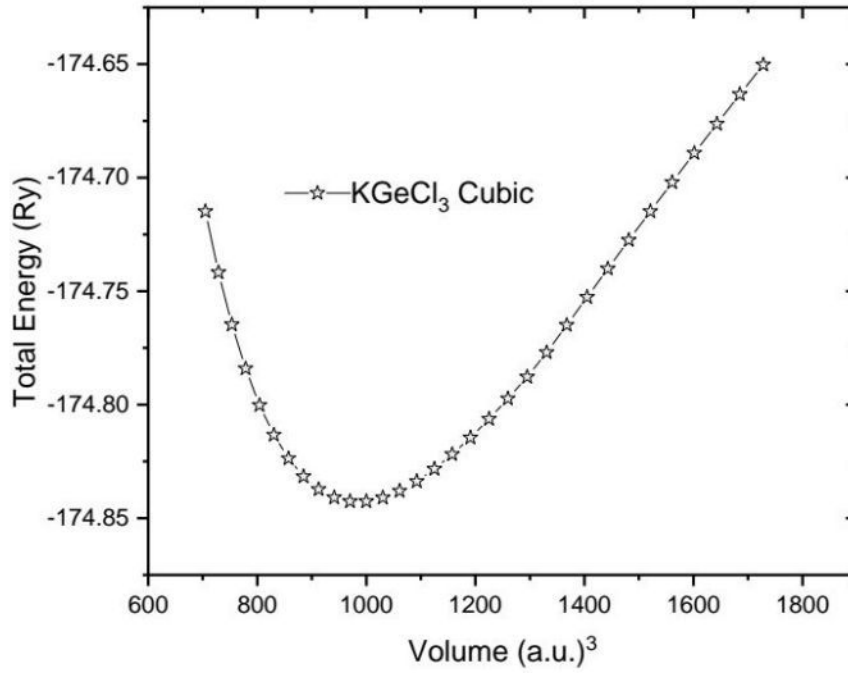


Figure 6.1 a *KGeCl<sub>3</sub> Cubic*

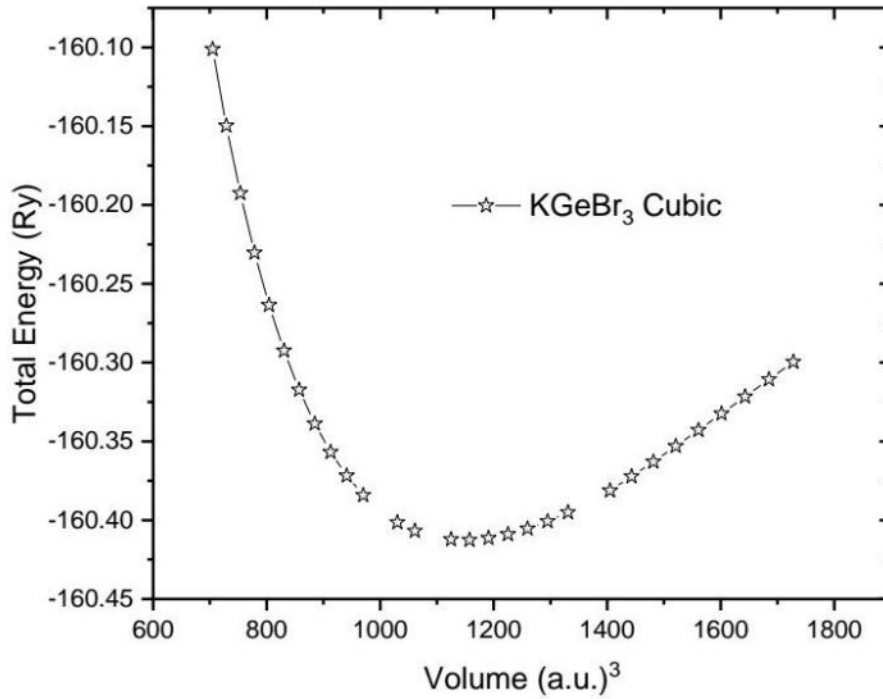


Figure 6.1 b *KGeBr<sub>3</sub> Cubic*

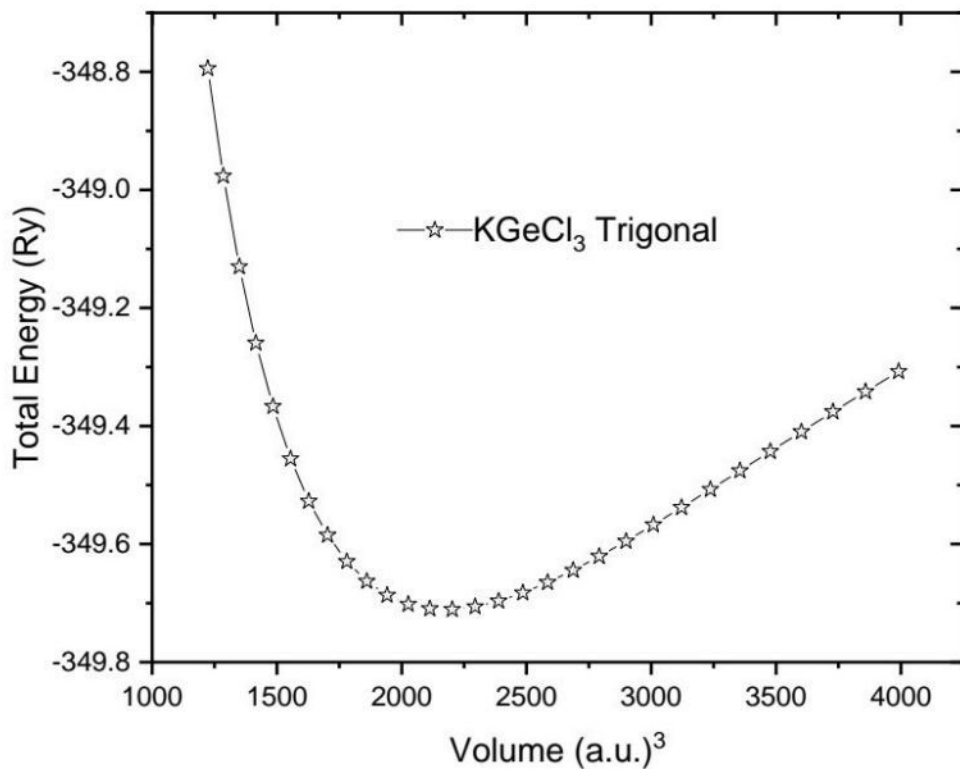


Figure 6.1 c KGeCl<sub>3</sub> Trigonal

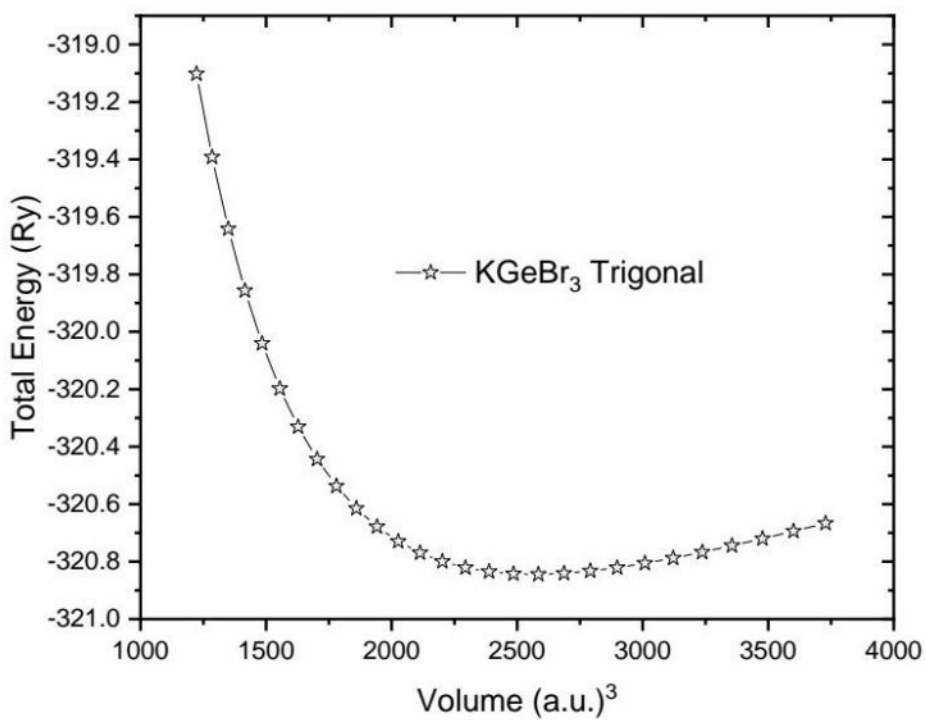


Figure 6.1 d KGeBr<sub>3</sub> Trigonal



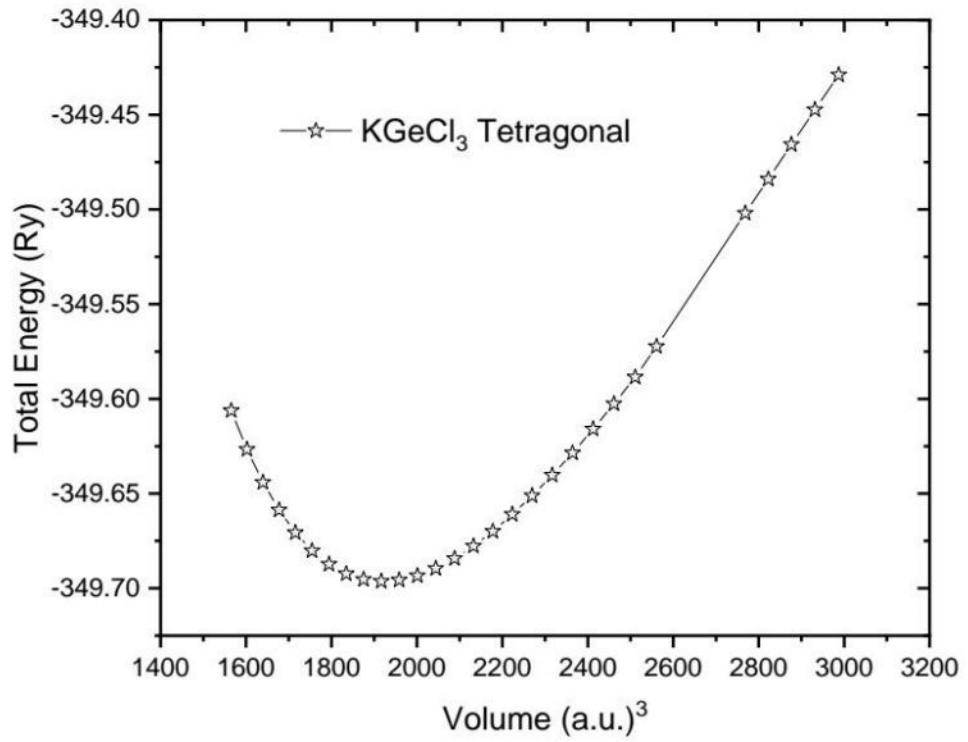


Figure 6.1 e KGeCl<sub>3</sub> Tetragonal

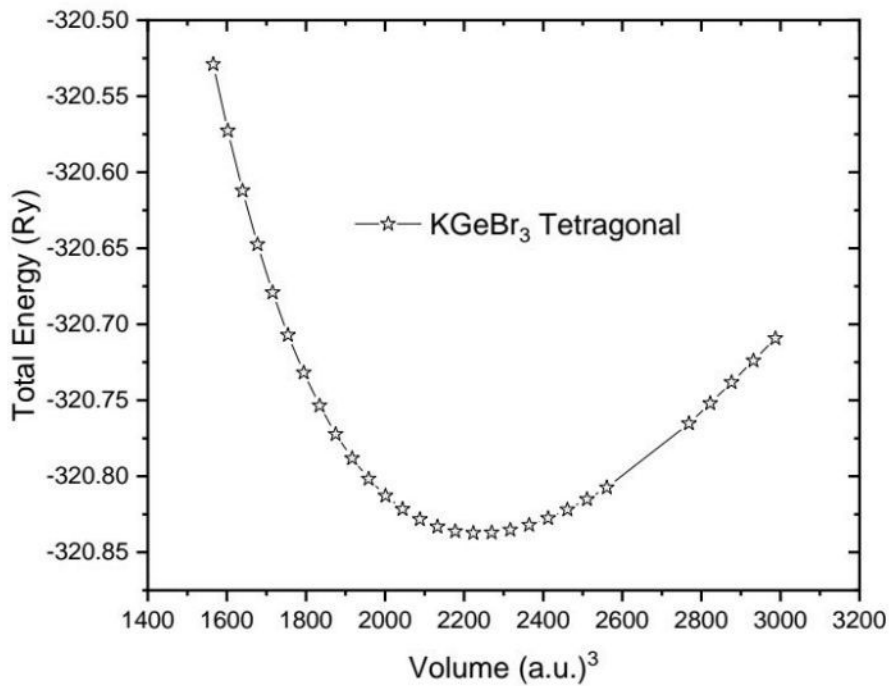


Figure 6.1 f KGeBr<sub>3</sub> Tetragonal

Figure 6.1 The Murnaghan equation of states for the cubic, tetragonal and trigonal KGeX<sub>3</sub> perovskite materials.

## **APPENDIX D: Publications from this Work**

With this work, we managed to write up three research articles which are as follows;

1. DFT study of cubic, tetragonal and trigonal structures of  $\text{KGeCl}_3$  perovskites for photovoltaic applications, *Computational Condensed Matter*, Elsevier.
2. Photovoltaic efficiency of  $\text{Rb}_2\text{InAgCl}_6$  double perovskites: A DFT study, (Under peer review in the *Royal Chemical Society*)
3. DFT study of cubic, tetragonal and trigonal structures of  $\text{KGeCl}_3$  perovskites for photovoltaic applications (Under peer review in *AIP advances*)

## **APPENDIX E: Relevant Conferences and Workshops Attended**

1. Materials Science and Solar Energy Network for Eastern and Southern Africa MSSEESA) Conference (16<sup>th</sup> - 18<sup>th</sup> November 2022)- Eldoret University, Kenya (Hybrid)
2. Science Communication and Data Management Workshop (25<sup>th</sup> - 29<sup>th</sup> April 2022) - University of Nairobi, Kenya
3. DFT & MD Workshop (7<sup>th</sup> - 8<sup>th</sup> April 2022) - Masinde Muliro University of Science and Technology, Kenya
4. Computational Physics Workshop (24<sup>th</sup> - 25<sup>th</sup> February 2022) - Egerton University, Kenya

## **APPENDIX 1**

### **UNIVERSITY OF NAIROBI DIGITAL REPOSITORY DEPOSIT AGREEMENT**

To efficiently administer the University of Nairobi Digital Repository and preserve its contents for long-term use, the University requires certain permissions and warrants from a depositor or copyright owner. By accepting this agreement, a copyright owner still retains copyright to their work and does not give up the right to submit the work to publishers or other repositories. If one is not a copyright owner, they represent that the copyright owner has given them permission to deposit the work.

By accepting this agreement, a depositor/copyright owner grants to the University the non-exclusive right to reproduce, translate and distribute the submission, including the descriptive information (metadata) and abstract, in any format or medium worldwide and royalty free, including, but not limited to, publication over the internet except as provided for by an addendum to this agreement.

**By depositing my/our work in the University of Nairobi Digital Repository, I/we agree to the following:**

- (i) This submission does not, to the best of my/our knowledge, infringe on anyone's copyright or other intellectual property rights.
- (ii) If the submission contains material for which I/we do not hold copyright and that exceeds fair use, I/we have obtained the unrestricted permission of the copyright owner to grant the University the rights required by this agreement and that such third-party owned material is clearly identified and acknowledged within the text or content of the submission
- (iii) The submitted material does not contain any confidential information, proprietary information of others or export controlled information
- (iv) There are no restrictions or required publication delays on the distribution of the submitted material by the University
- (v) Once the submission is deposited in the repository, it remains there in perpetuity
- (vi) The information I/we provide about the submitted material is accurate

- (vii) That if copyright terms for, or ownership of, the submitted material changes, it is my/our responsibility to notify the University of these changes

**I/we understand that the University of Nairobi Digital Repository:**

- (i) May make copies of the submitted work available world-wide, in electronic format via any medium for the lifetime of the repository, or as negotiated with the repository administrator, for the purpose of open access
- (ii) May electronically store, translate, copy or re-arrange the submitted works to ensure its future preservation and accessibility within the lifetime of the repository unless notified by the depositor that specific restrictions apply
- (iii) May incorporate metadata or documentation into public access catalogues for the submitted works. A citation/s to the work will always remain visible in the repository during its lifetime
- (iv) Shall not be under any obligation to take legal action on behalf of the depositor or other rights holders in the event of breach of intellectual property rights or any other right in the material deposited
- (v) Shall not be under any obligation to reproduce, transmit, broadcast, or display the submitted works in the same format or software as that in which it was originally created
- (vi) May share usage statistics giving details of numbers of downloads and other statistics with University of Nairobi staff

While every care will be taken to preserve the submitted work, the University of Nairobi is not liable for loss or damage to the work(s) or associated data while it is stored within the digital repository.

**Work(s) to be deposited:**

AB INITIO STUDY OF THE OPTICAL, STRUCTURAL, ELECTRONIC AND ELASTIC PROPERTIES OF  $KGeX_3$  (X=Br and Cl) INORGANIC  
**Title:** ..PEROVSKITES.FOR.PHOTOVOLTAIC APPLICATIONS .....

MWANAIKI MAUWA NAMISI  
**Author:** .....


**Depositor's Declaration**

I/we ..... MWANAIKI MAUWA NAMISI .....

hereby grant to the University of Nairobi Digital Repository, a non-exclusive license on the terms outlined above.

Name..... MWANAIKI MAUWA NAMISI .....

~~College~~..... Faculty of Science and Technology (FST) .....

Sign.....  .....

Date.. .. 5/12/2022 .....